UNIVERSITÀ
DEGLI STUDI
FIRENZE

PhD in

Atomic and Molecular Photonics

CYCLE XXXVIII

COORDINATOR Prof. Diederik S. Wiersma

Spatiotemporal dynamics of the cortex and their disruption in Shank3b mouse model of autism

Characterization and modulation of large-scale cortical activity using optical techniques

Academic Discipline: FIS/07

Doctoral Candidate

Dr. Ambrosone Manuel

Supervisor

Dr. Anna Letizia Allegra Mascaro

Coordinator

Prof. Diederik S. Wiersma

ABSTRACT

Autism Spectrum Disorders (ASD) comprise a group of neurodevelopmental conditions characterized by behavioral and neuronal abnormalities. Phelan-McDermid Syndrome (PMS) is a specific neurodevelopmental disorder caused by deletions or mutations of the 22q13 region, which often encompass the SHANK3 gene. leading to ASD-like symptoms. Shank3-deficient mice are considered a reliable model for studying PMS, as they display autism-like behaviors and neural impairments. Optical techniques such as widefield fluorescence imaging (WFFI) and optogenetics are increasingly used to characterize and modulate abnormalities in ASD mouse models.

In the first chapter of this thesis, we characterized the calcium indicators GCaMP7f and jRCaMP1b for large-scale monitoring of cortical activity. Using PHP.eB-mediated transfection, we achieved robust and widespread expression across the dorsal cortex, enabling longitudinal imaging. GCaMP7f was employed to study different anesthesia states, while jRCaMP1b was combined with the inhibitory actuator stGtACR2 to develop an all-optical approach for simultaneous inhibition and monitoring of cortical activity. Consistent with previous studies, a single light pulse elicited a rebound of activity, whereas a 1-second illumination at 0.82 mW significantly reduced resting-state activity.

In the second chapter, we first characterized the behavior of Shank3b+/– mice, identifying altered anxiety-like and grooming behaviors. WFFI with GCaMP7f revealed age-dependent cortical hyperconnectivity compared to wild-type littermates, which was reversed under anesthesia. Using convolutional non-negative matrix factorization, we identified distinct spatiotemporal motifs underlying cortical activity. Motor and associative motifs were differently expressed between genotypes and contributed to the observed hyperconnectivity. Movement tracking during imaging further revealed that associative motifs were less correlated 1 second before movement onset in Shank3b+/– mice, suggesting impaired motor-predictive activity.

In the third chapter, we investigated whisker-evoked cortical activity, observing disrupted sensory integration. Specifically, we found a reduced activated area, lower response amplitude in the barrelfield cortex, altered temporal adaptation, and more localized responses in Shank3b+/– mice. Finally, we explored transcranial direct current stimulation (tDCS) as a non-invasive neuromodulation strategy. Anodal tDCS (20 min) modulated cortical excitability, although effects were variable and not consistently genotype-dependent, suggesting further optimization of stimulation parameters.

Overall, this work provides new insights into the developmental trajectory of cortical dysfunction in the Shank3b+/– model of ASD and highlights the relationship between altered network dynamics and behavioral impairments.

Table Of Contents

General Introduction

This doctoral thesis is organized into three main chapters. Each chapter includes an introduction to the state of the art of the topic, a detailed description of the methods, and a section presenting and discussing the results.

The first chapter focuses on the development of optical methods to simultaneously investigate large-scale dynamics of cortical excitatory neurons and to inhibit their activity leveraging a combination of wide-field calcium imaging and optogenetics. To this aim, a retro-orbital injection of a PHP.eB-AAV vector is employed to induce the expression of both the calcium indicator GCaMP7f and of the actuator stGtACR2 across the entire brain. We characterize the effects of stGtACR2-mediated neuronal inhibition across the entire dorsal cortex, monitored through the red-shifted calcium indicator jRCaMP1b.

In the second chapter, we use calcium imaging to study resting-state cortical deficits in the Shank3b+/– mouse model of autism. This powerful technique enables the simultaneous recording of cortical activity and behavior, allowing us to gain deep insight into how cortical activity propagates through the cortex, carrying and transforming information to support behavior.

The third chapter investigates sensory-evoked cortical activation and to characterize differences in the cortical integration of sensory information between Shank3b+/– mice and wild-type controls.

Some sections of this thesis are also included as part of the following research papers:

- Montagni, E., Ambrosone, M., Martello, A. et al. Age-dependent cortical overconnectivity in Shank3 mice is reversed by anesthesia. Transl Psychiatry 15, 154 (2025). https://doi.org/10.1038/s41398-025 03377-5

- Ambrosone, M. et al. All-optical mapping reveals distributed suppression of cortical sensory responses after optogenetic silencing. Brain Stimulation 18, 5 (2025). https://doi.org/10.1016/j.brs.2025.07.003
- Ambrosone, M. et al. Disrupted cortex-wide dynamics impair motor planning in Shank3-mutant mice. *Preprint* (2026). https://doi.org/10.64898/2026.01.14.699439
- Ambrosone, M et al. Altered Spatiotemporal Dynamics of Sensory Processing in Shank3b Mice. *Under preparation*

Technical Development

Introduction

Fluorescence

Fluorescence is a type of radiative emission that occurs following the absorption of energy by a molecule known as a fluorophore (Jameson David M., 2014). A fluorophore is a type of molecule capable of absorbing photons at a specific excitation wavelength and re-emitting them at a longer emission wavelength. Specifically, when a photon of a given wavelength strikes the fluorophore, its electrons are excited from the ground state (S0) to a higher-energy excited state (S1). When the electrons return to the ground state, the fluorophore emits a photon with a longer wavelength. The difference between the absorbed light wavelength and the emitted fluorescence wavelength is called the "Stokes shift," and it is due to a non-radiative energy loss (Jameson David M., 2014; Caminade et al., 2019) (Fig. 1.1A).

Another radiative process, two-photon fluorescence, occurs when the fluorophore is excited by simultaneously absorbing two photons, each having approximately half the energy required for excitation. The two-photon excitation promotes the fluorophore to the same excited state (S1) as one-photon excitation, from which fluorescence emission occurs. The emitted fluorescence photon has a longer wavelength compared to the combined excitation photons (Zipfel et al., 2003; Caminade 2019) (Fig. 1.1B).

This process typically requires a highly focused pulsed laser to achieve the high photon density necessary for the near-simultaneous absorption of the two photons. Due to the quadratic dependence of excitation on photon intensity, two-photon fluorescence is confined to the focal volume, allowing deeper tissue imaging with less excitation and damage outside the focal plane (Helmchen et al., 2005; Luu et al., 2024).

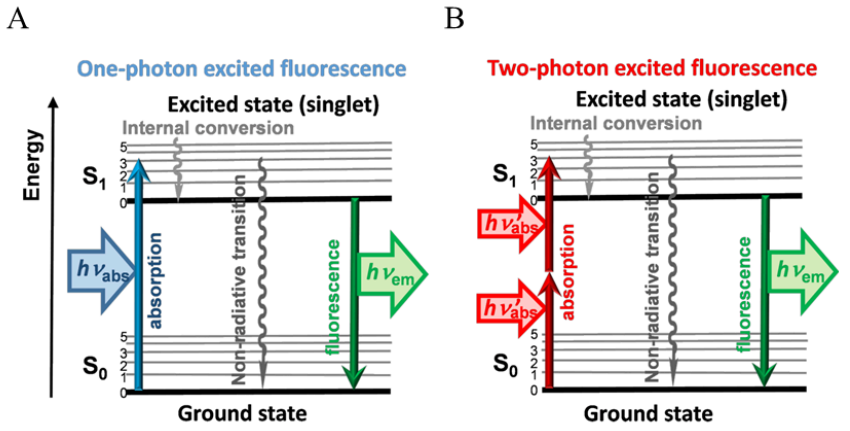

Figure 1.1. Jablonski Diagrams.
Schematic representation of one-photon (A) and two-photon (B) excitation fluorescence in Jablonski diagrams. The ground state is indicated as S_0 and the excited state as S_1. Absorption wavelengths are shown in red for two-photon fluorescence and in blue for one-photon fluorescence, while green indicates the emission wavelength. Modified from Caminade et al., 2019.

Fluorophores can be used in neuroscience to monitor neuronal activity. Specifically, they are coupled to proteins integrated into the neuronal membrane with particular functional groups capable of detecting cell activation (sensors). The protein formed by the coupling between the sensor and the fluorophore is called indicator; it changes conformation when the neuron becomes active and causes the fluorophore to emit fluorescence photons.

Genetically encoded indicators

Genetically encoded indicators have become essential tools for monitoring neuronal activity in vivo. The main types detect direct parameters of neuronal activity, such as changes in membrane potential (GEVIs), neurotransmitter release (GETIs), or calcium concentration (GECIs).

GEVIs enable direct measurement of membrane potential changes with sub-millisecond resolution, capturing both action potentials

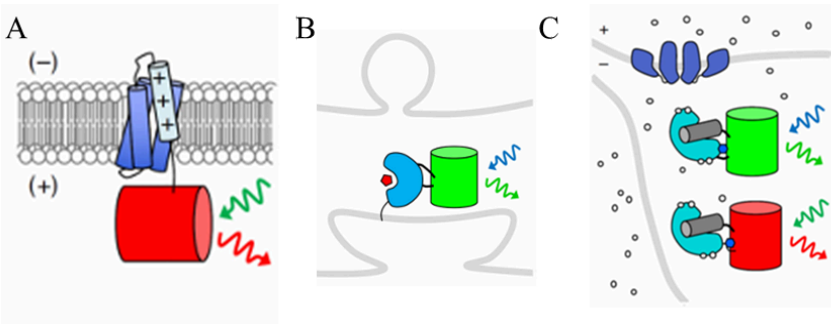

Figure 1.2. Examples of GEVI (A), GETI (B), and GECI (C).
(A) Upon green excitation (leftward green sinusoidal arrow), the GEVI FlicR reports membrane depolarization as an increase in red fluorescence (red sinusoidal arrow) emitted by a circularly permuted red fluorescent protein (cpRFP). (B) The GETI iGluSnFR reports glutamate binding through enhanced fluorescence. When the bacterial glutamate transporter Glt1 undergoes a conformational change in its glutamate-binding domain, the chromophore loses a proton, shifting its absorbance peak to approximately 490 nm. This enables excitation by 488-nm light (blue sinusoidal arrow) and results in green emission (green sinusoidal arrow). (C) In GCaMPs, calcium-induced binding of calmodulin (CaM) to a peptide derived from smooth muscle myosin light-chain kinase (RS20) triggers repositioning of Arg377, leading to an absorbance shift and chromophore deprotonation. Following blue excitation (blue sinusoidal arrow), increased green emission (rightward green sinusoidal arrow) allows detection of calcium transients evoked by synaptic activity (top row) and action potentials (middle row). Modified from Lin & Schnitzer, 2017.

and subthreshold fluctuations. However, GEVIs often have lower brightness and more challenging targeting to the plasma membrane, which can limit their sensitivity and dynamic range (Knopfel, 2012; Platisa & Pieribone, 2018). (Fig. 1.2A)

In contrast, GETIs, such as dLight for dopamine or iGluSnFR for glutamate, provide direct visualization of neurotransmitter release with high spatial and temporal precision, thus complementing the electrical activity measurements provided by GEVIs (Patriarchi et al., 2018; Marvin et al., 2013). While still a rapidly evolving technology, GETIs have weak fluorescence changes upon ligand binding, making detection of subtle neurotransmitter fluctuations

difficult and can perturb the physiology of neurotransmission (Palmer et al., 2011). (Fig. 1.2B)

The most widely used genetically encoded indicators are GECIs, due to their high signal-to-noise ratio and relatively simple expression in neurons. Calcium is a second messenger whose intracellular concentration increases in response to membrane depolarization, mainly through ionotropic receptors (such as NMDA-type glutamate receptors) and voltage-gated calcium channels (Brini et al., 2014). GECIs report neuronal activation indirectly by detecting increases in intracellular calcium concentration that follow action potentials, although they suffer from limited temporal resolution and nonlinear responses (Lin & Schnitzer, 2016; Chen et al., 2013). (Fig. 1.2C)

Overall, each class of indicators presents distinct advantages and limitations, and the choice among them depends on the specific physiological question and spatiotemporal resolution required.

Green GECIs

Among the most widely used and well-characterized GECIs are the GCaMP indicators, which are excited by blue light ($\lambda \approx 470$ nm) and emit fluorescence in the green spectrum ($\lambda \approx 530$ nm).

The mechanism of action of GCaMP indicators involves several key steps: synaptic release of glutamate activates NMDA-type glutamate receptors and voltage-gated Ca^{2+} channels, resulting in calcium influx into the neuron, which is the primary trigger for increases in intracellular Ca^{2+}. Once inside the cell, calcium binds to the calmodulin domain of the GCaMP protein, inducing a conformational change that enables interaction with a circularly permuted green fluorescent protein (GFP). This structural rearrangement enhances fluorescence emission, allowing real-time imaging of calcium dynamics as a proxy for neuronal activation (Lin & Schnitzer, 2016).

One of the most advanced versions, jGCaMP7f, enables precise measurement of neuronal activity with improved kinetics. The letter "f" in its name denotes its fast response, due to a quicker binding and unbinding rate to free cytoplasmic calcium compared to slower variants like jGCaMP7s ("slow"). Despite its speed, jGCaMP7f may be less sensitive in detecting events involving a small number of action potentials and exhibits a nonlinear fluorescence response (Dana et al., 2019).

Red GECIs

Red genetically encoded calcium indicators (RGECIs) consist of a circularly permuted, thermostable red fluorescent protein (RFP), calmodulin (CaM), and M13, a peptide derived from myosin light chain kinase (Suzuki et al., 2016).

Among the most commonly used RGECIs, there are two variants based on different RFPs: mRuby (found in jRCaMP1a and jRCaMP1b) and mApple (present in jRGECO1a and jRGECO1b). These variants have similar spectral properties, with excitation peaks around 558 nm and 568 nm, and emission peaks near 605 nm and 592 nm, respectively (Dana et al., 2016).

Red GECIs offer several advantages for in vivo imaging, including high calcium sensitivity, good photostability, and a relatively linear fluorescence response to changes in intracellular calcium, making it well-suited for long-term recordings and deep-tissue imaging due to reduced scattering of red-shifted light (Emiliani et al., 2015). While red GECIs have historically lagged behind GCaMPs in terms of brightness and kinetics (Chen et al., 2013), recent developments like jRCaMP1b have closed much of this performance gap because of the red fluorescence that is less absorbed by endogenous fluorophores and hemoglobin in mammalian tissue compared to green fluorescence (Montagni et al., 2018).

Expression of GECI's in the brain

A widely adopted approach for expressing GECIs in the mouse brain is the use of transgenic mouse lines, in which the GECI gene is placed under the control of a specific promoter, such as Thy1. The Thy1-GCaMP transgenic lines express improved GCaMP variants in defined neuronal subpopulations, enabling chronic in vivo imaging of calcium transients at the level of individual neurons and synapses in awake, behaving animals. These models provide heritable, robust, and uniform expression across brain regions, making them ideal for longitudinal studies and large-scale neural circuit analysis (Chen et al., 2012).

As a more flexible alternative, recombinant adeno-associated viruses (AAVs) can be used to induce GECI expression in specific brain regions or cell populations. AAV vectors are considered safe and efficient, as they do not integrate into the host genome, elicit minimal immune responses, and support long-term expression (Michelson et al., 2019; Salimzadeh et al., 2013). The use of cell-type-specific promoters, such as CaMKIIα, allows targeting of excitatory neurons (Wang et al., 2013). Similarly, alternative promoters can be used to target other neuronal populations, such as mGAD65 for parvalbuminergic neurons, or GFAP for astrocytes (Deverman et al., 2016; Tasic et al., 2016 Hoshino et al., 2021). Moreover, viral delivery systems enable the rapid expression of multiple gene copies, making them well suited for experiments requiring high fluorescence signals.

AAVs can be administered via intracranial injection, systemic intravenous injection, or retro-orbital injection. Among these, retro-orbital injection has emerged as a preferred method due to its minimally invasive nature, low stress on the animal, and broad transduction efficiency, especially when using engineered AAV capsids such as PHP.eB, which cross the blood–brain barrier in adult subjects with high efficacy (Grødem et al., 2021).

Imaging in neuroscience

In order to monitor neuronal activity in mice, fluorescent microscopy in combination with genetically encoded indicators are widely used.

Two-photon excitation microscopy (2PEF) enables high-resolution imaging of neuronal activity at the cellular and even subcellular level, with excellent optical sectioning and the ability to probe deep cortical layers (Chen et al., 2013). This technique is especially valuable for investigating microcircuit dynamics, but it comes with limitations in terms of field of view and acquisition speed, making it less suitable for capturing large-scale cortical activity.

In recent years, wide-field fluorescence imaging (WFFI) has emerged as a complementary mesoscale approach, providing the capability to monitor cortical activity across multiple areas simultaneously in awake, behaving animals (Cramer et al., 2019; Ren & Komiyama, 2021). Although WFFI lacks the depth resolution of 2PEF and is affected by light scattering and fluorescence originating from multiple cortical layers (Waters, 2020), it offers a better compromise between spatial coverage and temporal resolution.

Importantly, it provides a more direct measure of neuronal activity compared to functional magnetic resonance imaging (fMRI), which relies on indirect signals such as changes in blood oxygenation (the BOLD signal) (Logothetis et al., 2001; Ahmad et al., 2016). In this sense, WFFI bridges the gap between the fine spatial detail of 2PEF and the large-scale, non-invasive perspective offered by fMRI, making it a powerful tool for studying distributed neuronal processes with cellular resolution and whole-cortex coverage.

Optogenetics as a modulation tool

Monitoring cortical activity with WFFI can be combined with optical modulation of the cortex. Optogenetics enables precise and reversible manipulation of neuronal activity by using light to activate or inhibit genetically encoded light-sensitive ion channels (Acharya et al., 2021).

This approach provides a powerful way for modulating neural circuits, allowing either excitation or suppression of targeted populations with high temporal precision (Deisseroth, 2011, Khalanithi et al., 2012). Among the most widely used genetically encoded actuators for neuronal excitation are Channelrhodopsins (ChRs), light-gated cation channels that depolarize neurons in response to light, leading to action potential firing (Boyden et al., 2005). Variants such as ChR2(H134R) and Chronos offer improved photocurrents and kinetics, enabling precise temporal control of neuronal activation (Jun & Cardin, 2019). On the inhibitory side, tools like halorhodopsins (e.g., eNpHR3.0), which pump chloride ions into the cell upon light irradiation, and archaerhodopsins (e.g., ArchT), which hyperpolarize neurons through proton extrusion, have been extensively employed to silence activity (Zhang et al., 2006). Among these, blue-light actuators are now highly used in combination with red-shifted indicators to modulate and visualize neuronal activity with reduced cross-talk (Forli et al., 2018; Resta et al., 2022; Fan et al., 2020). Exploiting the WFFI is now possible to perturb neuronal activity at arbitrary point and simultaneously measure its effect (Esmaeili et al., 2021; Resta et al., 2022). More recently, anion-conducting channelrhodopsins such as GtACR2 have emerged as highly effective inhibitory actuators, providing rapid and reversible neuronal silencing with minimal phototoxicity and high light sensitivity (Park et al., 2022; Mahn et al., 2016). Compared to other inhibitory optogenetic tools, GtACR2 exhibits a favorable photon-to-ion transport ratio and high single-channel conductance. Its soma-targeted version, stGtACR2, offers

enhanced light sensitivity, minimizes unwanted axonal activation, and generates strong photocurrents, making it particularly efficient for precise neuronal silencing (Mahn et al., 2018).

In this first chapter, we characterize the expression of the calcium indicators GCaMP7f and jRCaMP1b following retro-orbital injection to evaluate their feasibility for large-scale cortical activity monitoring in different brain states. Given its spectral compatibility with blue-light actuators, we selected jRCaMP1b to develop a novel all-optical approach that combines targeted cortical inhibition using stGtACR2 with simultaneous activity readout.

Gcamp7f and WFFI as a tool for monitoring large scale cortical activity

Materials and Methods

Virus injection for the expression of GCaMP7f

To selectively express the genetically encoded calcium indicator GCaMP7f in excitatory neurons, a viral vector (ssAAV-PHP.eB/2-mCaMKIIα-jGCaMP7f-WPRE-bGHp(A); titer: 1.3×10^{13} vg/mL; Viral Vector Facility, CH) was systemically delivered via the retro-orbital sinus. Injections were performed on postnatal day 30 (P30) under isoflurane anesthesia. The viral stock was diluted in sterile saline to a final volume of 150 µL. Following the injection, mice were returned to their home cages and monitored during recovery.

Intact skull window surgery

One week after viral delivery, animals underwent preparatory surgery to enable chronic imaging under head fixation. Mice were anesthetized with isoflurane (3% for induction, 1–2% for maintenance) and positioned in a stereotaxic frame (KOPF model 1900). To prevent corneal desiccation during surgery, ophthalmic

gel (Lacrilube) was applied to the eyes, and body temperature was maintained at 37 °C using a feedback-controlled heating pad.

A local anesthetic (2% lidocaine) was applied to the scalp before making the incision. The skin and periosteum covering the skull were carefully removed, and the cranial landmarks bregma and lambda were identified and marked. A custom-made aluminum head bar was secured posterior to lambda using dental cement (Super Bond C&B, Sun Medical). The remaining exposed skull surface was sealed with the same transparent cement to create a stable and durable preparation suitable for longitudinal imaging through the intact skull.

Postoperative care was provided in a controlled environment, ensuring optimal temperature and humidity. Mice were monitored until fully awake and were given unrestricted access to food and water.

Wide-field microscope

Wide-field calcium imaging was performed using a custom-built epifluorescence microscope. Excitation of the GCaMP7f calcium indicator was achieved using a 470 nm LED light source (M470L3, Thorlabs, NJ, USA) filtered through a 482/18 nm bandpass filter (Semrock, Rochester, NY, USA). The excitation light was reflected onto the brain surface by a dichroic mirror (DC FF 495-DI02, Semrock) and directed through a 2X Super Apochromatic objective (TL2X-SAP, 0.1 NA, 56.3 mm working distance; Thorlabs).

To acquire reflectance signals, a 530 nm LED light source (M530L4, Thorlabs) was positioned at a 45° angle relative to the cortical surface. Both excitation and reflectance channels were alternated using a stroboscopic illumination protocol (20 Hz per LED). Emitted fluorescence and reflectance signals were filtered

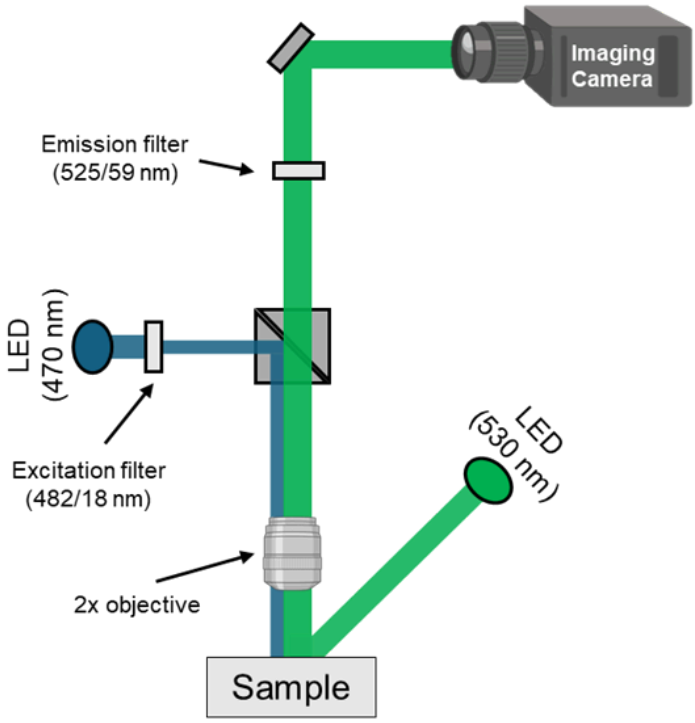

Figure 1.3. Widefield fluorescence microscope.
Optical path for the widefield fluorescence microscope including GCaMP7f and reflectance imaging. See materials and methods for details.

through a 525/50 nm bandpass filter (Semrock) and recorded using a CMOS camera (ORCA-Flash4.0 V3, C13440-20CU; Hamamatsu). Imaging was conducted at a frame rate of 40 Hz, with a spatial resolution of 512 × 512 pixels, corresponding to a field of view of approximately 11.5 × 11.5 mm. (Fig. 1.3)

Habituation and awake imaging

Mice were gradually habituated to head-fixation over two consecutive days (15 minutes per day per mouse) to minimize anxiety and sudden movements during data acquisition. Imaging sessions were conducted 14 days after the viral injection, at multiple time points (P45, P60, and P90).

Image stacks were registered using custom-developed software. This program centers the field of view (FOV) by overlaying a cross aligned with the bregma landmark, which was previously marked on the skull with a black dot. This allowed precise alignment of each imaging session across animals and timepoints based on the anatomical reference of bregma.

Each session consisted of four recordings, each lasting 180 seconds, capturing spontaneous cortical activity in awake, resting mice. The animals were head-fixed but allowed to freely move their limbs and were not engaged in any specific tasks.

Imaging under anesthesia

The day after the awake imaging sessions, the same mice were anesthetized with isoflurane to investigate spontaneous cortical activity across different brain states. Anesthesia depth was modulated by adjusting isoflurane concentration to achieve stable global rhythmic activity patterns, measured as slow oscillations averaged over the entire field of view.

Deep anesthesia was characterized by slow oscillations at approximately 0.1–0.2 Hz and was maintained at an average isoflurane concentration of $1.7 \pm 0.1\%$. Slightly higher isoflurane levels produced medium anesthesia, where oscillatory activity increased in frequency to 0.2–0.4 Hz (average concentration $1.5 \pm 0.1\%$). Light anesthesia, achieved at lower isoflurane levels ($1.3 \pm 0.1\%$), exhibited longer up-states interspersed with brief down-states. Due to anesthesia stability constraints, anesthesia recordings were performed starting from the highest to the lower isoflurane concentration.

Each anesthesia level was maintained for 60 minutes, with ongoing monitoring to ensure a consistent slow-oscillatory regime. Imaging sessions consisted of repeated recordings of spontaneous activity (180 s-long). Throughout anesthesia, body

temperature was regulated at 37 °C using a feedback-controlled heating pad.

Ex-vivo immunohistochemistry protocol

To validate the expression of GCaMP7f in the excitatory neurons, histological analysis was performed ex vivo at postnatal day 90 (P90). Mice were deeply anesthetized and transcardially perfused with 20 mL of phosphate-buffered saline (PBS, 0.1 M, pH 7.6), followed by 100 mL of 4% paraformaldehyde (PFA). Brains were extracted and sectioned coronally at 100 µm thickness using a vibratome (Vibratome Series 1500 Tissue Sectioning System).

For immunofluorescence staining, free-floating brain slices were incubated in a blocking solution containing 1% bovine serum albumin (BSA) and 0.1% Triton X-100 in PBS for 1 hour at room temperature. After three washes in PBS with 0.1% Triton X-100, the sections were incubated overnight at 4 °C with a primary antibody against PV (rabbit anti-PV, 1:500, Abcam, ab11427). The following day, sections were rinsed and incubated for 2 hours at room temperature with a secondary antibody conjugated to Alexa Fluor 594 (anti-rabbit, 1:200, Abcam, ab150080). Finally, slices were mounted for imaging.

Confocal microscopy Imaging

Immunostained slices were imaged using a confocal laser scanning microscope (Nikon Eclipse TE300 with C2 scanning head). The system was equipped with a 20× Plan Apo air objective. Two lasers were used for fluorescence excitation: a 488 nm laser for GCaMP7f and a 561 nm laser for Alexa Fluor 594. The emitted signals were collected through bandpass filters (520/35 nm for GCaMP7f and 630/69 nm for Alexa 594). Colocalization of PV+ cells with GCaMP7f signal was assessed in three coronal sections per animal.

To further evaluate the cortical distribution of GCaMP7f expression across layers, additional high-resolution imaging was performed on three coronal slices per animal at defined distances from bregma. These images were acquired using a Nikon Ti2-E Spinning Disk confocal microscope, equipped with a CFI Plan Apo 10× Glyc water-immersion objective (NA 0.5). This setup enables rapid and sensitive volumetric imaging with improved axial resolution, particularly suitable for imaging large areas of cortex with high fidelity.

Data analysis

All data analyses were performed in MATLAB (MathWorks), ImageJ, and Origin.

In-vivo quantification of raw fluorescence

To evaluate in vivo GCaMP7f expression, a region of interest (ROI) was manually defined based on the mean fluorescence of the entire FOV, carefully excluding the outer edges of the skull preparation to minimize signal variability. Within this ROI, the average fluorescence intensity was measured at three developmental stages (P45, P60, and P90), allowing for a temporal assessment of expression stability and distribution across the dorsal cortical surface.

Image preprocessing

Image stacks collected across sessions for each mouse were aligned using custom-made software that relied on the anatomical landmarks bregma and lambda. A subject-specific field of view (FOV) template was used to manually fine-tune the imaging area on each recording day. To assign functional signals to distinct cortical regions, the imaged cortex was registered to a two-dimensional projection of the Allen Mouse Brain Atlas (www.brain-map.org), aligned to match our imaging plane. For each recording block, $\Delta F/F_0$ was calculated at the pixel level,

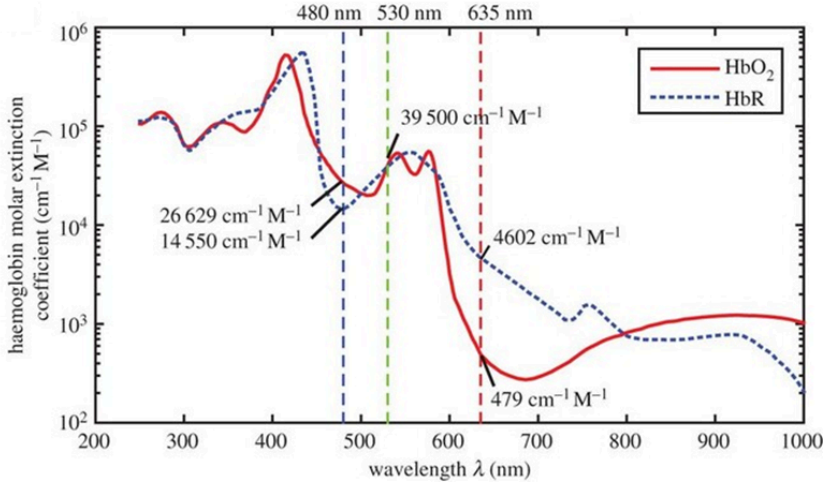

Figure 1.4. Measurement of hemodynamics.
Oxy- and deoxyhemoglobin (HbO2 and HbR) absorption spectra in the visible spectrum. Vertical lines show common wavelengths for reflectance measurement. Modified from Ma et al., 2016.

where ΔF represents the change in fluorescence intensity at a given time point relative to the mean fluorescence (F_0) across the session. Hemodynamic correction was then applied following the ratiometric method described by Scott et al., and reported in the following formula:

$$\frac{F}{F_0} = \frac{\frac{I^{482}}{I_0^{482}}}{\frac{I^{525}}{I_0^{525}}} \quad \text{(Equation 1)}$$

The corrected GCaMP signal (F/F_0) was derived using the ratio between the fluorescence signal at 482 nm (I_{482}) and the reflectance signal at 525 nm (I_{525}) (Ma et al., 2016; Valley et al., 2020; Scott et al., 2018). (Fig. 1.4)

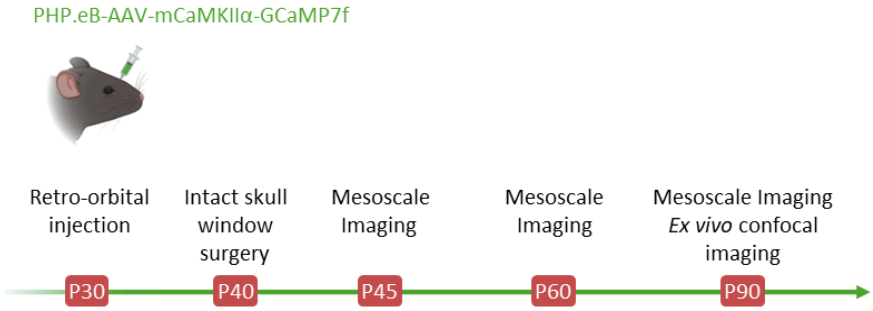

Figure 1.5 Experimental timeline for GCaMP7f.
Experimental timeline with retro-orbital injection of GCaMP7f, optical window surgery and in vivo imaging at P45, P60 and P90. After in vivo experiments, confocal imaging analysis was performed.

Finally, each image was then resized to 128x128 pixels.

Ex-vivo quantification and PV colocalization

In order to evaluate the efficacy of virus transfection in the excitatory neurons, the fluorescent neurons in the cortex from 3 mice were analyzed by an experienced observer quantifying the percentage of cells showing co-expression of both the indicator and the PV neurons.

Results

In this section, a total of 27 mice were used to characterize the feasibility of the GCaMP7f indicator for large scale longitudinal study of cortical activity in different brain states. Mice were retroorbitally injected with the AAV-PHP.eB carrying the CaMKIIα-GCaMP7f construct at P30. After 10 days an intact skull window surgery was performed in order to have free access to the cortical activity. In vivo mesoscale imaging was performed

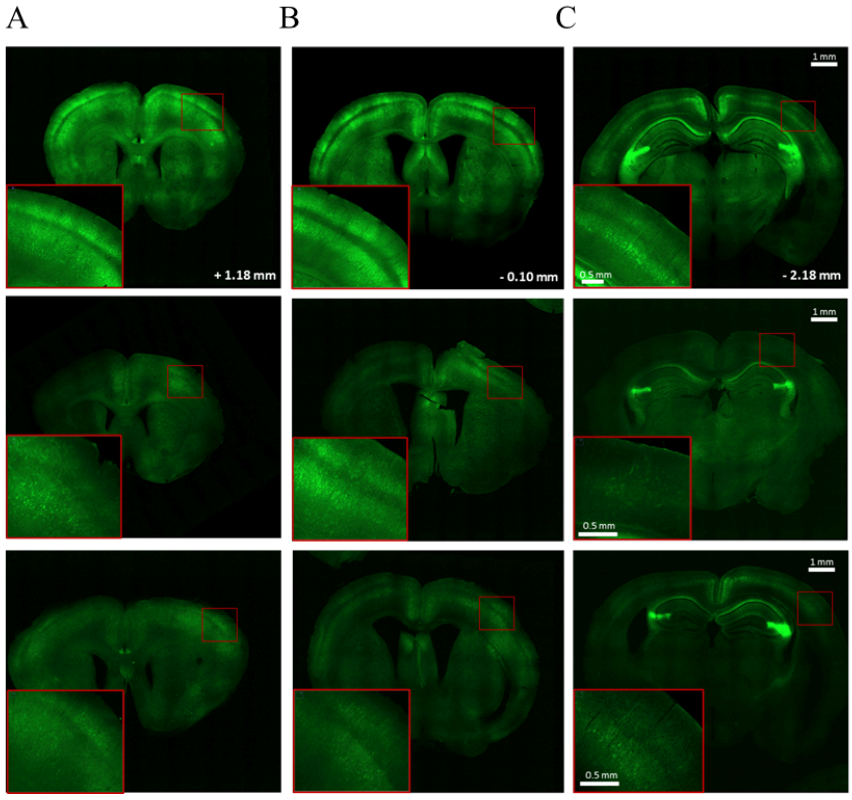

Figure 1.6. Cortical AAV-PHP.eB GCaMP expression.
Low magnification pictures of three distinct mice at P90 demonstrating GCaMP expression in coronal histological slices at various separations from the bregma (shown on the lower right for the first line of figures). A chosen field of view (FOV) displayed at increased magnification in the motor cortex (A), barrel field cortex (B), and visual cortex (C) is represented by red boxes.

at P45, P60 and P90 and eventually the expression was evaluated through ex vivo confocal imaging (Fig. 1.5).

Ex vivo expression of the GCaMP7f indicator in the cortex excitatory neurons

Exploiting ex vivo confocal imaging, we demonstrated that PHP.eB-AAV injection allows for widespread expression of the

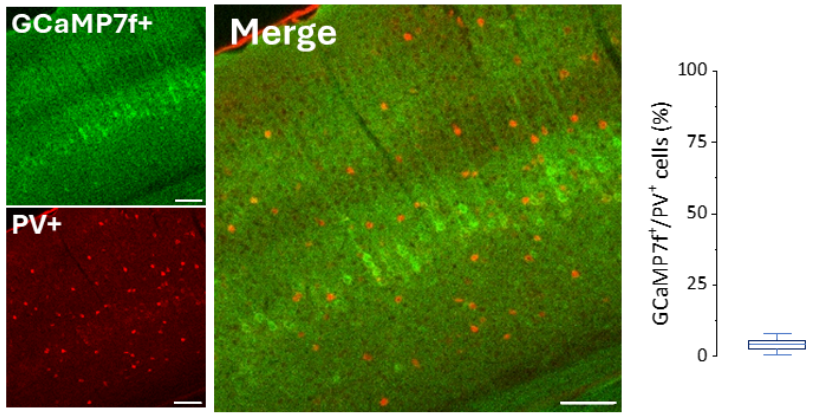

Figure 1.7. GCaMP7f expression in excitatory and parvalbuminergic neurons.
Left, representative immunohistochemistry images showing the neuronal expression of GCaMP7f (green) and PV (red) in the whole cortical layers, scalebar: 100µm. Right, Quantification of the colocalization ratio GCaMP7f+/PV+.

calcium indicator GCaMP7f throughout the cortex (Fig. 1.6), with a strong tropism for layer V pyramidal neurons.

To confirm the selectivity of the CaMKIIα promoter for excitatory neurons, we performed immunohistochemistry on brain slices. Sections were stained for parvalbumin (PV), a marker of inhibitory interneurons. The vast majority of PV-positive cells did not express GCaMP7f, confirming that expression was largely restricted to excitatory neurons (7.4±1.0%, n=3 mice) (Fig. 1.7).

In vivo mesoscale Ca^{2+} imaging across cortical regions

In vivo imaging was conducted at multiple time points following injection and the dorsal cortical surface was monitored using wide-field fluorescence imaging, which allowed simultaneous recording from distinct cortical areas (Fig. 1.8 A).

To assess the stability of expression of GCaMP7f over time, we monitored fluorescence intensity at P45, P60, and P90 finding that the expression levels remained consistent across time points

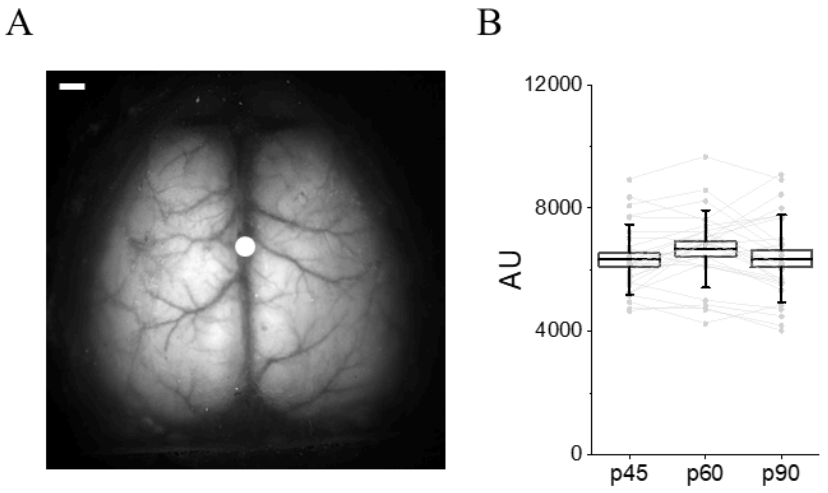

Figure 1.8. In vivo measurement of GCaMP7f expression across timepoints.
(A) Representative image of the field of view. White dots represent bregma, scalebar: 1mm.
(B) In vivo quantification of GCaMP7f expression at P45, P60 and P90.

(6326 ±223AU- P45, 6679±245AU- P60, 6354±277AU- P90, n=27, one-way repeated measure ANOVA). (Fig. 1.8 B).

Brain state modulation through anesthesia levels

To investigate cortical dynamics under different brain states, we modulated the level of anesthesia by adjusting isoflurane concentrations between 1.3% and 1.7% (Fig. 1.9 A).

This protocol allowed us to distinguish between light and deep anesthesia states. Light anesthesia was characterized by prolonged Up-states and shortened Down-states, whereas deep anesthesia exhibited the opposite pattern. These differences were consistent across recording time points (Fig. 1.9 B-E).

Finally we demonstrated that this systemic expression strategy enabled large-scale imaging of excitatory neurons under

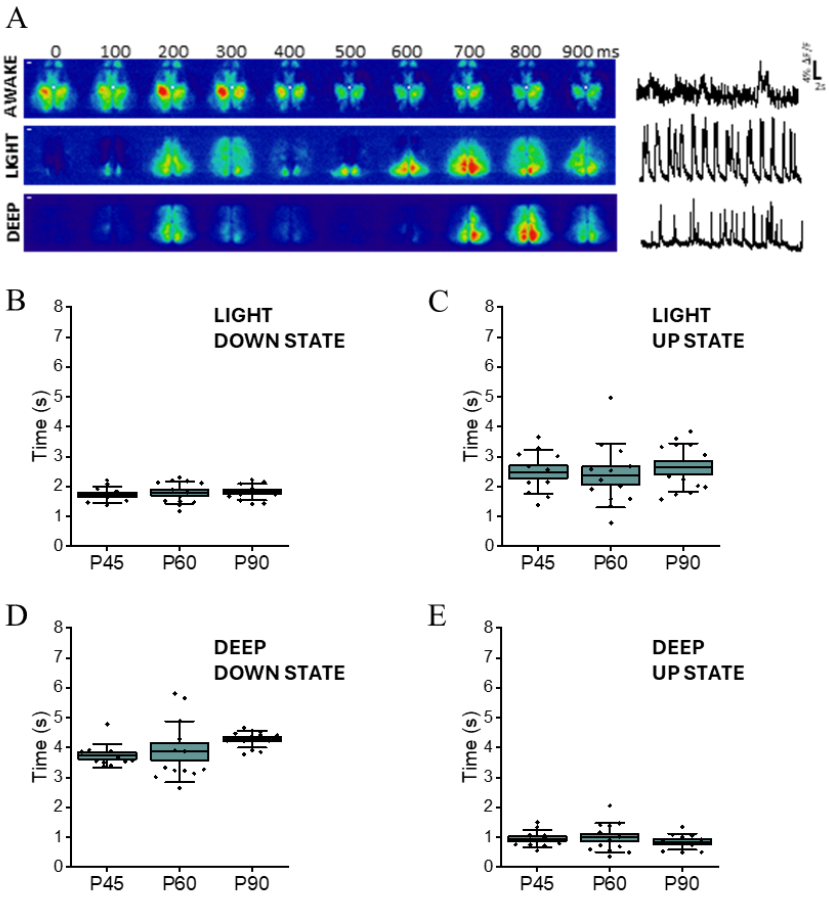

Figure 1.9. In vivo large scale calcium imaging in awake and anesthesia states.
(A) Left, representative image sequences showing cortical activity in three different brain states (awake, light anesthesia and deep anesthesia). White dots represent bregma, scale bar: 1mm. Right, representative single-trail time series showing averaged cortical activity in the same brain states.
(B-E) Average down state duration (B,D) and up state duration (C,E) under light and deep anesthesia.

various brain states: wakefulness, light anesthesia, and deep anesthesia.

Large scale all-optical imaging and inhibition of the cortex through jRCaMP1b + stGtACR2

Materials and Methods

Virus injection for the expression of jRCaMP1b and stGtACR2

To achieve transfection of excitatory neurons with the jRCaMP1b indicator and the optogenetic actuator stGtACR2, mice were injected with a single retro-orbital injection of a mixture containing two AAV-PHP.eB viruses. The final solution was prepared by diluting 25 µL of the indicator vector (ssAAV-PHP.eB/2-mCaMKIIα-NES_jRCaMP1b-WPRE-hGHp(A), 1.2×10^{13} vg/ml) and 12.5 µL of the actuator vector (ssAAV-PHP.eB/2-mCaMKIIα-stGtACR2_mCerulean-WPRE-bGHp(A), 1.7×10^{13} vg/ml) in 112.5 µL of saline. Each mouse thus received 3.0×10^{11} vg of the indicator and 2.1×10^{11} vg of the actuator. A sham group was injected with 25 µL of the indicator diluted in 112.5 µL of saline, without the actuator.

As in the GCaMP7f protocol, intact skull window surgery was performed in order to have free access to fluorescence from cortical neurons and, here, to illuminate with the optogenetic path.

Widefield microscope and optogenetic

A red LED light source (595 nm, M595L3, Thorlabs, New Jersey, USA) combined with a bandpass filter (578/21 nm, Semrock, Rochester, NY, USA) and a dichroic mirror (606 nm, Semrock) was used to excite jRCaMP1b. Excitation light was directed through a 2X objective (TL2X-SAP 2X Super Apochromatic, 0.1 NA, 56.3 mm working distance, Thorlabs) onto the skull. Activation of the stGtACR2 actuator was achieved using a continuous-wave laser (473 nm, OBIS LX 75 mW, Coherent, Santa Clara, CA, USA), focused into the imaging path via a dichroic beam splitter (FF484-Fdi01-25 336, Semrock). The

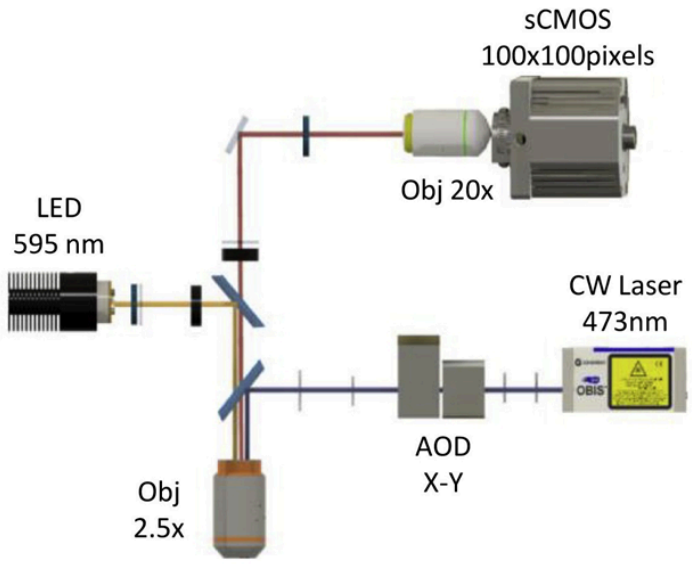

Figure 1.10. Widefield microscope and optogenetics.
Schematic representation of the double-path wide-field fluorescence microscope. See methods for details. Modified from Resta et al., 2022.

imaging system included a random-access scanning head equipped with two acousto-optic deflectors (DTSXY400, AA Opto-Electronic, Orsay, France) and used a laser beam with an approximate diameter of 200 μm. Fluorescence emitted by jRCaMP1b was filtered (630/69 nm, Semrock) and captured by a high-speed CMOS camera (Orca Flash 4.0, Hamamatsu Photonics, NJ, USA) at 40 Hz with a resolution of 512×512 pixels, covering a 11.6×11.6 mm² field of view of the mouse cortex. To quantify stGtACR2 fluorescence across the dorsal cortex, a blue LED (415 nm, M415L4, Thorlabs) was used along with a bandpass excitation filter (432/36 nm, Semrock) and a dichroic mirror (425 nm, Semrock). The emitted signal was then filtered (480/15 nm, Semrock) and recorded using a CMOS camera (ORCA-Flash4.0 V3, C13440-20CU; Hamamatsu) (Fig. 1.10).

Calibration of optogenetic irradiation

Laser stimulation patterns were generated using two orthogonally mounted acousto-optic deflectors (AA Opto-electronic). A reference image of the field of view (FOV) was used to guide the laser beam toward a specific cortical region corresponding to the barrel field cortex (BFD), located at x = 3.2 mm right and y = 1.3 mm posterior to bregma.

Single-pulse stimulation consisted of a 10 ms laser pulse, repeated 10 times per session, with each session including 15 seconds of baseline (PRE-stim) and 11 seconds after stimulation (POST-stim), across increasing laser power levels (0.15 – 0.32 – 0.82 – 1.66 – 3.34 – 6.85 – 10.4 mW). For 5-second stimulation, the laser was applied for 5 seconds, repeated 10 times per session (15 s PRE-stim, 6 s POST-stim), using three power levels (0.15 – 0.32 – 0.82 mW). To test optogenetic inhibition at different durations, laser pulses of 1, 2, 3, 4, or 5 seconds were delivered at a constant power of 0.82 mW, each repeated 10 times with 15 seconds of baseline and 6 seconds after stimulation in each session.

Confocal microscopy imaging

As in the GCaMP7f protocol, mice were perfused and brain coronal slices were obtained. Imaging was carried out using a Nikon Eclipse TE300C2 laser confocal scanning microscope (Nikon), aligned with the BFD position, and equipped with a Nikon Plan Apo 20x air objective. The system utilized two lasers (408 nm and 561 nm) to simultaneously excite stGtACR2 and jRCaMP1b, respectively. Emitted fluorescence was detected using bandpass emission filters set at 472/10 nm for the actuator and 630/69 nm for the indicator.

Data analysis

All data analyses were performed in MATLAB (MathWorks), ImageJ, and Origin.

In vivo quantification of raw fluorescence

To assess in vivo expression, a region of interest (ROI) was selected on the jRCaMP1b image, encompassing the entire dorsal cortex while excluding the borders of the skull window. For both the calcium indicator and the optogenetic actuator, expression levels were quantified by calculating the mean fluorescence within the ROI at two time points: 20 and 30 days post-injection (dpi).

Optogenetic calibration

For each imaging session, ΔF/F was computed using the baseline fluorescence (F), defined as the mean signal recorded prior to optogenetic stimulation. Frames contaminated by skull autofluorescence caused by laser exposure were excluded from analysis. Images were resized to 256×256 pixels, and a 10×10 pixel region of interest (ROI) was selected based on the laser stimulation site. For single-pulse stimulation, both the peak amplitude and the full width at half maximum (FWHM) of the response were calculated. In the case of multiple durations irradiation, the mean ΔF/F was measured before and after the laser stimulation period.

Ex vivo confocal imaging

An experienced observer analyzed fluorescent neurons in the cortex of 3 mice to determine the percentage of cells co-expressing both the calcium indicator and the optogenetic actuator.

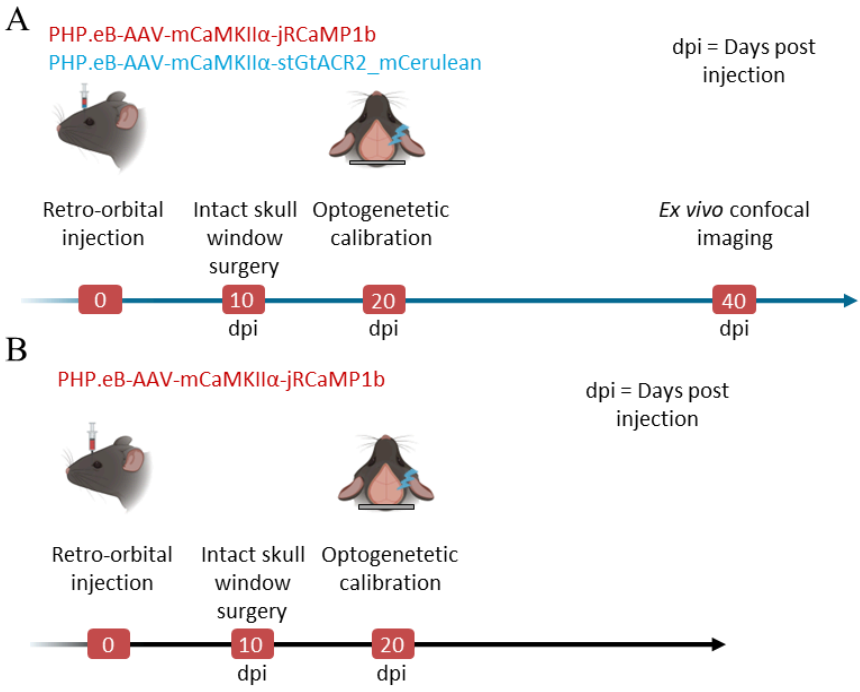

Figure 1.11 Experimental timeline for experimental group and sham control.
(A) Experimental timeline with retro-orbital injection of both jRCaMP1b and stGtACR2, optical window surgery 10 days post injection (dpi) and in vivo imaging calibration at 20dpi. After in vivo experiments, confocal imaging analysis was performed.
(B) Experimental timeline with retro-orbital injection of jRCaMP1b, optical window surgery 10 days after injection (dpi) and in vivo imaging session 20 dpi.

Statistical analysis

Paired sample t test was used for the comparison of in vivo expression between time points. Two way RM ANOVA followed by Bonferroni correction was used for the comparison between pre and post irradiation ΔF/F. Differences were considered significant when $p<0.05$. Errors are reported as Standard Error of Means, *p <0.05, **p<0.01, ***p<0.001.

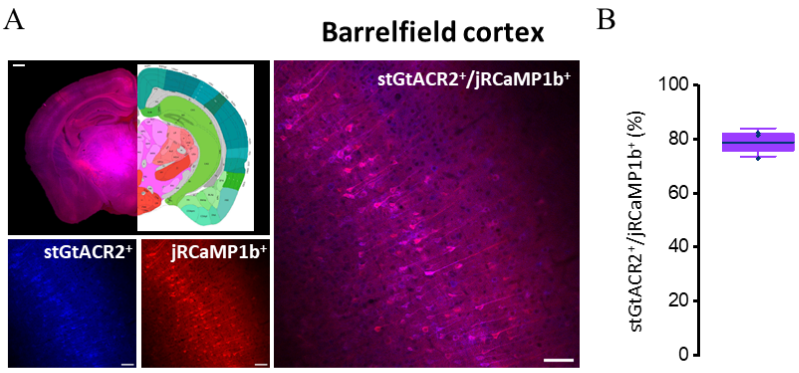

Figure 1.12. Co-expression of jRCaMP1b and stGtACR2 in the barrelfield cortex.
(A) Upper left: Representative wide-field image of a single slice with related Allen Brain Atlas reference, scale bar: 1mm. Bottom left: Representative confocal images showing the neuronal expression of jRCaMP1b (red) and stGtACR2 (blue) in the barrel field cortex, scale bar: 100 µm. Right: Merge of the representative images, scale bar: 100 µm.
(B) Quantification of the absolute (dots) and average (line) colocalization ratio stGtACR2^{+}/ jRCaMP1b^{+}.

Results

In this section, a total of 13 mice were used to characterize the all optical system for simultaneous monitoring and inhibition of cortical activity. 8 mice were injected with both jRCaMp1b and stGtACR2 (Fig. 1.11A) while 5 mice were used as sham (jRCaMP1b only) (Fig. 1.11B).

Ex vivo validation of co-expression and specificity

To confirm the selectivity and spatial distribution of expression, we performed histological analysis on brain sections collected at 30 days post-injection (dpi). Fluorescence imaging revealed widespread cortical expression of both jRCaMP1b and stGtACR2. Notably, the two constructs were co-expressed in a large proportion of neurons in the BFD (Fig. 1.12) (78.9 ± 3.03%; n = 3 mice). Similar co-expression levels were also observed in the motor and visual cortices (Fig. 1.13) (Motor cortex:

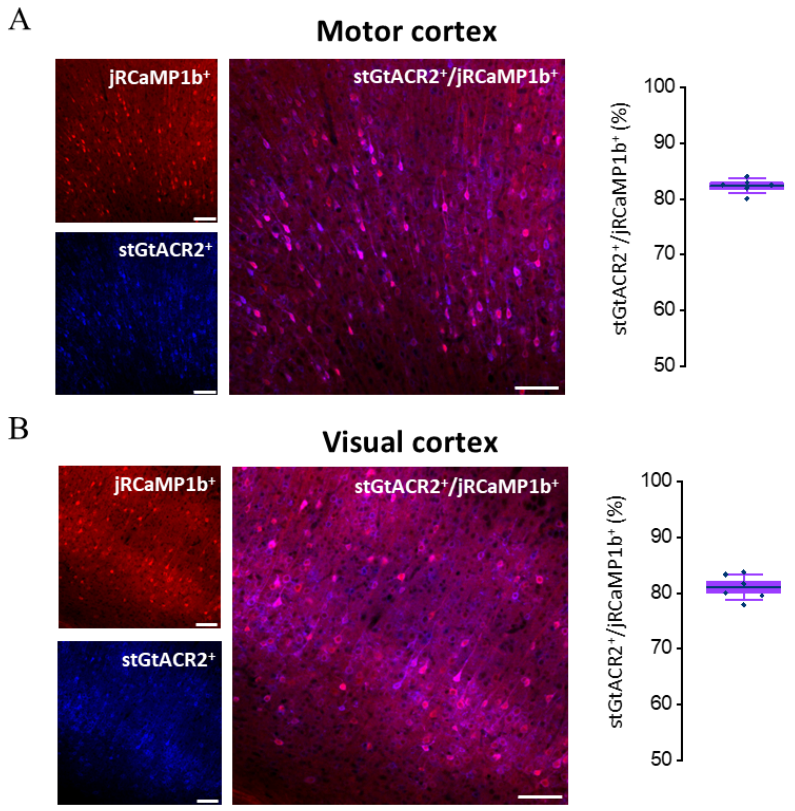

Figure 1.13. Co-expression of jRCaMP1b and stGtACR2 in the motor and visual cortices.
(A) Left: Representative confocal images showing the neuronal expression of jRCaMP1b (red) and stGtACR2 (blue) in the motor cortex with merge (purple), scale bar: 100 µm. Right: Quantification of the absolute (dots) and average (line) colocalization ratio stGtACR2^{+}/ jRCaMP1b^{+}.
(B) Left: Representative confocal images showing the neuronal expression of jRCaMP1b (red) and stGtACR2 (blue) in the visual cortex with merge (purple), scale bar: 100 µm. Right: Quantification of the absolute (dots) and average (line) colocalization ratio stGtACR2^{+}/ jRCaMP1b^{+}.

82.3 ± 0.54%; Visual cortex: 81.0 ± 0.94%; n = 2 mice, N = 6 slices). These findings confirm efficient and consistent dual expression of the calcium indicator and optogenetic actuator following a single retro-orbital injection.

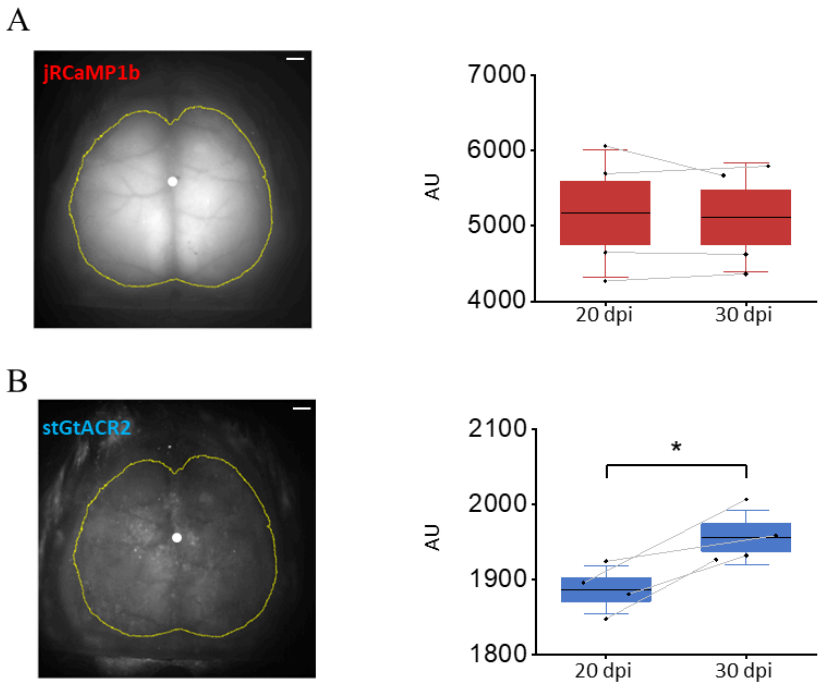

Figure 1.14. In vivo expression of jRCaMP1b and stGtACR2 across time.
Representative images of the field of view of jRCaMP1b (A) and stGtACR2 (B) with relative in vivo quantification of absolute (dots) and average (line) jRCaMP1b (red) and stGtACR2 (blue) expression. Yellow lines represent the selected ROI for analysis. Scalebar: 1mm

In vivo assessment of expression stability

To evaluate the in vivo expression, we measured fluorescence signals from both indicator and actuator at two imaging time points (20 and 30 dpi). High and stable expression levels were detected for both indicator and actuator in the two time points. (Fig. 1.14) (jRCaMP1b: 5168 ± 423 AU at 20 dpi, 5111 ± 362 AU at 30 dpi; stGtACR2: 1886 ± 16 AU at 20 dpi, 1955 ± 18 AU at 30 dpi; *p = 0.02, paired t-test; n = 4 mice).

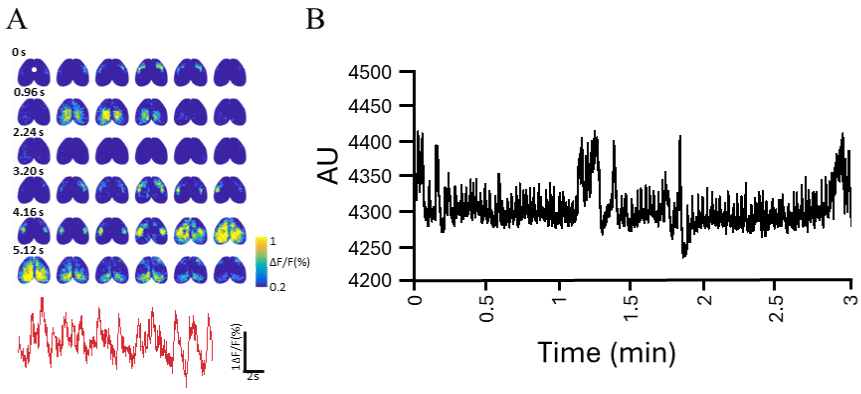

Figure 1.15. jRCaMP1b functionality.
(A) Left: Representative image sequence of jRCaMP1b resting state cortical activity. White dot represents bregma, scale bar: 1mm. Right: Representative trace of jRCaMP1b activity averaged from the same ROI of panel B.s. White dot represents bregma, scale bar: 1mm.
(B) Representative raw trace of resting state fluorescence of the jRCaMP1b indicator within a 3 -minutes window.

The uniform cortical expression enabled reliable WFFI across the dorsal cortex (Fig 1.15A). Importantly, no photobleaching was observed during red-light illumination in any 3-minute imaging window (Fig. 1.15B).

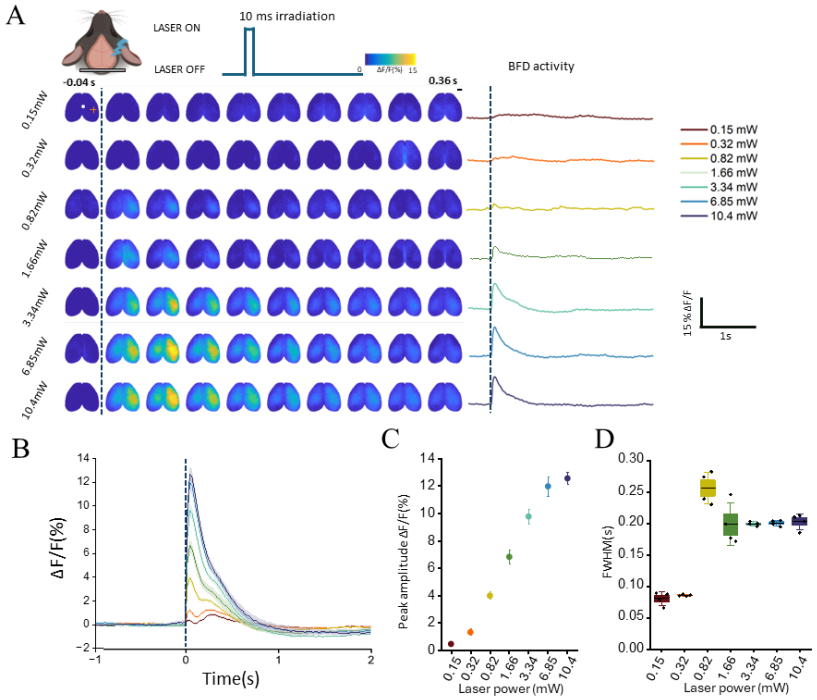

Figure 1.16. Single-pulse light irradiation.
(A) Left: Representative image sequence of cortical activity before and after 10-ms blue-light irradiation on the barrel-field (BFD) at increasing laser power. Frame with optogenetic back-scattering is removed. Dashed line represents the stimulation time point. White dot represents bregma. Orange cross represents the stimulated site. Scalebar: 2mm. Right: Representative traces of BFD activity at increasing laser power. Dashed line represents the stimulation time point.
(B) BFD activity before and after 10-ms blue-light irradiation (dashed line) at increasing laser power.
(C-D) Quantification of peak amplitude (C) and FWHM (D) at increasing laser power.

Calibration of single pulse optogenetic irradiation

To assess the dynamics of light-evoked responses, we applied brief (10 ms) pulses of blue light over the BFD at increasing laser powers (Fig. 1.16A). This protocol consistently evoked a

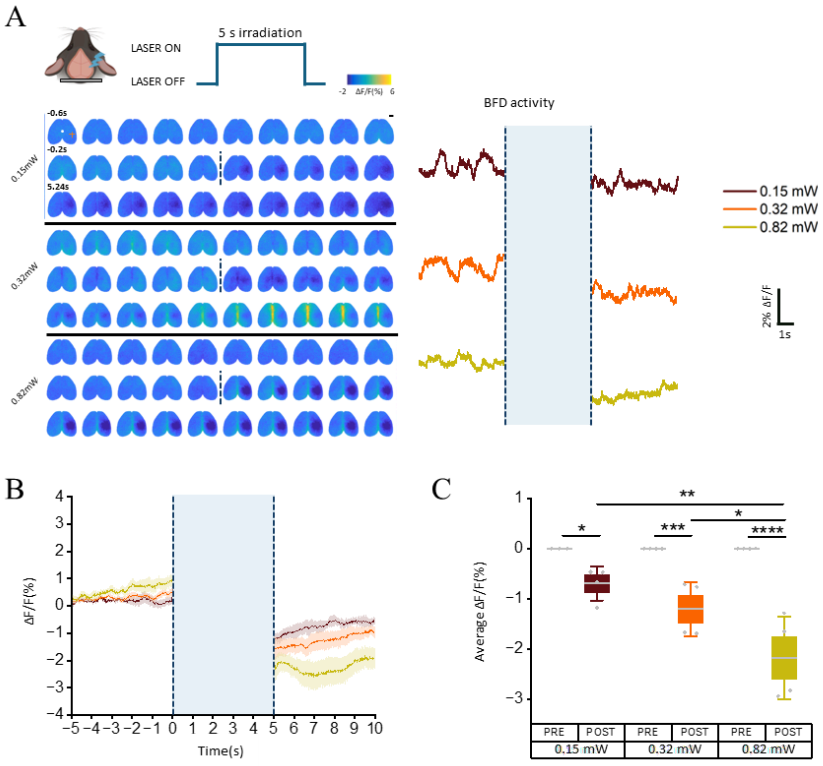

Figure 1.17. 5s irradiation at different powers in mice injected with both jRCaMP1b and stGtACR2.
(A) Left: Representative image sequence of cortical activity before and after 5-s blue-light irradiation on the BFD at increasing laser power. Frames with optogenetic back-scattering are removed. Dashed line represents the removed stimulation interval. White dot represents bregma. Orange cross represents the stimulated site. Scalebar: 2mm. Right: Representative traces of BFD activity at increasing laser power. Dashed lines represent the stimulation interval.
(B-C) Averaged BFD activity before and after 5-s blue-light irradiation at different laser power (B) with relative quantification of average ΔF/F (C). Dashed lines represent the stimulation interval.

transient increase in fluorescence immediately after the stimulus, with response amplitude scaling with laser power (Fig. 1.16B), in agreement with prior in vivo studies (Mahn et al., 2016, Wiegert et al., 2017). No detectable activation was observed at low laser intensities (0.15 and 0.32 mW), while significant increases in post-stimulus activity emerged from 0.82 mW upwards (Fig.

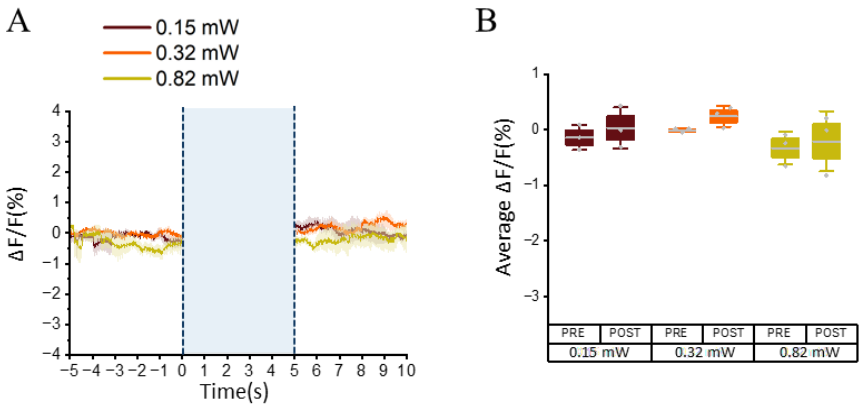

Figure 1.18. 5s irradiation at different powers in the sham group.
Averaged BFD activity before and after 5-s of optogenetic stimulation at different laser power (A) with relative quantification of average ΔF/F (B) in the sham group. Dashed lines represent the stimulation interval

1.16C) (0.15 mW: 1.2 ± 0.14%; 0.32 mW: 1.6 ± 0.13%; 0.82 mW: 4.6 ± 0.29%; 1.66 mW: 7.3 ± 0.44%; 3.34 mW: 10.3 ± 0.45%; 6.85 mW: 12.3 ± 0.68%; 10.4 mW: 13.11 ± 0.32%; n = 4 mice, N = 10 stimulations per mouse). In terms of response kinetics, significant differences in FWHM were also observed between lower and higher power levels, with a notable increase at 0.82 mW and above (Fig 1.16D). However, among higher powers, FWHM remained stable, except for a significant difference between 0.82 and 6.85 mW.

5 s illumination: laser-power dependent suppression of cortical activity

To determine the effect of sustained illumination on cortical suppression, we delivered 5-second light pulses at three power levels: 0.15, 0.32, and 0.82 mW (Fig. 1.17A). During the post stimulation window, a significant suppression of neuronal activity was observed in the BFD for all tested powers, with stronger inhibition corresponding to higher intensities (Fig. 1.17B-C) (0.15 mW: PRE: 0.001 ± 5.9×10^{-4}%; POST: −0.69 ± 0.17%; 0.32 mW: PRE: 7.8×10^{-4} ± 1.5×10^{-4}%; POST: −1.21 ± 0.27%; 0.82 mW:

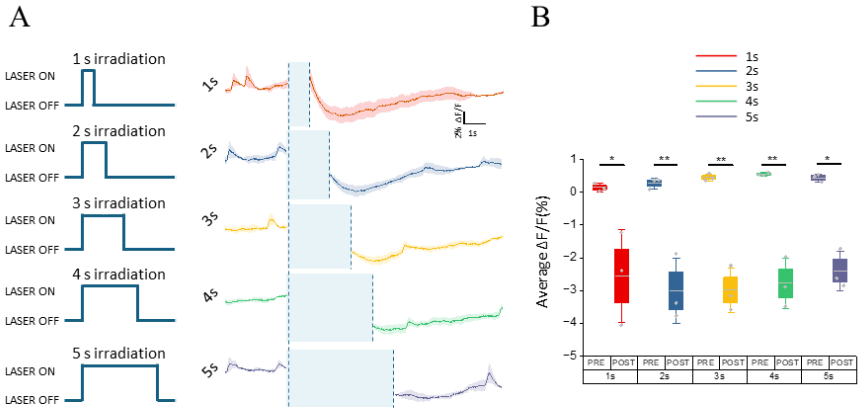

Figure 1.19. 0.82 mW irradiation at different time durations in mice injected with both jRCaMP1b and stGtACR2.
(A) Averaged BFD activity before and after optogenetic stimulation at different durations. Dashed lines represent the stimulation interval.
(B) Quantification of average ΔF/F 5s before (PRE) and after (POST) stimulation in the jRCaMP1b + stGtACR2 group.

PRE: $0.001 \pm 5.6\times10^{-4}$%; POST: -2.17 ± 0.41%; two-way repeated measures ANOVA, Bonferroni correction; n = 4 mice, N = 10 stimulations each). Importantly, this optogenetic suppression was absent in sham animals expressing only jRCaMP1b, indicating that the observed inhibition is stGtACR2-dependent (Fig. 1.18).

Effects of optogenetic inhibition across 1-5 s durations

Using the highest calibrated power (0.82 mW), we next tested the impact of varying the duration of stimulation (1 to 5 seconds) on cortical inhibition. We found that even the shortest stimulation duration (1 s) induced a significant reduction in fluorescence. However, extending the duration beyond 1 second did not yield stronger inhibition (Fig. 1.19) (1 s: PRE: 0.14 ± 0.07%; POST: -2.5 ± 0.8%; *p = 0.018; 2 s: PRE: 0.27 ± 0.09%; POST: -3.00 ± 0.57%; **p = 0.005; 3 s: PRE: 0.45 ± 0.06%; POST: -2.98 ± 0.39%; **p = 0.003; 4 s: PRE: 0.55 ± 0.03%; POST: -2.77 ± 0.44%; **p = 0.004; 5 s: PRE: 0.44 ± 0.07%; POST:

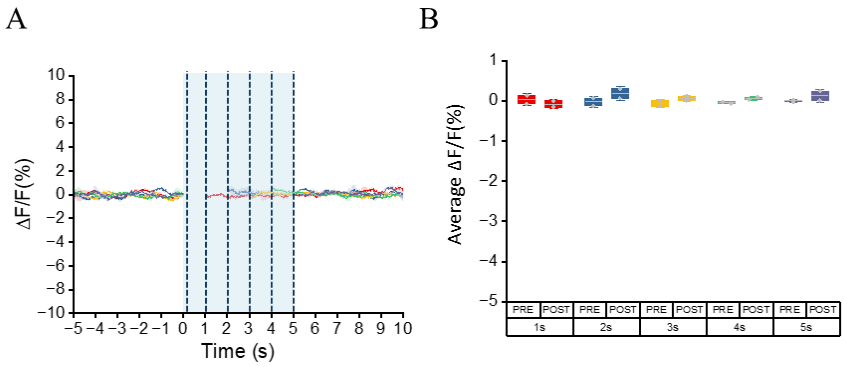

Figure 1.20. 0.82 mW irradiation at different time durations in the sham group.
Averaged BFD activity before and after different durations of optogenetic stimulation (A) with relative quantification of average ΔF/F (B) in the sham group. Dashed lines represent the stimulation interval.

−2.39 ± 0.34%; *p = 0.01; two-way repeated measures ANOVA, Bonferroni correction; n = 3 mice, N = 10 stimulations each). In contrast, no significant differences were observed at any duration in sham animals (jRCaMP1b only), confirming the specificity of the inhibition (Fig 1.20).

Taken together, these results demonstrate that this optogenetic tool can silence excitatory cortical neurons and monitor the resulting effects across the dorsal cortex.

Discussion

In this first chapter, we characterized two different indicators for monitoring cortical activity in mice. Several techniques can be employed for this purpose, including 2PEF, WFFI, and fMRI. Since our primary goal was to capture large-scale cortical dynamics in vivo, we chose WFFI in combination with GECIs, which provides both high temporal resolution and coverage of extended cortical areas. To achieve robust and homogeneous expression of the indicators, we employed systemic delivery of

PHP.eB AAV vectors encoding two different genetically encoded calcium indicators. This strategy allowed us to simultaneously monitor neuronal population activity across the dorsal cortex with high sensitivity and over extended periods, while avoiding the invasiveness of local microinjections.

First, we employed mesoscale cortical imaging using GCaMP7f to investigate excitatory neuron activity across three different brain states, tracking developmental changes from late adolescence to adulthood. To achieve widespread and stable expression of the calcium indicator throughout the dorsal cortex, we performed a retro-orbital injection of AAV-PHP.eB-GCaMP7f at P30, which showed strong tropism for layer V pyramidal neurons (Fig. 1.6, Fig. 1.7). This approach provides a reliable method for longitudinal monitoring of cortical activity (Michelson et al., 2019) and avoids the high costs and lengthy breeding times associated with generating genetically modified mice expressing GECIs (Grodem et al., 2023).

Compared to other members of the jGCaMP7 family, jGCaMP7f offers a favorable balance between sensitivity and temporal precision. While jGCaMP7s and jGCaMP7b display higher brightness and improved detectability in fine processes, and jGCaMP7c provides reduced background fluorescence in large neural ensembles, jGCaMP7f combines fast kinetics with high sensitivity, making it particularly suited for measuring rapid and transient cortical activity (Dana et al., 2019). Importantly, systemic viral delivery of jGCaMP7f resulted in stable cortical expression without adverse signs of cytotoxicity over several weeks, consistent with other studies using GCaMP7 variants in vivo (Grodem et al., 2023, Sato et al., 2015, Dana et al., 2019). These properties are crucial when both speed and sensitivity are required, highlighting the suitability of jGCaMP7f for large-scale cortical imaging of spontaneous and stimulus-evoked activity patterns.

In parallel, we developed a novel all-optical strategy that utilizes the jRCaMP1b indicator to monitor the extent of cortical inhibition mediated by stGtACR2. Previous all-optical approaches have mainly depended on intracranial AAV injections (Resta et al., 2022, Forli et al., 2019) or the use of voltage-sensitive dyes in transgenic mice expressing ChR2 (Lim et al., 2012, Lim et al., 2014). Alternative large-scale techniques, including electrophysiology and voltage imaging, are limited either by the small number of accessible recording sites, which reduces spatial resolution, or by poor signal sensitivity. By contrast, our method provides both high sensitivity and high spatial resolution, enabling reliable single-trial measurements with detailed spatiotemporal resolution.

Through a single systemic injection of a mixed solution containing two PHP.eB viral vectors, we achieved co-expression of jRCaMP1b and stGtACR2 in mice, resulting in homogeneous and stable expression across the cortex, while avoiding the tissue damage caused by invasive intracranial injections reported in earlier work (Hamodi et al., 2020, Lohani et al., 2022, Vinogradova et al., 2020). Unlike previous optogenetic tools, which often produced unintended excitatory side effects due to off-target activation (Mahn et al., 2016, Wiegert et al., 2017), stGtACR2 is specifically designed to minimize axonal activation while maintaining strong somatic inhibition (Mahn et al., 2018). This selectivity is critical for establishing causal links between neuronal silencing and cortical dynamics. A potential limitation, however, is the progressive increase in stGtACR2 expression over time (Fig. 1.14B), which raises concerns about possible toxicity.

Consistent with earlier findings (Li et al., 2019, Kinsky et al., 2023), we observed a rebound in local activity following 10-ms light stimulation, with the rebound amplitude scaling with light intensity (Fig. 1.16). This effect could stem from either intracellular chloride efflux or proton influx after light offset, leading to rapid membrane depolarization (Mahn et al., 2016,

Wiegert et al., 2017). Supporting this interpretation, recent single-cell inhibition studies with stGtACR2 also described paradoxical local excitation (Kinsky et al., 2023, Watkins de Jong et al., 2023). Importantly, our experiments further demonstrate that stGtACR2-mediated inhibition robustly and power-dependently suppresses spontaneous activity in the BFD, lasting up to 5 seconds after stimulation (Fig. 1.17, Fig. 1.19).

In the next section, we will use GECIs to investigate cortical deficits in a mouse model of autism.

Behavioral And Cortical Dysfunctions Of Shank3b+/- Mouse Model Of Autism

Introduction

Autism Spectrum Disorders

Autism spectrum disorders (ASD) are a group of neurodevelopmental conditions characterized by persistent deficits in social interaction and communication, along with restricted, repetitive, and atypical behaviors (Lord et al., 2018). These disorders are frequently associated with intellectual disability, language delays, and various cognitive impairments (Takumi et al., 2020). Since ASD is considered a spectrum disorder, individuals present substantial heterogeneity not only in symptom severity but also in the particular combination of behavioral and cognitive features.

Epidemiological studies estimate that ASD affects approximately 1% of the global population, with a higher prevalence in males. Despite extensive research, its etiology remains only partially understood. However, converging evidence indicates a central role for genetic factors in its development. For example, in a study involving 277 twin pairs (67 monozygotic and 210 dizygotic), ASD concordance was 88% among monozygotic twins but only 31% among dizygotic twins, underscoring the strong hereditary component (Rosenberg et al., 2009). At the same time, non-genetic influences – such as environmental factors, perinatal complications, and gene–environment interactions – are also thought to contribute to phenotypic variability and may help explain the broad range of clinical manifestations observed across individuals with ASD.

Phelan-McDermid Syndrome

Phelan–McDermid syndrome (PMS), also known as 22q13.3 deletion syndrome, is a rare neurodevelopmental disorder first described in the 1980s (Watt et al., 1985). It is caused by deletions or mutations in the distal region of chromosome 22 at 22q13.3,

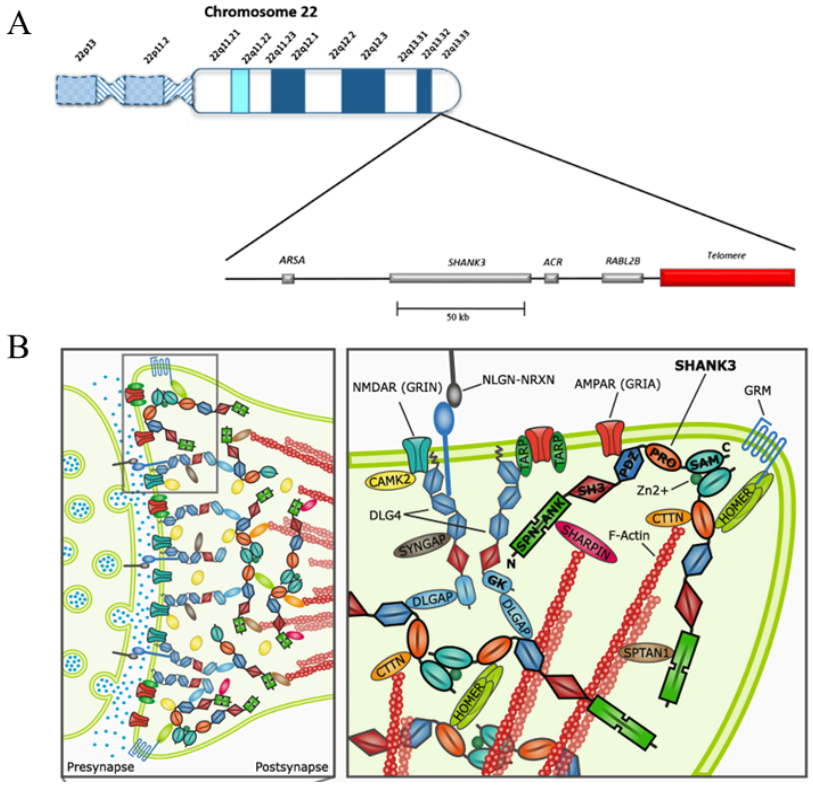

Figure 2.1. Shank3 gene and protein.
(A) Chromosome 22. The short (p) and long (q) arms of chromosome 22 are shown schematically, together with mapped regions of special significance. ARSA, SHANK3, ACR, and RABL2B (the genes found in region 22q13.3) are shown linearly, along with their corresponding sizes. Modified from Costales and Kolovzon, 2015.
(B) SHANK3 localizes to the postsynaptic density (PSD) of glutamatergic synapses, a protein-rich, electron-dense structure beneath the postsynaptic membrane. SHANK3 interacts with multiple partners through six functional domains (SPN, ANK, SH3, PDZ, PRO, and SAM), illustrated in the figure. MAGUK proteins such as DLG4 (PSD95) act as key organizers of the PSD, linking SHANK3, DLGAP, and HOMER to metabotropic glutamate receptor (GRM) and NMDA receptor (NMDAR) complexes. SHANK3 further connects these complexes to the cytoskeleton via interactions with proteins including CTTN and SPTAN1, whose binding is regulated by the SPN domain. Through interactions with the ARP2/3 complex and related actin-regulatory pathways, SHANK3 may modulate actin dynamics. Abbreviations: PSD, postsynaptic density; SPN, SHANK/ProSAP/N-terminal; SH3, Src homology 3; PDZ, PSD95/DlgA/ZO-1; PRO, proline-rich; SAM, sterile alpha motif; ANK, ankyrin repeats. Modified from Delling and Boeckers, 2021.

affecting multiple genes but primarily the SHANK3 gene (Bonaglia et al., 2001; Phelan and McDermid, 2011) (Fig. 2.1A and B).

The disorder presents with a spectrum of clinical features that vary in severity, including global developmental delay, intellectual disability, absent or severely delayed speech, hypotonia, and frequent ASD diagnoses (Kolevzon et al., 2014; Costales & Kolevzon, 2015; Harony-Nicolas et al., 2015).

ASD is reported in up to 94% of PMS patients, making it one of the most penetrant monogenic causes of autism (Costales & Kolevzon, 2015; Harony-Nicolas et al., 2015). Diagnosis relies on chromosomal microarray analysis to detect deletions. Smaller deletions or single nucleotide variants in SHANK3 require DNA sequencing for accurate identification (Costales & Kolevzon, 2015; Kolevzon et al., 2014).

The Shank3 mouse model

The genetic basis of PMS is predominantly linked to the haploinsufficiency or disruption of one copy of the SHANK3 gene located at chromosome 22q13.3 (Bonaglia et al., 2001). SHANK3 encodes a scaffolding protein that is a critical component of the postsynaptic density in excitatory synapses and plays a central role in synaptic formation, maintenance, and signaling (Sala et al., 2001; Durand et al., 2012; Han et al., 2013) (Fig. 2.1B).

To investigate the neuronal and behavioral consequences of SHANK3 deficiency, genetically modified mouse models have been generated. In these models, Shank3 heterozygous (HET, +/−) and knockout (KO, −/−) mice are typically compared with wild-type (WT, +/+) controls to characterize the behavioral and neuronal phenotypes underlying PMS (Peca et al., 2011; Bozdagi et al., 2010; Durand et al., 2012).

Behavioral deficits

Across multiple genetic constructs and experimental paradigms, Shank3 mice consistently display a broad range of behavioral abnormalities, many of which parallel core and associated symptoms observed in patients.

- Motor function:

  Shank3 KO mice display marked impairments in motor coordination and endurance, as demonstrated by poor performance on the rotarod and grid hanging tests (Bauer et al., 2023). In the open field, locomotor activity is reduced compared to WT controls (Peca et al., 2011; Delling & Boeckers, 2021).

- Social behavior and communication:

  In the three-chamber sociability test, Shank3 KO mice generally retain a preference for a social partner over an object, but show subtle deficits in social initiation, with most interactions being initiated by the stranger mouse (Peca et al., 2011; Bauer et al., 2023). Direct social interaction paradigms, including the resident-intruder assay, reveal freezing responses and reduced initiation of contact (Wang et al., 2011). Communication deficits are also evident: Shank3 KO males emit fewer ultrasonic vocalizations during social encounters (Wang et al., 2011; Bauer et al., 2023).

- Repetitive and stereotypic behaviors:

  A hallmark phenotype is the strong increase in self-grooming observed in homozygous KO mice, often considered a robust ASD-like trait (Delling & Boeckers, 2021). Other repetitive behaviors are also affected: Shank3 KO mice show reduced digging when placed in a fresh standard cage with bedding material, particularly in

males, and increased nestlet shredding activity (Bauer et al., 2023).

- Anxiety and avoidance behaviors:

  In the open field, Shank3 KO mice spend significantly less time in the center, reflecting elevated anxiety-like behavior (Delling & Boeckers, 2021). Similarly, in the marble burying test, they frequently fail to bury marbles, an index of altered anxiety and avoidance (Bauer et al., 2023).

- Cognitive function:

  Spatial learning and memory, assessed with the Barnes maze, are largely intact at baseline (Bauer et al., 2023). However, deficits emerge in reversal learning tasks probing cognitive flexibility: adult female KO mice in particular exhibit longer latencies to locate the escape box, indicating impaired adaptability (Bauer et al., 2023).

- Sensory perception:

  Shank3 KO mice also exhibit a complex panel of somatosensory abnormalities associated with tactile stimulation and whisker-dependent texture discrimination (Balasco et al., 2022; Falcão et al., 2024). We will discuss these alterations in detail in Chapter 3.

Heterozygous Shank3 mice generally exhibit milder or absent abnormalities compared to homozygous KOs. In most behavioral domains, they perform similarly to WT animals, though they occasionally show subtle “trend-like” changes, particularly in repetitive behaviors such as self-grooming and marble burying (Wang et al., 2011; Delling & Boeckers, 2021; Bauer et al., 2023).

Neuronal deficits

In addition to behavioral abnormalities, Shank3 deficiency produces profound neuronal and synaptic deficits, reflecting its critical role as a scaffolding protein at excitatory synapses.

At the synaptic level, homozygous knockouts show a marked reduction in excitatory synaptic transmission, with severely impaired AMPA and NMDA receptor function and strongly compromised long-term potentiation (Peca et al., 2011; Wang et al., 2011). These alterations are paralleled by a loss of dendritic spine density and complexity, particularly in striatal and hippocampal neurons, reflecting impaired synaptic maturation and maintenance (Durand et al., 2012; Monteiro & Feng, 2017).

At the molecular level, reductions in postsynaptic density proteins such as Homer, PSD-95, and glutamate receptor subunits highlight the widespread disorganization of the synaptic scaffold (Peca et al., 2011; Wang et al., 2011).

In the cortex, both electrophysiological and two-photon studies further demonstrate imbalances in excitatory/inhibitory signaling, with enhanced glutamatergic inputs and reduced GABAergic tone, leading to network-level dysfunction (Peixoto et al., 2016; Chen et al., 2020, Pagano et al., 2023).

Although milder than in homozygous knockouts, Shank3b+/– mice display clear neuronal and synaptic abnormalities that mirror the haploinsufficiency found in most human patients. Electrophysiological studies reveal reduced excitatory transmission, with decreased AMPA receptor-mediated responses and impaired synaptic plasticity (LTP and LTD) (Bozdagi et al., 2010; Wang et al., 2011; Yang et al., 2012; Kouser et al., 2013).

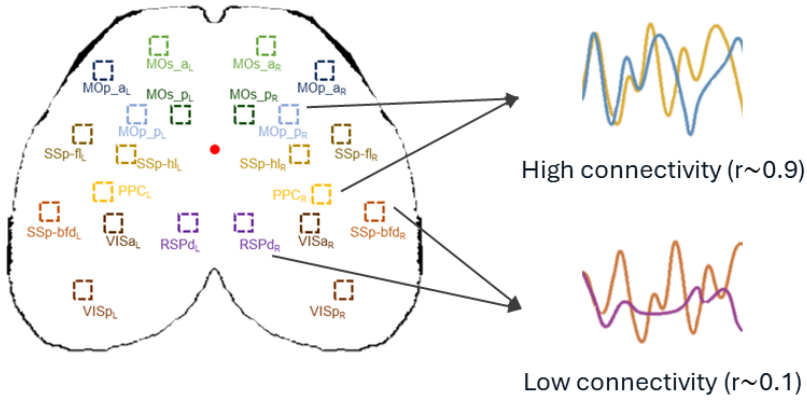

Figure 2.2. Cortical parcellation and functional connectivity.
Brain areas as defined in the Allen Mouse Brain. Traces extracted by areas with high temporal overlap show high connectivity and high Pearson's coefficient (r) while traces with low overlap show low connectivity and low r coefficient.

Structural plasticity is also compromised in Shank3b+/- mice, with impaired activity-dependent remodeling of dendritic spines, reduced Arc expression and abnormal actin regulation (Sarowar & Grabrucker, 2016).

Overall, these findings indicate that even partial loss of Shank3 is sufficient to disrupt synaptic function and plasticity, producing neuronal phenotypes that, while subtler than in homozygous models, are highly relevant to SHANK3-related disorders.

Functional connectivity as a biomarker for ASD

Functional connectivity (FC), defined as the temporal correlation in the activation of distinct brain regions (Ha et al., 2015), has emerged as a promising biomarker for ASD. It can be quantified using correlation coefficients such as Pearson's (r), which reflects the coactivation between two regions, ranging from strongly

positive (+1) to strongly negative (-1) (Scheinost et al., 2017) (Fig. 2.2).

Numerous neuroimaging studies in ASD have reported a pattern of local hyper-connectivity between nearby regions coupled with reduced long-range connectivity (Just et al., 2006; Vasa et al., 2016). However, these findings remain controversial, as other studies have described the opposite trend, with evidence of global hyper-connectivity (Mizuno et al., 2006; Turner et al., 2006, Rinaldi et al., 2007). This variability suggests that connectivity alterations may depend on developmental stage, brain state, or heterogeneity within the ASD population. Importantly, FC has been shown to correlate inversely with the severity of behavioral symptoms (Uddin et al., 2015), highlighting its potential as a translational biomarker.

Preclinical studies in animal models of ASD – both genetic (e.g., CDKL5, MecP2) and pharmacological (e.g., IL-6 exposure) – have further demonstrated disrupted FC (Dasilva et al., 2019; Zerbi et al., 2021), supporting the idea that altered large-scale network dynamics represent a conserved hallmark of the disorder. Recently, FC deficits have been reported in Shank3b-/- mice resulting in a disrupted correlation between hippocampus and somatosensory cortex (Balasco et al., 2021). Together, these findings position FC as a candidate biomarker that bridges mechanistic insights from animal models with clinical characterization in patients, offering a window into the network-level disruptions underlying PMS.

Variations in FC are believed to reflect alterations in the spatiotemporal interactions among cortical regions. Recently, MacDowell and colleagues analyzed cortex-wide neural activity in the valproic acid (VPA) mouse model of autism, quantifying its spatiotemporal dynamics in different ‘motifs’ and finding that individual changes in FC (and behavior) are related to differences in how frequently a motif is expressed (MacDowell et al., 2024).

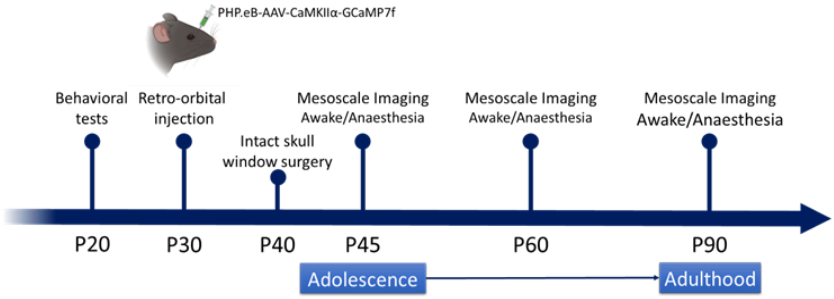

Figure 2.3 Experimental timeline for longitudinal imaging in Shank3b+/+ and Shank3b+/- mice.
Experimental timeline with retro-orbital injection of GCaMP7f, optical window surgery and in vivo imaging at P45, P60 and P90.

In this second chapter, we build upon the techniques introduced in Chapter 1 (specifically WFFI and the GCaMP7f indicator across three different brain states) to characterize FC deficits in the Shank3b+/− mouse model. We selected this model, in which the Shank3b knockout allele carries a neo cassette replacing the PDZ domain (exons 13–16) of the Shank3 gene, because it is widely used in the literature. Moreover, the haploinsufficiency of Shank3b+/- mice more accurately resembles the human condition compared to full KO Shank3b mice, making them a more relevant model for studying cortical alterations (Drapeau et al., 2014; Bauer et al., 2023). After assessing cortical and behavioral deficits independently, we examine how these two are related and how individual motifs contribute to both cortical activity, FC and behavior.

Materials and methods

Mice from both genotypes (Shank3b+/– and Shank3b+/+) were used to perform both behavioral and imaging experiments. Mice were subjected to behavioral testing at postnatal day 20 (P20) to assess early behavioral phenotypes. Ten days later, at P30,

animals received a retro-orbital injection of the PHP.eB-AAV vector to induce the expression of the GCaMP7f calcium indicator. At P40, an intact skull window surgery was performed to enable longitudinal widefield imaging. Mesoscale calcium imaging was subsequently conducted at three developmental stages (P45, P60, and P90) and under three distinct brain states: awake, light anesthesia, and deep anesthesia (Fig. 2.3).

Open field

At P20, open field test was conducted to assess spontaneous exploratory and grooming behavior. Animals were first acclimated to the behavioral room for 2 hours to reduce novelty-induced stress. Each mouse was then allowed to explore an empty arena ($45 \times 45 \times 45$ cm) with uniform white, smooth walls, for 10 minutes. To eliminate residual olfactory cues, the arena was sanitized with a 70% ethanol solution prior to each session. Behavioral activity was captured using a PointGrey FLIR Chameleon3 video camera (CM3-U3-13Y3C-CS) at 30 Hz.

In vivo imaging of cortical activity through GCaMP7f

As described in chapter 1, at P30 mice were injected with a PHP.eB AAV vector to induce the expression of the GCaMP7f indicator. After 10 days, an intact skull window surgery was performed allowing optical access to the mouse cortex. Imaging recordings were performed at three different time points (P45, P60 and P90) and in three different brain states (wakeness, light anesthesia and deep anesthesia). In order to quantify movements during awake imaging sessions, at P60 a camera (PointGrey flir Chameleon3, CM3-U3-13Y3C-CS) was orthogonally placed 10 cm in front of the mouse. The camera recorded at 40 frames per second with a resolution of 512×512 pixels, which provided adequate coverage of the mouse's frontal area for detailed movement analysis. To enhance movement detection, a visible light source at 630 nm was directed onto the forepaws.

Data analysis

All data analyses were performed in MATLAB (MathWorks), Imagej, Python, DeepLabCut, and Origin.

Open field analysis

Grooming behaviors, such as paw-to-face movements, snout cleaning, and body licking, were manually quantified by a trained observer. Finally, videos were also automatically analyzed by Animal Tracker tool (ImageJ) for the measuring of locomotor parameters such as total distance traveled and time spent in the central zone of the arena.

Movements tracking using DeepLabCut

At P60, behavioral videos were analyzed using Python. Alternate frames from each video were taken for the alignment to the imaging recording. The resulting videos were then preprocessed to increase the contrast. Five regions of interest (Eye, Snout, Whisker, Right forepaw and Left forepaw) were tracked with DeepLabCut extracting the spatial (x, y) coordinates for each frame (Mathis et al., 2018).

Imaging analysis

Cortical Parcellation

From preprocessed images (See Chapter 1), a total of 22 ROIs were then selected (11 ROI for each hemisphere, 10x10 pixels). The abbreviations and extended names for each areas are as follows: MOs-a, anterior region of secondary motor cortex; MOs-p, posterior region of secondary motor cortex; MOp-a, anterior region of primary motor cortex; MOp-p, posterior region of primary motor cortex; SSp-bfd, primary somatosensory area, barrefield; SSp-fL, primary somatosensory area, forelimb; SSp-hl, primary somatosensory area, hindlimb; PPC, posterior parietal

cortex; RSPd, retrosplenial cortex; VISa, associative visual cortex; VISp, primary visual cortex. Throughout the text and figures, suffixes L and R were added to denote cortical areas of the left or right hemisphere, respectively (e.g., MOp-a_L, MOp-a_R) (Fig. 2.2).

Resting state functional connectivity

FC mapping was performed individually for each subject by computing Pearson's correlation coefficients between the average fluorescence signal of a given ROI and those of all other ROIs, using a 180-second time window. Correlation values were then averaged across imaging sessions. To facilitate group-level comparisons, individual correlation matrices were transformed using Fisher's r-to-z transformation and subsequently averaged across animals within each experimental group. The resulting group-averaged matrices were then converted back to correlation coefficients (r-values).

To assess differences in FC between genotypes, contrast matrices were generated by subtracting the mean r-values of Shank3b+/- from those of heterozygous mice Shank3b+/-, for each ROI pair and time point. In FC graphs, ROI positions were arranged based on their anatomical coordinates. The strength of each connection was represented by the thickness of the connecting lines, while symbol size reflected the number of significant connections associated with each ROI.

We then used the Network-Based Statistic (NBS) method to assess significant changes in connectivity (Zalesky et al., 2010).

Motifs analysis

Preprocessing

After ΔF/F and hemodynamic correction (See Chapter 1), images were resized to 64×64 pixels and aligned to a 2D projection of the

Allen Brain Atlas using bregma and lambda coordinates. The recordings were then band-pass filtered between 0.4 and 4 Hz (Nietz et al., 2022; Brier et al., 2022) and masked. Subsequently, we performed pixel-wise deconvolution of the ΔF/F signal to estimate neural activity using Lucy–Richardson deconvolution (lucid function from Stern et al.; kernel parameters: gamma = 0.95, smt = 1, p_num = 30), which provides a more accurate estimation of the underlying neural activity. After deconvolution, pixel values were normalized to a range between zero and one. A total of four 180-second recordings were obtained for each mouse for motif discovery. Each recording was divided into two 90-second epochs, with alternating epochs used for motif discovery and testing.

Motifs discovery

To identify spatiotemporal sequences in widefield imaging data, we employed the seqNMF algorithm (MATLAB toolbox described in Mackevicius et al., 2019). This method is based on convolutional non-negative matrix factorization (CNMF), with an added regularization term that promotes the discovery of repeating patterns. The following method and equations are adapted by MacDowell & Buschman, 2020 from Mackevicius et al., 2019.

Each image was treated as a P×1 vector, where P is the number of pixels. A sequence of images (i.e., a recording epoch) was represented as a P×T matrix, where T is the number of time points. This matrix was factorized into K smaller matrices of size P×L, each representing short spatiotemporal motifs. These motifs collectively form a tensor W of dimensions P×K×L, and their temporal activations are represented by a matrix H of size K×T. The original data are approximated by the sum of convolutions between each motif and its corresponding temporal activation:

$$X_{pt} \approx \sum_{k=1}^{K} \sum_{l=0}^{L-1} W_{pkl} H_{k(t-l)} \equiv (W * H)_{pt} \quad \text{(Equation 2)}$$

The matrices W and H were optimized using a multiplicative update algorithm. The parameters L (motif duration) and K (number of motifs) are critical for the factorization. Values of L and K that are too small may constrain motif discovery – leading to overly short motifs or merging of distinct motifs – while excessively large values do not bias the solution, as unused motifs or time points are suppressed through CNMF regularization. However, large values increase computational load.

We used L=20 frames (1s), a value chosen to be consistent with previous reports (MacDowell & Buschman, 2020). The number of motifs was set to K=28, which exceeded the maximum number of motifs identified in any single epoch and did not constrain the number of discovered motifs. Variation of K within reasonable ranges had minimal impact on the results (MacDowell & Buschman, 2020).

To reduce redundancy among discovered motifs, seqNMF includes a spatiotemporal penalty in the cost function:

$$R = \lambda \left|\left| (W * X) SH^T \right|\right|_{1, i \neq j} \quad \text{(Equation 3)}$$

This term discourages multiple motifs from describing the same sequence, prevents single motifs from being split across time, and encourages temporal independence. The matrix S, of size T×T, is a temporal smoothing matrix where Sij=1 when |i-j| < L and 0 otherwise.

Measuring the overlap between the motifs and the original data is useful to calculate the competition between motifs:

$$(W * X)_{kt} = \sum_{l} \sum_{p} W_{pkl} X_{p(t+l)} \quad \text{(Equation 4)}$$

The notation $\| \cdot \| 1, i \neq j$ excludes diagonal elements, avoiding penalization of self-similarity within motifs. The parameter lambda (λ) controls the strength of this penalty. We used λ=0.0005, which provided a good balance between reconstruction accuracy, motif separation, and the number of motifs discovered according to MacDowell & Buschman, 2020.

An optional orthogonality constraint was applied to encourage event-based (i.e., temporally distinct) motifs, which is well-suited for widefield imaging data. This was implemented through an additional cost term penalizing overlap in the temporal activations:

$$R_{Hortho} = \frac{\lambda_{Hortho}}{2} \left|\left| HSH^T \right|\right|_{1, i \neq j} \quad \text{(Equation 5)}$$

Here, λ_{Hortho} was set to 1 based on preliminary trials and kept constant for all analyses. All factorizations were run for 300 iterations, which was sufficient for convergence of the cost function as in MacDowell & Buschman, 2020.

A complete list of the seqNMF parameters used is provided in Table 1.

Refitting Motifs to Withheld Data

To evaluate motif expression in unseen data, we refit the previously identified motifs to withheld datasets using the seqNMF algorithm. During this process, the spatial components W (i.e., the basis motifs) were held fixed, and only the temporal coefficients H were updated. This approach restricted the factorization to adjusting the timing of motif activations, without altering their spatial structure. The full list of parameters used during refitting is available in Table 1.

Since only the temporal weights were optimized, the regularization parameter λ was set to zero. As a result, unlike the

motif discovery step, which included constraints to enforce spatial and temporal independence among motifs, refitted motifs were not subject to such penalties. Consequently, some degree of combinatorial activation across motifs was observed.

Generating Basis Motifs

To extract representative motif patterns, we applied an unsupervised clustering approach using the Phenograph algorithm (Levine et al., 2015). Before clustering, motifs were rescaled to a [0, 1] range and smoothed in space and time using a 3D Gaussian filter with standard deviation $\sigma=[1,1,0.1]$.

Phenograph constructs a directed graph in which each node (i.e., a motif) is connected to its k nearest neighbors, based on the pairwise similarity of their temporal structure. Similarity was defined as the peak of the temporal cross-correlation between motif time series. The graph was then partitioned into clusters using the Louvain community detection algorithm. The only adjustable parameter in Phenograph is the number of nearest neighbors, k, which was set to 17 based on preliminary analyses.

To create basis motifs, we averaged the core set of motifs within each cluster. The core community was defined as the top 10% of motifs with the highest number of within-cluster nearest neighbors. Before averaging, motifs were aligned to a reference (template) motif within the cluster. This template was selected as the motif with the greatest number of high zero-lag cross-correlations with other motifs in the group. If multiple candidates were present, one was selected at random.

Each motif was zero-padded to a length of 3L (i.e., 60 time points) to account for potential temporal offsets, and then aligned to the template based on the lag at which cross-correlation was maximal. Basis motifs were obtained by averaging the aligned core motifs over time.

Finally, the basis motifs were mutually aligned by centering the temporal profile of each motif – specifically, shifting the center of mass of activity to the midpoint of the time window. Time points with zero variance across all basis motifs were excluded, resulting in final basis motifs with a maximum duration of 40 time points (approximately 2 seconds). A full description of each basis motif, including its temporal extent and dominant activity pattern, is provided in Table 1.

Evaluating motifs expression

In all analyses, the percent explained variance (PEV) was used to quantify how well the reconstructed data captured the original neural activity. It was computed as:

$$PEV = 100 * \left(1 - \frac{(\sigma_x^2 - \sigma_{x^-}^2)}{\sigma_x^2}\right) \quad \text{(Equation 6)}$$

where σ_x^2 and represents the total spatiotemporal variance of the original data, and $\sigma_{x^-}^2$ is the variance of the data reconstructed from the factorization.

To evaluate the contribution of individual motifs, each motif was convolved with its corresponding temporal activation, and the PEV was computed using the same formula. As a result, the PEV for individual motifs reflected both how often the motif occurred and how well it matched the underlying neural dynamics (aka expression).To express the relative contribution of each motif, its individual PEV was divided by the total PEV explained by all motifs during that epoch.

	Motifs Discovery	Motifs Refit
K	28	17 (# basis motifs)
L	20	20
λ	0.0005	0
W	Random	Basis Motifs
H	Random	Random
λ_{Hortho}	1	1
λ_{Wortho}	0	0
Iterations	300	100
Wfixed	0	1
Wupdated	1	0

Table1. CNMF parameters used for discovery and refitting.

Correlation between cortical dynamic and movements

Motion energy of global movements

Adapted from Hasnain and colleagues, the motion energy for a given frame and ROI was defined as the absolute value of the difference between the value of the coordinates of that frame and the next frame. The global movement for each frame was then defined as the sum of motion energy values across all selected ROIs, yielding a global index of motor activity. This approach is sensitive to rapid, localized movements (e.g., forepaws) while remaining relatively unaffected by slow and widespread changes such as those associated with respiration. (Hasnain et al., 2024)

Motion energy of cortical activity

In order to quantify the global cortical dynamic from the preprocessed images, the motion energy for a given frame and pixel was computed as the absolute value of the difference between consecutive frames, resulting in a matrix of size pixels × time points. The cortex dynamic for each frame was then calculated as the square of the sum of the motion energy for each frame.

Cross-correlation

For each epoch, the resulting motion energy traces of movements and cortical activity were finally aligned. At different lags (± 45) a Pearson's correlation coefficient was calculated and then averaged within epochs and genotypes.

Statistical analysis

Two sample t test was used when comparing differences between genotypes (behavior, number of motifs, relative PEV and correlation between cortical dynamics and movements). NBS Toolbox in MATLAB was used to statistically assess functional network connectivity. Two way ANOVA was used to compare differences in global FC between time points. One way ANOVA

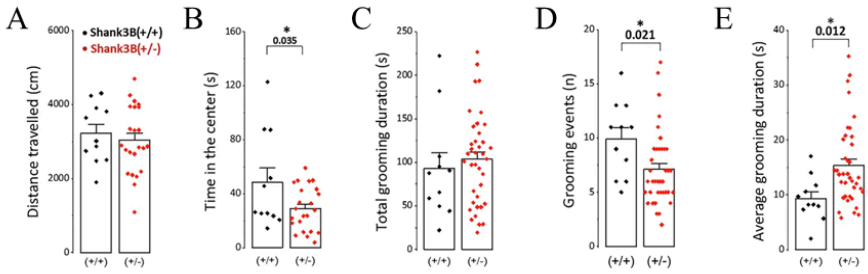

Figure 2.4. Quantification of open field performance of Shank3B+/+ and Shank3B+/- mice.
(A) Total distance travelled
(B) Time spent in the center of the arena
(C) quantification of the total amount of self-grooming grooming
(D) quantification of the number of self-grooming events (n) performed
(E) Averaged duration of a single self-grooming event.

was used to compare FC differences. Two way RM ANOVA followed by Tukey correction was used for differences in PEV within and between mice. Differences were considered significant when $p<0.05$. Errors are reported as Standard Error of Means, *$p<0.05$, **$p<0.01$, ***$p<0.001$.

Results

Adolescent Shank3b mice show increased anxiety and altered grooming patterns

Previous studies assessing Shank3b mutant mice from postnatal day 45 up to 6 months of age have reported various behavioral impairments (Orefice et al., 2019; Balasco et al., 2022; Peca et al., 2011; Bauer et al., 2023). To investigate whether similar abnormalities are present earlier in development, we examined Shank3b+/− and WT mice at postnatal day 20. Anxiety-like behavior and general locomotion were assessed using the open field test. While Shank3b+/− mice covered distances comparable to their Shank3b WT littermates (Shank3b+/+, 3220 ± 240 cm

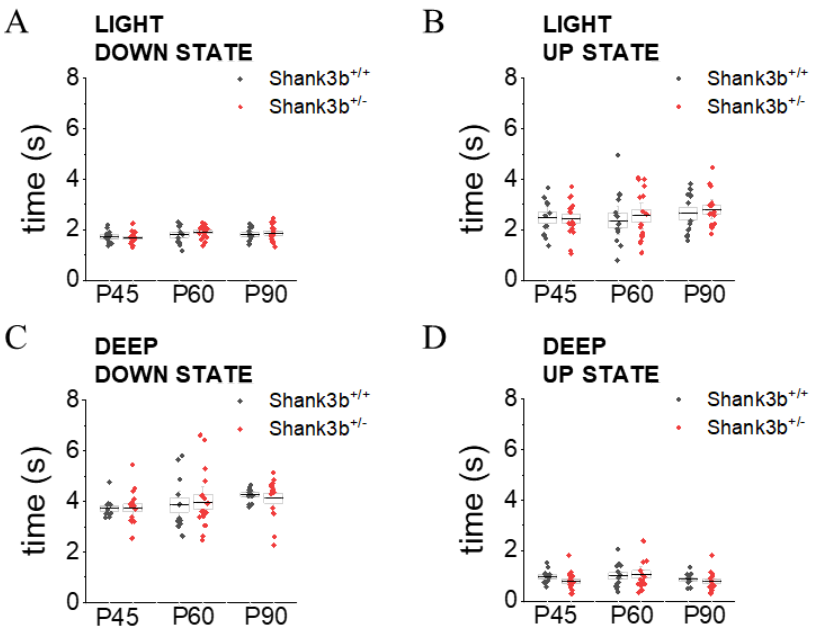

Figure 2.5 Differences in temporal dynamics of anesthetized brain states between genotypes.
(A-B) Average down state duration (A) and up state duration (B) under light anesthesia in Shank3b+/+ (black) and Shank3b+/- (red) mice.
(C-D) Average down state duration (C) and up state duration (D) under light anesthesia in Shank3b+/+ (black) and Shank3b+/- (red) mice.

n=11; Shank3b+/- 3034 ± 188 cm n=23, two-sample t-test) (Fig. 2.4A), they spent significantly less time in the center of the arena (Shank3b+/+ = 48 ± 10 s n=11; Shank3b+/- = 29 ± 3 s n=11, *p = 0.035, two-sample t-test) (Fig. 2.4B), suggesting increased anxiety in the absence of motor impairments. Consistent with previous findings (Orefice et al., 2019; Liu et al., 2024), total grooming duration did not differ significantly between genotypes (93 ± 18 s n=11 Shank3b+/+, 103 ± 8 s n=38 Shank3b+/-, two-sample t-test) (Fig. 2.4C). However, Shank3b+/− mice exhibited fewer grooming bouts (Shank3b+/+ = 9.9 ± 1.0 n n=11, Shank3b+/- = 7.1 ± 0.5 n=38, *p = 0.021, two-sample t-test) (Fig. 2.4D) and a marked tendency toward longer individual grooming episodes (Shank3b+/+ = 9 ± 1 s n=11, Shank3b+/- = 15

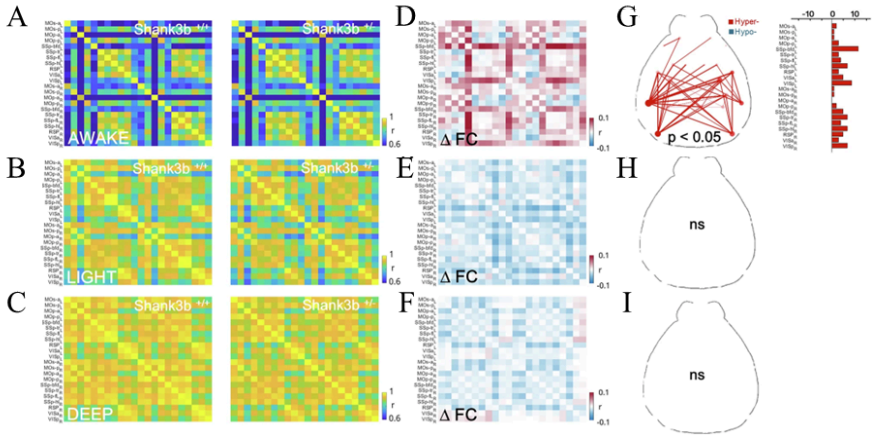

Figure 2.6. Functional connectivity in adolescent mice (P45).
Averaged correlation matrices for genotype (Shank3b+/+ left, Shank3b+/− right) in wakefulness (A), light anesthesia (B), and deep anesthesia (C) were used to display Pearson's correlation coefficients of cortical activity during a 3-minute window. The average FC of Shank3b+/+ mice in the awake condition (D), light anesthesia (E), and deep anesthesia (G) is subtracted from that of Shank3b+/− mice to create the d–f matrix of difference. Shank3b+/-hyper- or hypo-connectivity is indicated by red and blue squares, respectively. g–i Network diagrams demonstrating statistically significant FC changes in light anesthesia (H), deep anesthesia (I), and the awake condition (G) are shown on the left. The number of significant FC modifications for each cortical area is shown in the bar plot on the right. Shank3b+/+ = 11 and Shank3b+/− = 17. NBS. $p < 0.05$ is the statistical test.

± 1 s n=38, *p = 0.012, two-sample t-test) (Fig. 2.4E). These results indicate that although the overall amount of grooming is unaffected, Shank3b+/− mice display difficulties in terminating repetitive behaviors, pointing to specific grooming impairments.

Wild-type and mutant mice share the same temporal dynamics under anesthesia

As demonstrated in Chapter 1, prolonged Up-states and shortened Down-states characterize light anesthesia, whereas deep anesthesia exhibits the opposite pattern (Fig. 1.9 B-E). Here, we found the same trend across genotypes, with no significant differences in Up- and Down- states duration (Fig. 2.5 A-D).

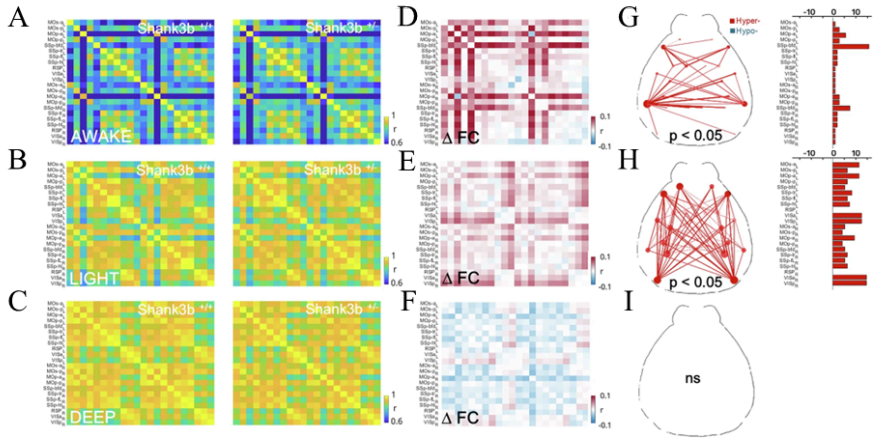

Figure 2.7. Functional connectivity at P60.
Averaged correlation matrices for genotype (Shank3b+/+ left, Shank3b+/− right) in wakefulness (A), light anesthesia (B), and deep anesthesia (C) were used to display Pearson's correlation coefficients of cortical activity during a 3-minute window. The average FC of Shank3b+/+ mice in the awake condition (D), light anesthesia (E), and deep anesthesia (G) is subtracted from that of Shank3b+/− mice to create the d–f matrix of difference. Shank3b+/-hyper- or hypo-connectivity is indicated by red and blue squares, respectively. g–i Network diagrams demonstrating statistically significant FC changes in light anesthesia (H), deep anesthesia (I), and the awake condition (G) are shown on the left. The number of significant FC modifications for each cortical area is shown in the bar plot on the right. Shank3b+/+ = 11 and Shank3b+/− = 17. NBS. $p < 0.05$ is the statistical test.

Awake-state hyperconnectivity of the barrel field and visual cortices in adolescent Shank3b mice

As previously reported (Scaglione et al., 2024), resting-state FC increased under deeper levels of anesthesia (Fig. 2.6 A-C), a pattern seen in both genotypes. However, clear genotype-specific differences emerged: during the awake state, Shank3b+/− mice exhibited strong, bilateral hyperconnectivity relative to WT mice (Fig. 2.6D). This hyperconnectivity was especially pronounced in networks involving the barrel cortex (SSp-bfd) and the primary visual cortex (VISp; Fig. 2.6G), potentially explaining the heightened responsiveness to sensory stimuli observed in Shank3b mutants (Balasco et al., 2022). In contrast, under light

(Fig. 2.6E) and deep anesthesia (Fig. 2.6F), FC in Shank3b+/− mice closely resembled that of WT, with only a weak and non-significant trend toward overall reduced connectivity (Fig. 2.6H and I).

These findings highlight a strong brain-state dependency of FC alterations: the prominent hyperconnectivity in Shank3b+/− mice is evident only during wakefulness and is diminished under anesthesia. This emphasizes the importance of accounting for brain state when assessing FC in mutants versus WT mice.

Hyperconnectivity intensifies and extends to motor regions at P60

To examine how cortical networks change over time, we conducted recordings at P60. Notably, in the awake state, the hyperconnected network observed in Shank3b+/− mice at P45 centered around the barrel cortex, became even more pronounced at P60 (Fig. 2.7D and G). In addition, a new FC disruption emerged in the anterior primary motor cortices (MOp-a) in Shank3b+/− mice (Fig. 2.7G).

Unlike the findings at P45, significant hyperconnectivity was also evident during light anesthesia at P60 (Fig. 2.7E), affecting nearly the entire cortical network except for the retrosplenial cortices (RSP; Fig. 2.7H). Under deep anesthesia, a general but mild decrease in FC was observed, although no significant differences between genotypes were detected (Fig. 2.7F and I).

Taken together, these results suggest that the hyperconnected subnetwork, particularly involving the bilateral BFD, persists and

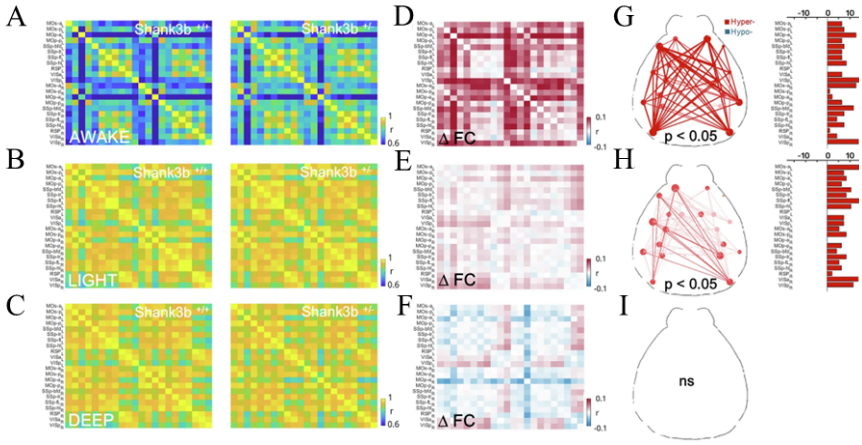

Figure 2.8. Functional connectivity in adult mice (P90).
Averaged correlation matrices for genotype (Shank3b+/+ left, Shank3b+/− right) in wakefulness (A), light anesthesia (B), and deep anesthesia (C) were used to display Pearson's correlation coefficients of cortical activity during a 3-minute window. The average FC of Shank3b+/+ mice in the awake condition (D), light anesthesia (E), and deep anesthesia (G) is subtracted from that of Shank3b+/− mice to create the d–f matrix of difference. Shank3b+/-hyper- or hypo-connectivity is indicated by red and blue squares, respectively. g–i Network diagrams demonstrating statistically significant FC changes in light anesthesia (H), deep anesthesia (I), and the awake condition (G) are shown on the left. The number of significant FC modifications for each cortical area is shown in the bar plot on the right. Shank3b+/+ = 13 and Shank3b+/− = 14. NBS. $p < 0.05$ is the statistical test.

becomes more robust with age during wakefulness. The additional recruitment of motor areas at P60 indicates a progressive worsening of cortical network dysfunction in Shank3b+/− mice over time.

Functional connectivity alterations persist into adulthood

To assess whether FC abnormalities continue from adolescence into adulthood, we recorded cortical network activity at postnatal day 90 (P90). In the awake state, Shank3b+/− mice exhibited a widespread and strongly hyperconnected cortical network (Fig. 2.8D and G), indicating that FC differences between genotypes

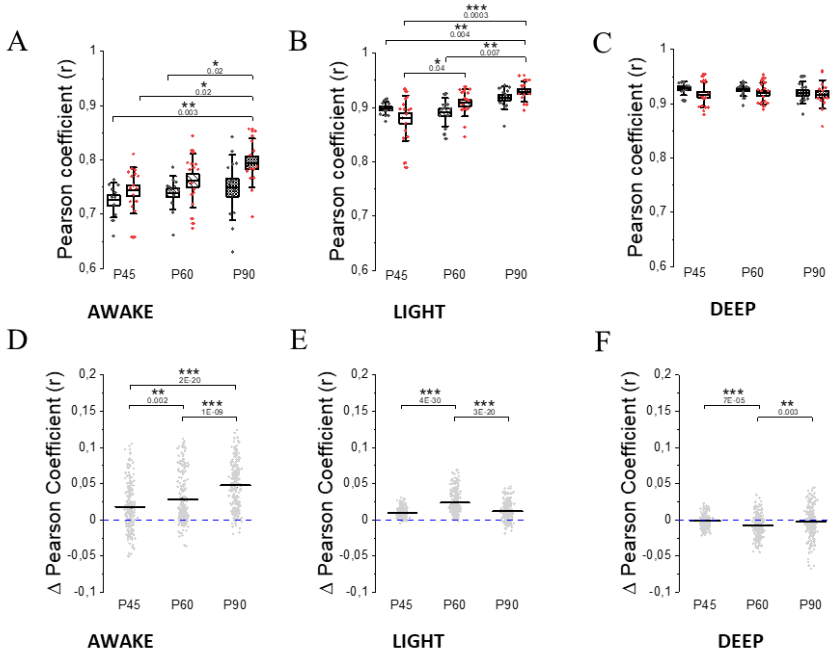

Figure 2.9. Quantification of global FC between genotypes and states.
(A-C) Global functional connectivity box plots in the waking state (A), light anesthesia (B), and deep anesthesia (C) for both genotypes (Shank3b+/+ black, Shank3b+/− red) are shown in the following figures: *p < 0.05; **p < 0.01; ***p < 0.001, two-way ANOVA).
(D-F) Shank3b+/− and Shank3b+/+ person coefficient differences in awake (D), light (E), and deep anesthesia (F) were tracked longitudinally. **p < 0.01; ***p < 0.001, one-way ANOVA; *p < 0.05.

become more pronounced with age. This pattern of hyperconnectivity was also maintained during light anesthesia at P90 (Fig. 2.8E and H). In contrast, under deep anesthesia, Shank3b+/− mice showed a mild, non-significant trend toward reduced connectivity compared to controls (Fig. 2.8F and I).

Overall, these findings demonstrate that FC alterations are strongly influenced by brain state and expand from early adolescence (P45) through adulthood (P90). The continued and progressive hyperconnectivity observed in awake and lightly

anesthetized conditions highlights the enduring and dynamic nature of cortical network dysfunction in Shank3b+/- mice.

Network alterations are most pronounced in the awake state

Since FC disruptions became more widespread between P45 and P90 in both the awake and lightly anesthetized conditions, we tracked how global FC evolved over time in each brain state separately for the two genotypes.

Interestingly, WT mice showed stable global FC across all time points and brain states (Fig. 2.9). In contrast, Shank3b+/− mice displayed a significant increase in global FC from P45 to P90 during both the awake state and light anesthesia (Fig. 2.9A and B). Under deep anesthesia, however, global FC in Shank3b+/− mice followed a similar trend to that of WT, with no significant differences observed (Fig. 2.9C).

Further analysis showed that the differences in FC between genotypes were most prominent in the awake state and became more pronounced with age (Fig. 2.9 D-F). Altogether, these findings reveal that cortical hyperconnectivity in Shank3b+/− mice emerges early in life and becomes stronger over time, particularly in the awake state. Moreover, they underscore that the extent of network imbalance is heavily influenced by brain state, with the most severe disruptions occurring during wakefulness and a shift toward hypoconnectivity under anesthesia.

Shank3b mice have the same number of motifs compared to WT

In a separate batch on animals (N Shank3b+/+ = 7, N Shank3b+/- = 9), we demonstrated that FC deficits are more pronounced during the awake state, so we focused our analysis on P60 awake mice in order to identify neural signal patterns (motifs) that

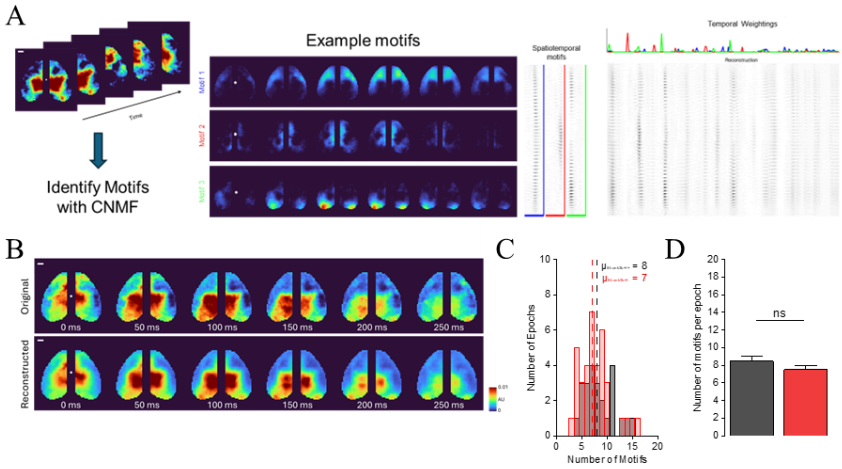

Figure 2.10. Identification of motifs from cortex-wide activity.
(A) Example motifs extracted using CNMF (left), with their corresponding temporal expression profiles (right). The white dot marks the location of bregma; scalebar = 1mm.
(B) Comparison between the original cortical activity and the activity reconstructed from the expression of the discovered motifs. The white dot marks the location of bregma; scalebar = 1mm.
(C) Quantification of the number of motifs identified in each epoch in each genotype (median Shank3b+/+ = 8, median Shank3b+/- = 7).
(D) Average number of discovered motifs in Shank3b+/+ (black) and Shank3b+/– (red) mice.

propagate through the brain. Discovering these spatiotemporal dynamics is essential to determine the contribution of each pattern to cortical and behavioral deficits. To this end, we applied CNMF to recognize motifs in cortical activity and assess differences in their expression between genotypes (Fig. 2.10A).

For each mouse, we analyzed four 3-minute epochs of resting-state activity, using half of each epoch for motif discovery and the other half for evaluation. The reconstructed recordings accurately reproduced the original data (Fig. 2.10B). A total of 461 motifs were identified (Shank3b+/+ = 215, N=7; Shank3b+/- = 246, N=9), with no significant differences in their number between genotypes (Shank3b+/+: 8.45 ± 0.61 AU; Nepochs/Nmice= 28/7; Shank3b+/-: 7.50 ± 0.47 AU;

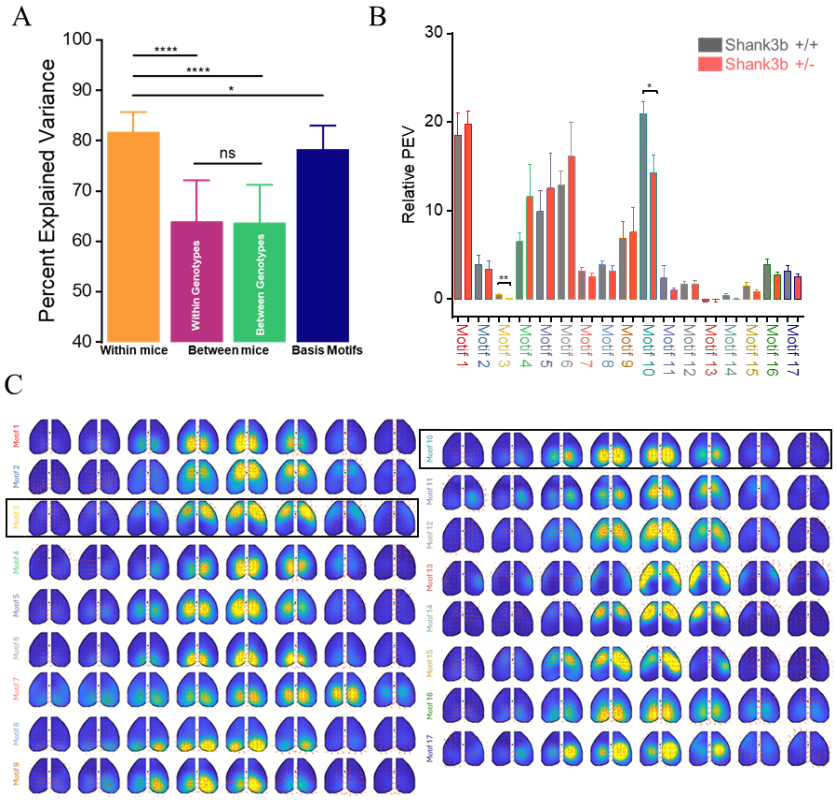

Figure 2.11. Shank3b+/– mice exhibit altered expression of specific motifs and distinct correlations with global movement.
(A) Percent explained variance of the discovered motifs: within individual mice (orange), between mice of the same genotype (purple), between mice of different genotypes (green), and for the basis motifs across all mice (blue)
(B) Relative percent explained variance for each basis motif in Shank3b+/+ (black) and Shank3b+/– (red) mice (NShank3+/+ = 7 mice; NShank3b+/- = 9 mice; Two sample t test).
(C) Basis motifs discovered within genotypes. Black rectangle indicates motifs with different expression.

Nepochs/Nmice= 36/9; p= 0.22 Two sample t test) (Fig. 2.10C and D).

Some specific motifs show a different expression between genotypes

Percent Explained Variance (PEV) was used to evaluate motif expression. Motifs were refitted within and between mice, revealing a marked decrease in expression when refitted across different mice (Fig. 2.11A) (Within mice: 81.6 ± 0.51 %; Between mice-within genotype: 63.7 ± 1.04 %; Between mice-between genotype: 63.5 ± 0.97 %; Basis motifs: 78.2 ± 0.59 %; Nepochs/Nmice = 64/16; ANOVA Two way RM, Tukey correction). This result indicates that motifs extracted from one epoch in a given mouse can explain the variance of another epoch from the same mouse but fail to capture the variance of a different mouse. Interestingly, no significant differences were observed when comparing refitting between mice of the same genotype versus different genotypes (Fig. 2.11A).

The ability of motifs to generalize across time and individuals suggests the existence of a set of basis motifs capturing canonical spatiotemporal dynamics. To identify these basis motifs, we applied an unsupervised clustering algorithm to group all motifs identified across animals and epochs. Clustering was performed using the Phenograph algorithm, with the peak of the temporal cross-correlation as the distance metric. This analysis yielded 17 distinct motif clusters (Fig. 2.1B and C). Unexpectedly, these basis motifs exhibited lower PEV compared to within-mouse motifs (Fig. 2.11A), suggesting potential differences in motif expression between genotypes. Indeed, relative PEV analysis revealed significant differences for specific motifs between genotypes (Fig. 2.11B). In particular, motifs 3 and 10 showed lower expression in Shankb +/- mice.

These results demonstrate that Shank3b+/- mice show an altered spatiotemporal dynamics, resulting in a different expression of motifs arising from motor and associative cortices.

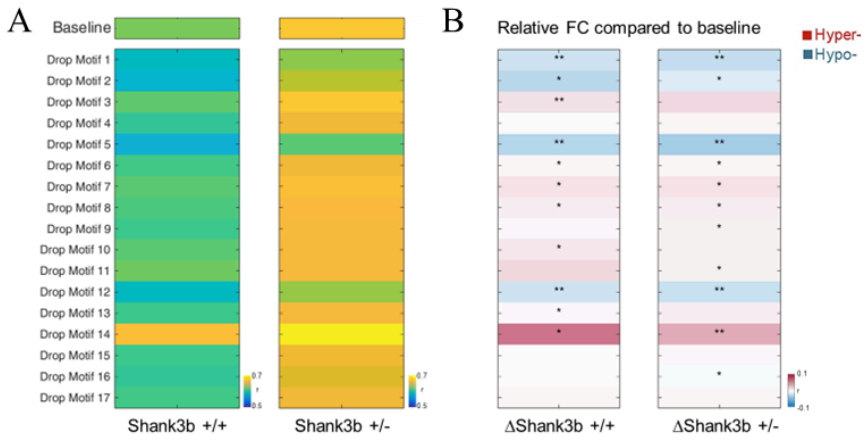

Figure 2.12. Some motifs contribute more than others to the hyper-connectivity observed in Shank3b+/– mice.
(A) FC matrices computed after dropping each individual motif, showing global FC in Shank3b+/+ (left), Shank3b+/– (right).
(B) Relative FC compared to baseline in Shank3b+/+ (left), Shank3b+/– (right). Red indicates increased connectivity; blue indicates decreased connectivity. Asterisks denote statistically significant differences (*p < 0.05; **p < 0.01).

Certain motifs contribute more than others to the hyper-connectivity observed in Shank3b mice.

To assess the contribution of each motif to the cortical deficits observed in Shank3b+/− mice, we computed FC for both WT and Shank3b+/− mice by systematically dropping each motif from the total reconstruction (baseline). Compared to baseline, each motif contributed differently to FC across genotypes (Fig. 2.12A and B). For example, dropping the motif number 6, 7, 8 and 14 resulted in an increase of the connectivity in both genotypes, while dropping 1, 2, 5, 12 induced hypo-connectivity compared to the baseline. Importantly, an increase in the connectivity was observed associated with dropping the motif number 3 and 10 (more expressed in WT mice) in Shank3b+/+ only. Conversely, dropping the motif number 9, 11 and 16 resulted in an

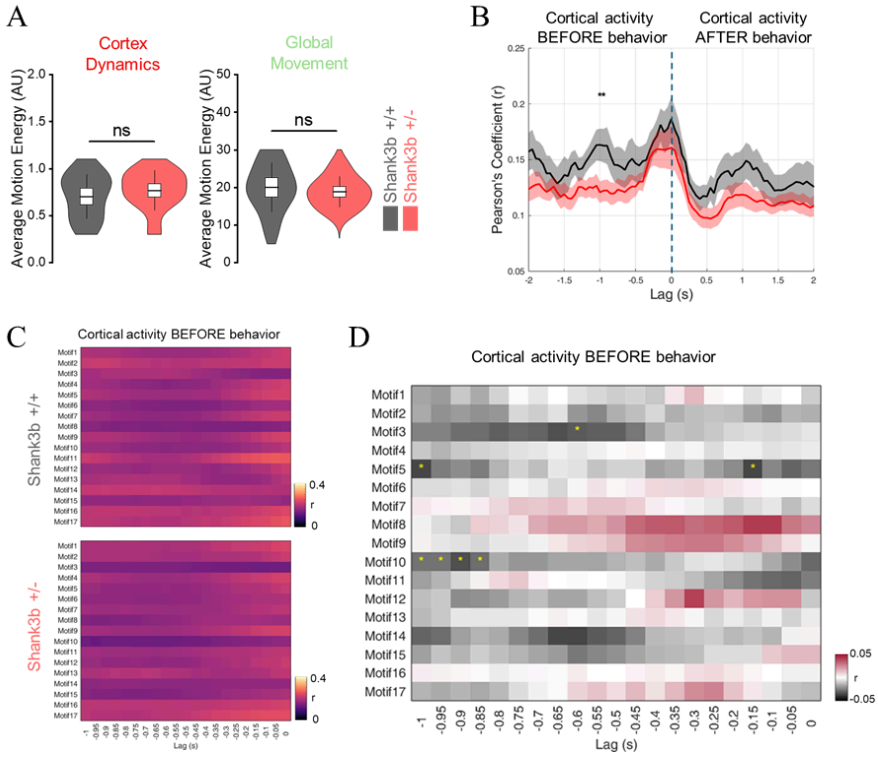

Figure 2.13. Disruption of cortex-movement correlation in Shank3b+/- mice.
(A) Quantification of average motion energy from cortical dynamics (left, red) and global movement (right, green) in Shank3b+/+ (black) and Shank3b+/– (red) mice.
(B) Correlation between global movement and cortical dynamics at different time lags in Shank3b+/+ (black) and Shank3b+/– (red) mice. The dashed line indicates lag = 0. Asterisks denote statistically significant differences ($p < 0.05$).
(C) Correlation between global movement and motif dynamics across time lags before behavior in Shank3b+/+ (top) and Shank3b+/– (bottom) mice.
(D) Differences in correlation between global movement and motif dynamics across time lags before behavior. Black indicates higher correlation in Shank3b+/+ mice; red indicates higher correlation in Shank3b+/– mice. Asterisks denote statistically significant differences ($p < 0.05$).

hyper-connectivity in Shank3b+/- compared to the baseline. These findings indicate that individual motifs have distinct impacts on the observed FC deficit.

Impaired correlation between cortical dynamics and behavior in Shank3b mice 1 second before movement generated by specific motifs

We observed that Shank3b+/− mice exhibit both behavioral impairments and cortical alterations; however, the extent to which cortical activity contributes to behavior in this model remains unclear. During WFFI, mice were head-fixed but allowed to move their forepaws freely, enabling us to directly compare cortical dynamics with global movements on a frame-by-frame basis.

To this end, we calculated motion energy for both cortical activity and behavioral movements. This analysis revealed no significant differences between genotypes in motion energy, either at the cortical or behavioral level (Cortex dynamics-Shank3b+/+: 0.70 ± 0.09 AU; N = 7 mice; Cortex dynamics-Shank3b+/-: 0.77 ± 0.07 AU; N = 9 mice; p= 0.57 Two sample t test. Global movement-Shank3b+/+: 20.0 ± 2.50 AU; N = 7 mice; Global Movement-Shank3b+/-: 18.8 ± 1.37 AU; N = 9 mice; p= 0.66 Two sample t test) (Fig. 2.13A).

We then examined the temporal relationship between cortical activity and movement by correlating the respective traces across different time lags. In both genotypes, cortical activity was correlated with movement; however, WT mice displayed a significantly higher correlation one second prior to movement onset compared to Shank3b+/− mice (Fig. 2.13B).

Next, to assess whether specific cortical motifs were preferentially correlated with movement one second before onset, we performed the correlation analysis for each motif individually (Fig. 2.13C). We considered three possible scenarios: (1) different patterns are activated in WT and Shank3b+/− mice 1 second before movement; (2) the same pattern is activated at different lags in the two genotypes; (3) different patterns are activated at different lags in the two genotypes.

Our results showed that in WT mice, specific motifs – particularly motifs 5 and 10, related to associative cortical areas – were preferentially activated 1s before the movement. These motifs exhibited weaker correlations in Shank3b+/− mice at the same lag. Although not statistically significant, other motifs (e.g., 8 and 9, associated with visual areas) appeared to be recruited at different time lags (–0.4s to –0.1s), consistent with the third hypothesis (Fig. 2.13D). Moreover, motif 3, involving motor cortices, was more strongly correlated in WT mice 0.6s before movement, whereas another motor-related motif 12 had a peak of correlation at lag = –0.3s in Shank3b+/− mice, with a trend toward significance ($p = 0.066$, two sample t test).

Overall, these results suggest that motif 10 is the key contributor to link disrupted preparatory activity to aberrant large-scale network organization.

Discussion

The present chapter provides new insights into the spatiotemporal organization of cortical dynamics and their relationship with behavior in a mouse model of ASD carrying a heterozygous deletion of Shank3. We selected the haploinsufficiency model because Shank3b+/- mice more accurately reflect the human condition than the Homozygous model (Drapeau et al., 2014; Bauer et al., 2023).

Our findings demonstrate that adolescent Shank3b+/− mice exhibit both behavioral abnormalities and cortical network dysfunctions that progressively worsen with age, particularly during wakefulness.

Behavioral assessments revealed increased anxiety-like behavior and altered grooming structure in juvenile Shank3b+/− mice (P20), consistent with previous reports describing neophobia and abnormal grooming in several Shank3 mutant models at later

developmental stages (Orefice et al., 2019; Bauer et al., 2023). These early behavioral alterations suggest that key features of the autistic-like phenotype in Shank3b mutants emerge before adolescence, when cortical networks are still undergoing significant maturation (Warm et al., 2025) (Fig. 2.4).

Importantly, our functional connectivity analysis demonstrated that alterations in the somatosensory network were already evident by P45 and persisted into adulthood (P90). This observation supports the hypothesis that somatosensory circuits are largely established by the second postnatal week (around P15) (Rahn et al., 2022), and that early disruptions in network organization may have long-lasting consequences on cortical function (Fig. 2.6).

Interestingly, connectivity alterations in motor cortices emerged later, at P60, likely reflecting the protracted maturation of anterior cortical regions. Indeed, motor, visual, and retrosplenial cortices undergo significant structural and functional changes between P22 and P60 in wild-type mice (Rahn et al., 2022; Mallya et al., 2019). Our findings align with observations from other ASD mouse models, where wakefulness is associated with widespread hyperconnectivity involving motor areas (Nakai et al., 2023) (Fig.2.9).

Conversely, Pagani and colleagues reported a deficit of prefrontal and frontostriatal hypo-connectivity in anesthetized Shank3b-/- mice (Pagani et al., 2019). This divergent result can be explained by the fact that here, the higher connectivity was found in the awake state, underlying the importance of the brain state on FC deficit. Indeed, we also found a non-significant trend of hypoconnectivity in deeply anesthetized Shank3b+/- mice. Additionally, differences between full knockout and heterozygous mice may contribute to genotype-specific effects. Finally, the profound anesthesia level required for fMRI could substantially alter the brain state recorded in these studies.

A central goal of this chapter was to dissect the contribution of elementary spatiotemporal patterns to cortical and behavioral phenotypes. Using CNMF-based decomposition, we identified a set of motifs consistently expressed across animals, suggesting the existence of canonical basis patterns underlying cortical dynamics. Although the overall number of motifs did not differ between genotypes, the expression strength of specific motifs was altered in Shank3b+/− mice, as shown by PEV analysis. Motifs 3, and 10 were more expressed in WT mice, indicating selective disruption rather than a global loss of spatiotemporal diversity (Fig. 2.11).

To understand whether these motifs contribute to network dysfunction, we examined their impact on FC by systematically removing each motif from the reconstruction. We found that motif number 3 and 10 contribute more than others to the observed hyperconnectivity. This aligns with recent evidence linking specific mesoscale activity patterns to functional integration across cortical modules (MacDowell & Buschman, 2020; MacDowell et al., 2024) (Fig. 2.12).

Finally, by correlating cortical dynamics with movement on a frame-by-frame basis, we demonstrated that both genotypes exhibit coupling between neural activity and behavior, consistent with the view that large-scale cortical states dynamically interact with motor output. However, WT mice showed a higher correlation approximately 1 second before movement onset, suggesting a predictive component of cortical activity that is blunted in Shank3b+/− mice. Indeed, motif-specific analysis revealed that in WT mice, motor and associative motifs (3, 5, and 10) were preferentially expressed before movement, whereas in Shank3b+/− mice, visual motifs (8 and 9) dominated and were expressed at different lags, despite non-significant. This shift implies a reorganization of cortical control strategies, possibly reflecting a compensatory reliance on sensory processing rather than motor planning (Fig. 2.13).

Taken together, these results indicate that cortical activity in Shank3b+/− mice is less predictive of the behavioral output, a mechanism that may contribute to deficits in motor coordination and goal-directed behaviors. Nevertheless, Shank3b+/- mice mostly exhibit a strong disruption of somatosensory areas.

Building on these results, in the next chapter we will examine the sensory-evoked responses of the cortex following whisker stimulation in the two genotypes and investigate the therapeutic potential of transcranial current stimulation on restoring cortical dysfunction.

Sensory-Evoked Deficits In Shank3b+/- Mouse Model Of Autism

Introduction

Neural bases of whisker-mediated stimulus perception

The whisker-mediated sensory pathway is an exceptionally organized ascending system (Fig. 3.1) , often compared to the human fingertip somatosensory pathway (Staiger & Petersen, 2020; Adibi, 2019). This system allows rodents to perform precise active sensation behaviors, such as texture discrimination and object localization (Adibi, 2019).

Specifically, mechanical whisker stimulation is first detected by trigeminal ganglion afferents, which transmit signals through the trigeminal nerve to the Brainstem Trigeminal Complex, where barrelettes preserve the vibrissae's somatotopic map (Adibi, 2019; Falcão et al., 2024). From there, information ascends to the Ventro-Posterior Medial (VPM) thalamic nucleus, organized into barreloids, which provide strong excitatory input to Layer 4 of the primary somatosensory (barrel) cortex (Adibi, 2019; Staiger & Petersen, 2020). In vS1, neurons encode stimulus features such as velocity and direction, with activity tightly regulated by feed-forward inhibition from local PV interneurons to maintain excitation-inhibition balance (Staiger & Petersen, 2020; Kremer et al., 2011). Finally, whisker-related signals are distributed to higher cortical areas and the hippocampal-entorhinal system, supporting integrative functions such as texture discrimination and sensorimotor processing (Adibi, 2019; Balasco et al., 2022).

Somatosensory deficits in Shank3b behavior

Atypical sensory processing, particularly altered responses to tactile stimuli, is a defining and clinically significant feature of ASD and PMS (Balasco et al., 2022; Delling et al., 2021; Falcão et al., 2024). Different studies have demonstrated somatosensory disruptions in several ASD mouse models' behavior (Drapeau et al., 2014; He et al., 2017; Liu et al., 2025). Behavioral assays

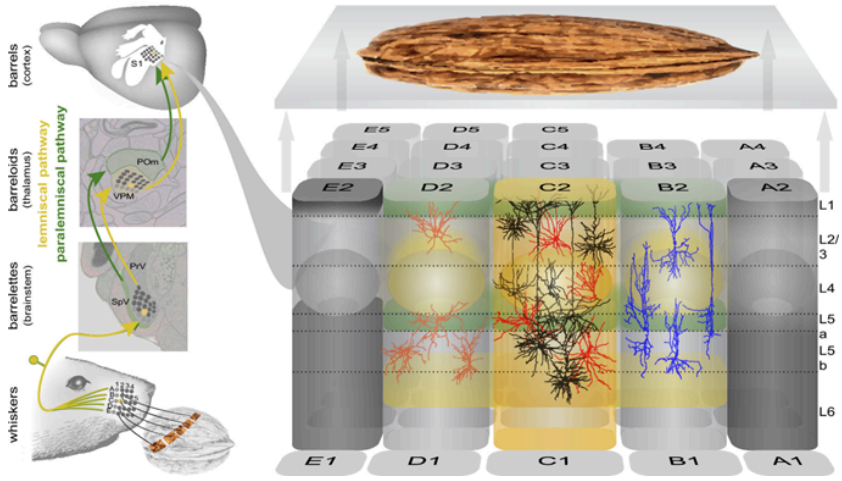

Figure 3.1. Whisker-to-barrel pathways conveying tactile information from the muzzle to the cortex.
On the left, the "labeled line" shows the two parallel pathways: lemniscal (yellow, via PrV–VPM) and paralemniscal (green, via SpV–POm), projecting to the whisker primary somatosensory cortex (wS1). On the right, a pseudo-3D view of wS1 highlights the main termination layers: lemniscal (L4/lower L3 and L5/6 border) and paralemniscal (L1 and L5a). Additional inputs are shown from whisker motor cortex (E2, left gray) and cholinergic fibers from the basal forebrain (A2, right gray). Representative neuron types are superimposed on different columns (SST-expressing interneurons in orange, PV in red, VIP in blue, and principal neurons in black). The walnut symbolizes cortical integration of parallel pathways into a unified tactile perception. Modified from Staiger & Petersen, 2020.

relying on whisker or tactile cues, such as the textured Novel Object Recognition Test (tNORT), the Whisker Nuisance (WN) test, and the vibrissa motion detection task, are widely used to dissect these phenotypes in mouse models (Balasco et al., 2022; Chen et al., 2020; Falcão et al., 2024; Orefice et al., 2019). Shank3 KO mice display complex somatosensory phenotypes, including deficits in whisker-dependent texture discrimination and hypo-responsiveness to repetitive tactile stimulation in the WN test (Balasco et al., 2022; Falcão et al., 2024), but also sensory hyper-reactivity in the vibrissa motion detection task, where they show lower detection thresholds and heightened sensitivity (Chen et al., 2020; Falcão et al., 2024). Larger

deletions of Shank3 (De4–22 KO or R1117X homozygotes) further reveal impaired pain perception, with marked deficits in heat hyperalgesia (Han et al., 2016; Gao et al., 2025), while R1117X homozygotes additionally show impaired sensory gating, including reduced prepulse inhibition (PPI), and diminished pain sensitivity reflected in higher Von Frey thresholds (Gao et al., 2025). In contrast, heterozygous mutants are generally characterized by tactile hypersensitivity, displaying increased responses to tactile prepulses (e.g., air puff-induced PPI), impaired texture discrimination, and altered pain processing (Orefice et al., 2019; Falcão et al., 2024; Han et al., 2016).

Neural deficits of sensory response in Shank3b mice

Somatosensory deficits in Shank3 mouse models emerge from abnormalities spanning peripheral inputs to cortical microcircuits and large-scale networks. In the primary somatosensory cortex (S1, BFD), the main alteration is an excitation/inhibition (E/I) imbalance, driven by pyramidal neuron hyperactivity and impaired GABAergic inhibition. Specifically, Shank3B KO mice show hyper-responsiveness to weak whisker deflections, reflected in elevated spontaneous and stimulus-evoked activity in Layer 2/3 pyramidal neurons, coupled with reduced activity of inhibitory interneurons (Chen et al., 2020; Falcão et al., 2024). A consistent feature across models is the vulnerability of PV-positive interneurons, whose reduced number or altered function disrupts feed-forward inhibition, a key mechanism regulating sensory gain in the BFD (Orefice et al., 2019; Staiger & Petersen, 2020). This imbalance explains sensory hyper-reactivity, while at the network level, Shank3 mutants also exhibit hypo-responsiveness to repetitive stimulation, associated with diminished c-fos activation in S1, hippocampus, and thalamus, and reduced long-range connectivity between S1 and hippocampus (Balasco et al., 2022).

Finally, electrophysiological studies have shown a decreasing cortical response to repeated auditory stimuli in PMS patients,

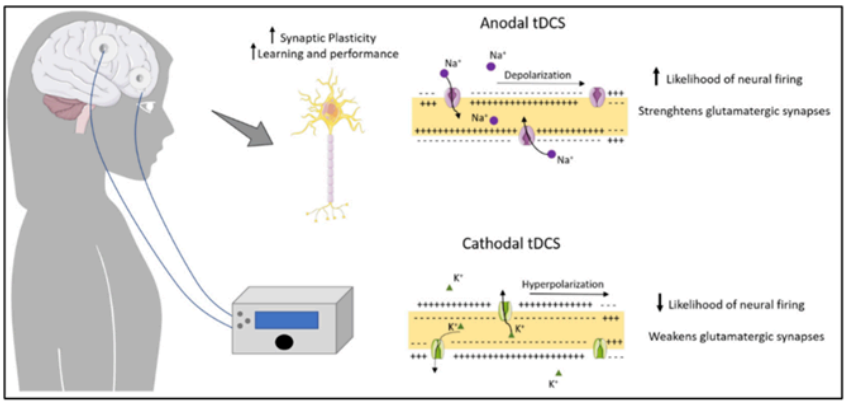

Figure 3.2 Effects of anodal and cathodal transcranial direct current stimulation.
The figure represents cortical neuromodulation associated with anodal (a-tDCS, excitatory) and cathodal (c-tDCS, inhibitory) stimulation. While the a-tDCS lead to increase synaptic plasticity, the c-tDCS weaks neuronal connections. Modified from Sousa et al., 2022

indicating an altered habituation process compared to neurotypical controls (Isenstein et al., 2022). Adaptation to repeated sensory stimulation in Shank3 mouse models is otherwise poorly understood from the neuronal perspective.

Thus, Shank3 deficiency destabilizes both local inhibitory control and large-scale sensory integration, producing a dual phenotype of hyper-reactivity to weak inputs and hypo-responsiveness to sustained stimulation. Recently developed neuromodulation approaches can be leveraged to reconstitute sensory processing in ASD and PMS patients, as described in the next section.

Transcranial direct current stimulation as a translational tool for neuromodulation

Transcranial direct current stimulation (tDCS) is a non-invasive neuromodulatory technique that applies weak currents to modulate neural activity (Morya et al., 2019). It has been recently explored as a therapeutic approach in ASD for recovering

excitatory/inhibitory imbalance (Sousa et al., 2022; Kang et al., 2025). Functionally, it induces polarity-specific changes in cortical excitability: anodal tDCS (a-tDCS) depolarizes and increases excitability, whereas cathodal tDCS (c-tDCS) hyperpolarizes and decreases it (Fig. 3.2) (Podda et al., 2016, Sousa et al., 2022). These effects, mediated by current-induced shifts in neuronal compartments (somata, dendrites, axon terminals) (Morya et al., 2019), can outlast stimulation through synaptic plasticity mechanisms (Podda et al., 2016). In motor cortex slices, direct current stimulation induces a long-term potentiation dependent on NMDA receptors, requiring concurrent synaptic activation such as low-frequency stimulation (Fritsch et al., 2010). This plasticity involves activity-dependent Brain-Derived Neurotrophic Factor (BDNF) release and TrkB signaling (Fritsch et al., 2010).

In vivo studies demonstrated that a-tDCS enhances hippocampal plasticity and memory via epigenetic regulation, notably increased H3 acetylation at the Bdnf promoter (Podda et al., 2016). In sensory cortex, a-tDCS increases, and c-tDCS decreases, the amplitude of sensory-evoked potentials (SEPs) in mice, with c-tDCS producing longer-lasting suppression of SEPs and cortical oscillations, associated with elevated GABAergic markers (Sánchez-León et al., 2021). In humans, a-tDCS over S1 lowers vibrotactile detection and discrimination thresholds, while c-tDCS often yields weaker perceptual effects (Labbé et al., 2016).

Beyond basic mechanisms, clinical studies in children show that repeated sessions of cathodal tDCS over the left dorsolateral prefrontal cortex can reduce autistic symptomatology, with improvements in behavioral scales up to six months (Gómez et al., 2017). These effects are thought to arise from the capacity of tDCS to restore the excitation–inhibition balance, a mechanism often disrupted in ASD due to GABAergic dysfunction. Supporting this idea, rodent studies demonstrate that a-tDCS

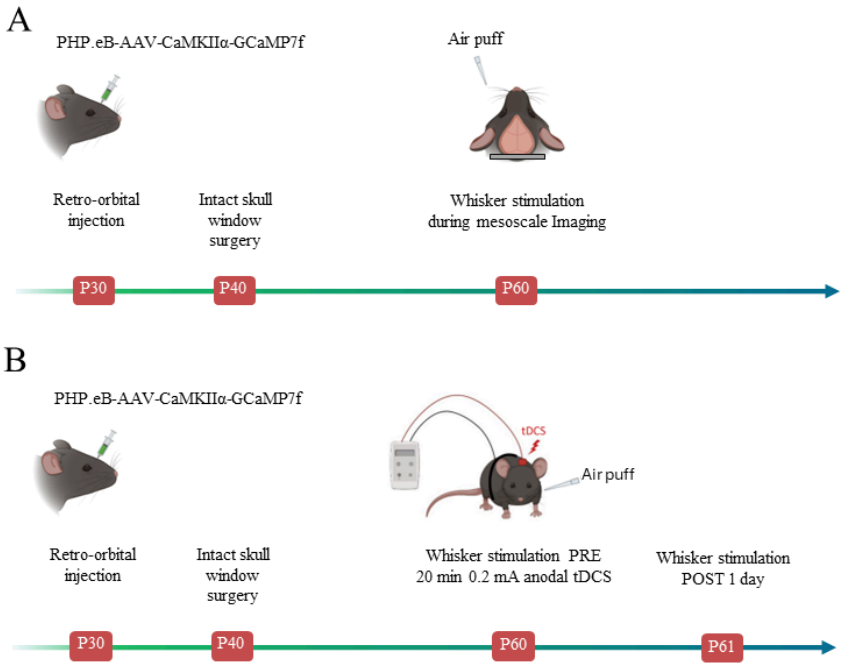

Figure 3.3. Experimental timeline for whisker stimulation imaging and transcranial direct current stimulation (tDCS).
(A) Experimental timeline with retro-orbital injection of GCaMP7f, optical window surgery and whisker stimulation at P60.
(B) Experimental timeline with retro-orbital injection of GCaMP7f, optical window surgery and whisker stimulation before and 1 day after 20 minutes of 0.2mA anodal tDCS.

enhances synaptic plasticity and upregulates neuroplasticity-related proteins, including BDNF and phosphorylated CREB (Podda et al., 2016; Barbati et al., 2020; Cavaleiro et al., 2020).

Given this evidence, we hypothesized that tDCS could alleviate sensory processing deficits associated with PMS, in which altered excitability and disrupted inhibitory function are core features. Building on these findings, in this last chapter we characterize somatosensory deficits in Shank3b+/- mice and test tDCS to modulate cortical excitability. To achieve this goal, we again exploit the expression of GCaMP7f indicator over the entire

dorsal cortex, which allows a comprehensive study of large-scale cortical activation among the two genotypes.

Materials and Methods

AAV injection and intact skull window surgery

A PHP.eB AAV vector was injected intravenously into mice at P30 to promote the expression of the calcium indicator GCaMP7f, as described in Chapters 1 and 2. In order to provide optical access to the cortex, an intact skull window procedure was performed ten days later (Fig. 3.3A). In a separate group of animals, following whisker stimulation at P60, a single session of electrical stimulation was delivered. In this group, a circular region was left free of dental cement over the BFD (x = 3 mm lateral to the right, y = 1 mm posterior to bregma) (Fig. 3.3B).

Unilateral multi whiskers stimulation

At P60, mice underwent sensory stimulation via single air puffs directed at the left whiskers. Stimulation was delivered using the Picospritzer III (General Valve™) connected to a tubing system positioned approximately 2 cm from the vibrissae. Each air puff had a duration of 60 ms and produced a ~1 cm deflection in the rostrocaudal direction. Each stimulation trial lasted 26 seconds and was structured as follows: 15 seconds of baseline (pre-stim), followed by the air puff (within a 1-second stimulation window), and concluding with 10 seconds of post-stimulus recording (post-stim). A total of 40 stimulation trials were recorded per animal during each session in the awake condition.

Transcranial direct current stimulation

The tDCS protocol consisted of 20 minutes of anodal stimulation at 0.2 mA. The current was applied using an animal transcranial electric stimulator (Soterix Medical), equipped with two

electrodes: the anode was placed on the exposed area of the head, while the cathode was embedded in a saline-soaked sponge in contact with the mouse's body. The anodal electrode did not directly touch the skull; instead, a drop of conductive gel was applied over the BFD to ensure proper contact.

Data Analysis

All data analyses were performed in MATLAB (MathWorks), Imagej and Origin.

Preprocessing

For each recording, ΔF/F was calculated by taking the baseline F as the mean of the signal before the whisker stimulation time point. Then, hemodynamic correction was computed and images were resized to 256 × 256.

Activated area

Average activity maps were extrapolated from the mean of the three maximum-activity frames over 50 stimuli. Quantification of activated area was extrapolated from the binarized masks based on the threshold of Mean + 2SD.

Peak amplitude and Full width at half maximum

All the stimuli were averaged within the same mouse and 10 × 10 pixels ROI was selected taking account of the BFD site. For each animal, peak amplitude and full width half maximum (FWHM) was calculated for different ROIs. Peak amplitude is defined as the maximum value in the 1s window following the whisker stimulation time point.

Sensory response across time

Sensory-evoked recordings of the BFD were divided into 8 chunks, each composed by 5 stimuli. Peak amplitude was computed for each chunk.

Sensory evoked functional connectivity

A total of 22 ROIs were defined based on the Allen Brain Atlas (Fig. 2.2). FC was estimated as Pearson's correlation between mean fluorescence signals of ROI pairs, calculated over 1-second windows before (PRE) and after (POST) whisker stimulation. Correlation matrices were Fisher z-transformed, averaged across animals within each group, and then converted back to r-values. PRE–POST differences were assessed by contrast matrices (POST – PRE) for each genotype. For tDCS analyses, only POST FC values were compared across time points. As in the previous chapter, FC graphs show ROIs positioned according to anatomical coordinates, with line thickness reflecting connection strength and node size the number of significant links. Significant network changes were identified using the Network-Based Statistic (Zalesky et al., 2010).

Statistical analysis

Two sample t test was used when comparing differences between genotypes (activated area, peak amplitude). Two way RM ANOVA followed by Tukey correction was used for differences in peak amplitude across trials. NBS Toolbox in MATLAB was used to statistically assess functional network connectivity. Two way RM ANOVA followed by Tukey correction was used for differences between baseline and stimulus FC. Differences were considered significant when $p<0.05$. Errors are reported as Standard Error of Means, *$p<0.05$, **$p<0.01$, ***$p<0.001$.

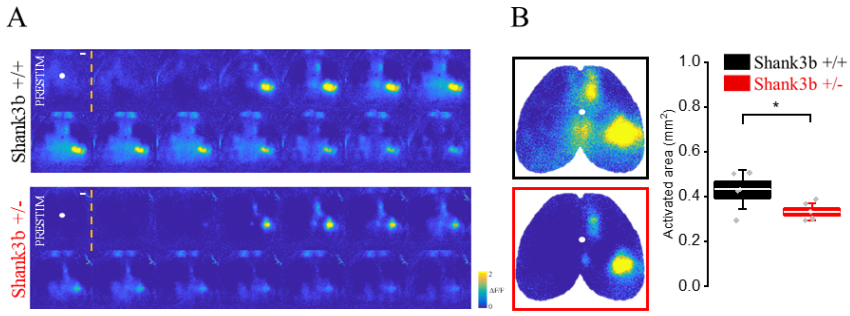

Figure 3.4. Sensory-evoked response in Shank3b+/- mice.
(A) Representative activation sequence of sensory-evoked response to whiskers stimulation in Shank3b+/+ (top, black) and Shank3b+/- mice (bottom, red). Yellow dashed line represents the whisker stimulus time point. White dot represents bregma, scale bar: 1 mm.
(B) (Left) Representative image of average activity maps in Shank3b+/+ (top, black) and Shank3b+/- mice (bottom, red). White dot represents bregma. (Right) Quantification of absolute (dots) and average (line) activated area in Shank3b+/+ (black) and Shank3b+/- mice (red).

Results

Reduced size of the activated area in Shank3b mice

At P60, cortical activity was recorded in mice of both genotypes before and after whisker stimulation. Both genotypes showed clear cortical activation, primarily localized in the BFD (Fig. 3.4A). Interestingly, the size of the activated area was significantly smaller in Shank3b+/- mice compared to WT (Fig. 3.4B) (Shank3b+/+ = 0.43 ± 0.04 mm², N = 5; Shank3b+/- = 0.33 ± 0.01 mm², N = 6; *p = 0.02, two sample t test).

This result suggests that the sensory-evoked response of the cortex is weakened in Shankb +/- mice.

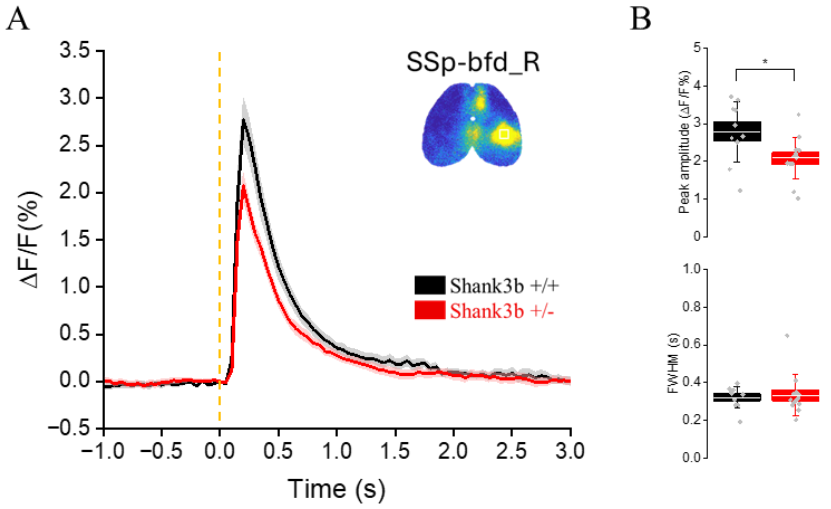

Figure 3.5. Sensory-evoked response in the barrelfield cortex.
(A) Sensory-evoked activity of the barrelfield cortex (inset) to whiskers stimulation in Shank3b+/+ (black) and Shank3b+/- mice (red). Yellow dashed line represents the whisker stimulus time point.
(B) (Top) Quantification of absolute (dots) and average (line) peak amplitude in Shank3b+/+ (black) and Shank3b+/- mice (red). (Bottom) Quantification of absolute (dots) and average (line) FWHM in Shank3b+/+ (black) and Shank3b+/- mice (red).

Shank3b mice exhibit reduced amplitude of the sensory-evoked response in the BFD following whisker stimulation

We then specifically investigated the sensory-evoked response in the BFD, the cortical area responsible for whisker stimulus perception and detection. Following stimulation, BFD activation was lower in Shank3b+/- mice, while the duration of the response remained unchanged (Fig. 3.5A). Across mice, the peak amplitude was significantly reduced in Shank3b+/- mice, whereas the FWHM of the response did not differ between genotypes (Fig. 3.5B) (Peak amplitude: Shank3b+/+ = 2.8 ± 0.2 %, N = 10; Shank3b+/- = 2.08 ± 0.1 %, N = 13; *p = 0.02, two sample t test; FWHM: Shank3b+/+ = 0.32 ± 0.18 s, N = 10;

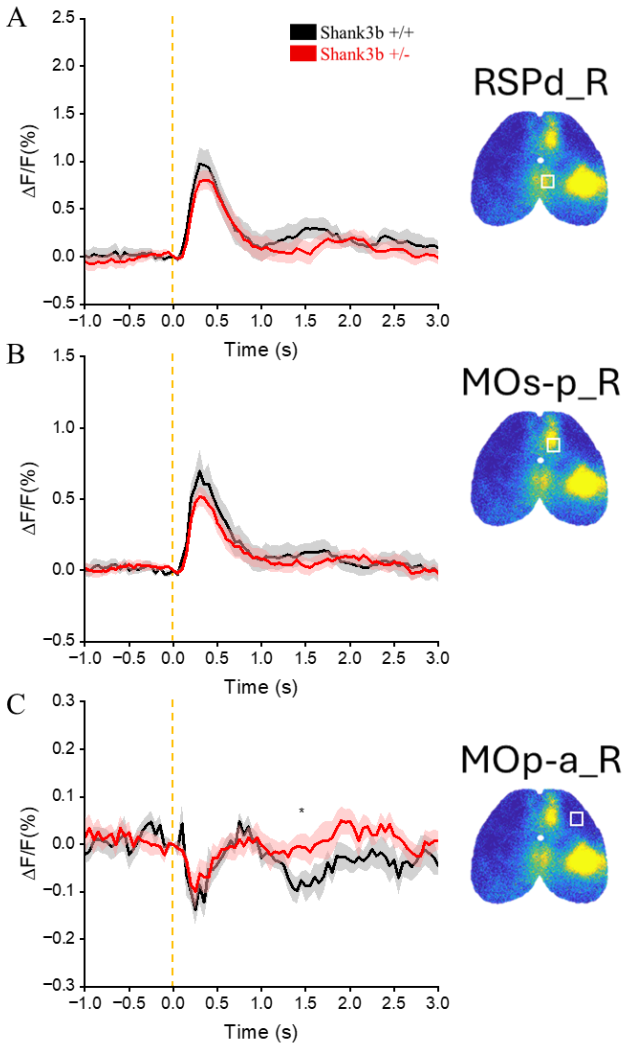

Figure 3.6. Sensory-evoked response in the retrosplenial and motor cortices.
(A) Sensory-evoked activity of the retrosplenial cortex (inset) to whiskers stimulation in Shank3b+/+ (black) and Shank3b+/- mice (red). Yellow dashed line represents the whisker stimulus time point.
(B) Sensory-evoked activity of the secondary posterior motor cortex (inset) to whiskers stimulation in Shank3b+/+ (black) and Shank3b+/- mice (red).
(C) Sensory-evoked activity of the primary anterior motor cortex (inset) to whiskers stimulation in Shank3b+/+ (black) and Shank3b+/- mice (red). Yellow dashed line represents the whisker stimulus time point. Asterisks represent time-points in which the activation is significantly different between genotypes (N Shank3b+/+ = 10, N Shank3b+/- =13; *$p < 0.05$).

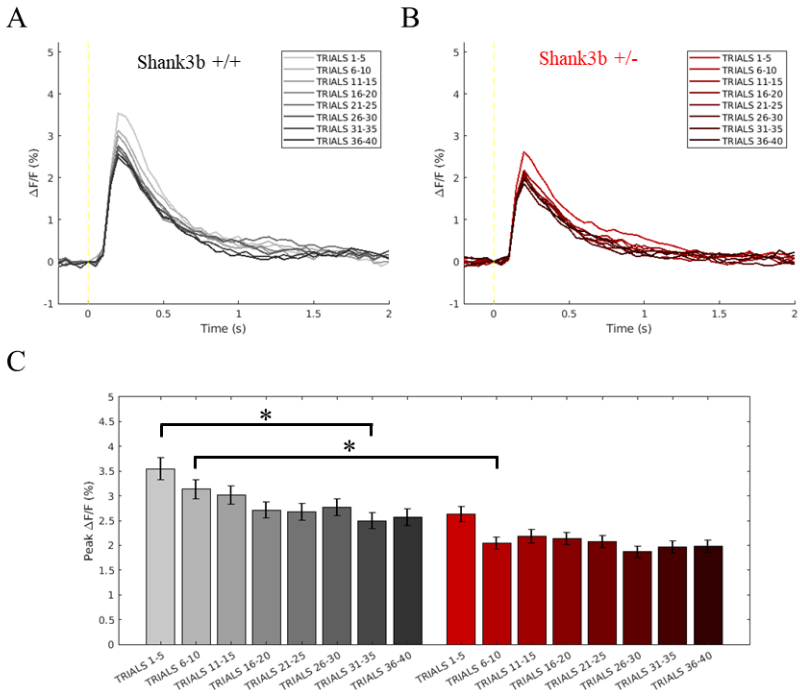

Figure 3.7. Sensory-evoked response in the barrelfield cortex across trials. (A,B) Sensory-evoked activity of the barrelfield cortex across trials to whiskers stimulation in Shank3b+/+ (A) and Shank3b+/- (B). Yellow dashed line represents the whisker stimulus time point.
(C) Bar plot indicating the quantification of average peak amplitude in across trials in Shank3b+/+ (black) and Shank3b+/- (red). Asterisk represent chunks in which the peak amplitude is significantly different (N Shank3b+/+ = 10, N Shank3b+/- = 13; *p < 0.05, Two way RM ANOVA, Tukey correction).

Shank3b+/- = 0.33 ± 0.22 s, N = 13). Overall, despite the duration of the response being the same between genotypes, Shank3b+/- mice showed a lower peak amplitude compared to their wild-type littermates.

Reduced feed-back processing of whisker-evoked responses in Shank3 mice

The lower BFD activation may result in altered distributed sensory processing across the cortex. We examined activation in various dorsal cortical areas. Although not statistically significant,

the retrosplenial cortex and the secondary motor cortex in the stimulated hemisphere showed reduced activation in Shank3b+/- mice (Fig. 3.6A and B). In contrast, the primary motor cortex (MOp-a_R) displayed a peak of activation 0.85 s after the stimulus in both the genotypes, which was more persistent in Shank3b+/- mice (Fig. 3.6C). Indeed, the ΔF/F 1.5 s after stimulation is significantly higher in Shank3b+/- mice (N Shank3b+/+ = 10, N Shank3b+/- =13; *p = 0.04, two sample t test) (Fig. 3.6C). These findings indicate that the computation of sensory inputs is processed differently across cortical regions in the two genotypes, possibly due to altered feedforward and feedback signaling.

Temporal adaptation to whisker-evoked responses differ between genotypes

We then analyzed the adaptation to repeated presentation of the same sensory stimulus in the BFD. By dividing trials into different segments, we assessed how the two genotypes adapt BFD activity to repeated whisker stimulation. Shank3b+/+ mice exhibited progressive adaptation, with BFD activity slowly dropping until reaching a plateau after 30 stimuli (Fig. 3.7A and C). In contrast, Shank3b+/- mice did not show a significant adaptation of BFD activity over the course of stimulation (Fig. 3.7B and C) (N Shank3b+/+ = 10, N Shank3b+/- = 13; *p = 0.048, Two way RM ANOVA, Tukey correction). Interestingly, the second chunk of stimuli contributes more than the others to the decrease in the BFD activity in Shank3b+/- mice (Fig. 3.7C) (N Shank3b+/+ = 10, N Shank3b+/- = 13; *p = 0.35, Two way RM ANOVA, Tukey correction).

Shank3b mice exhibit an altered sensory-evoked connectivity pattern

To investigate how different cortical areas are functionally connected during whisker stimulation across genotypes,

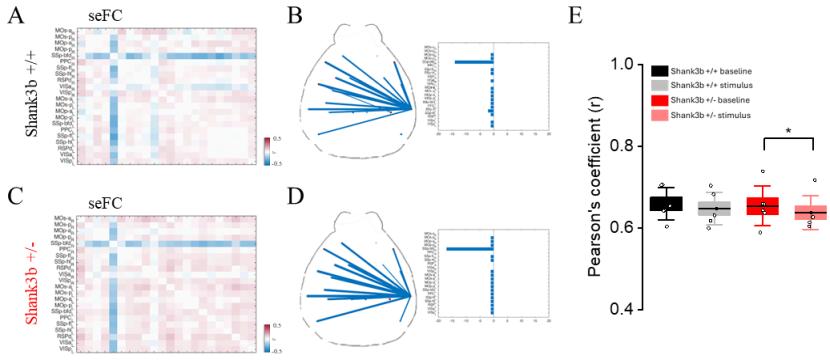

Figure 3.8. Sensory-evoked functional connectivity.
(A) Difference matrix of functional connectivity in Shank3b+/+ mice pre- and post-whisker stimulation (ws). Red and blue indicate post hyper- or hypo-connectivity, with significant differences in yellow (N=6, 60 stimulations).
(B) Network diagrams demonstrating statistically significant seFC changes. The number of significant FC modifications for each cortical area is shown in the bar plot on the right. Shank3b+/+ = 6. NBS. $p < 0.05$ is the statistical test.
(C) Difference matrix of functional connectivity in Shank3b+/- mice pre- and post-whisker stimulation (ws). Red and blue indicate post hyper- or hypo-connectivity, with significant differences in yellow (N=6, 60 stimulations).
(D) Network diagrams demonstrating statistically significant seFC changes. The number of significant FC modifications for each cortical area is shown in the bar plot on the right. Shank3b+/- = 6. NBS. $p < 0.05$ is the statistical test.
(E) Quantification of BFD FC differences in baseline and stimulus for both genotypes ((N Shank3b+/+ = 6, N Shank3b+/- =6; *$p < 0.05$; Two way RM ANOVA).

sensory-evoked connectivity (seFC) was computed in the 1-second window before (baseline) and after (stimulus) the whisker stimulation. Then, a difference matrix was calculated by subtracting the baseline from the stimulus. As expected, the stimulated BFD cortex showed the strongest hypo-connectivity in the stimulus window compared to the baseline (Fig. 3.8A and C). This indicates that the correlation between the BFD and other areas is reduced, according to the sensory-evoked response being localized in this region.In WT mice, connectivity between the stimulated BFD and other sensory areas of the stimulated hemisphere (SSp-flR, SSp-hlR, VISaR) was reduced compared to

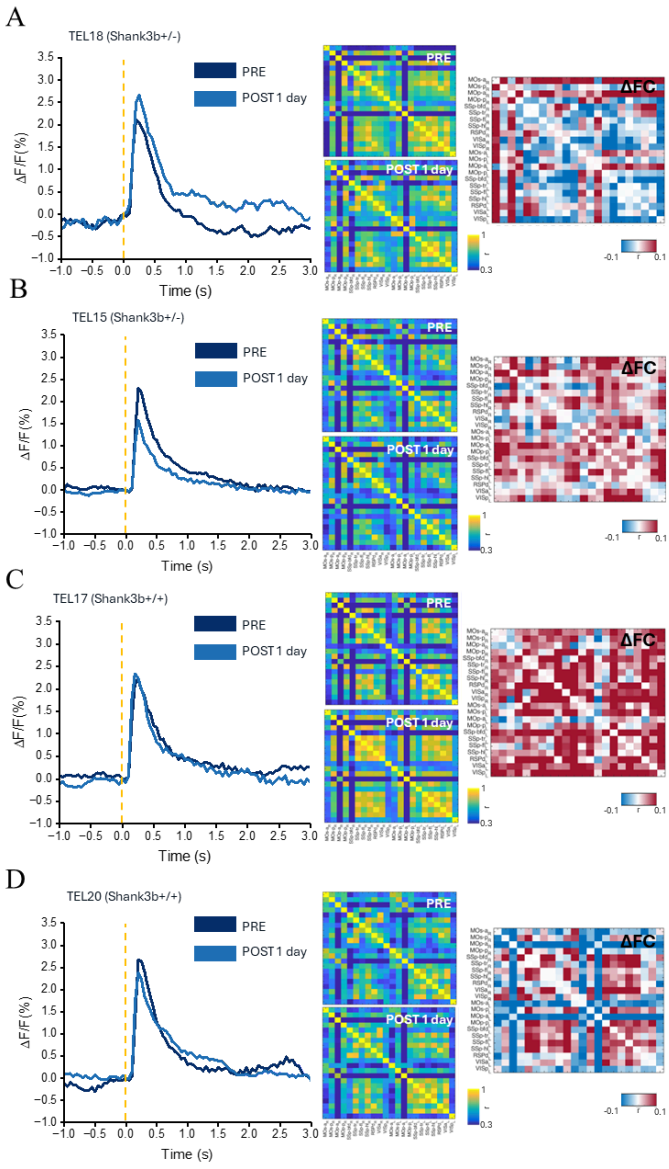

Figure 3.9. tDCS effect on sensory-evoked response and FC in Shank3b+/+ and Shank3b+/- mice.
(A-D) Sensory-evoked BFD activity (left) and FC (right) PRE and POST 1 day after anodal tDCS in Shank3b+/- mice (A and B) and Shank3b+/+ mice (C and D). Yellow dashed line represents the whisker stimulus time point. Red and blue indicate post-tDCS hyper- or hypo-connectivity compared to pre-tDCS.

baseline. The BFD was also hypo-connected with the Primary motor cortices of the stimulated hemisphere. Overall, the BFD is hypo-connected with all the contralateral areas except for the RSPL (Fig. 3.8A and B). When the same analysis was applied to Shank3b+/- mice, a different connectivity pattern emerged. Specifically, the BFD showed reduced connectivity with the whole contralateral hemisphere and secondary motor and visual cortices in the ipsilateral hemisphere (Fig. 3.8C and D). We then compared the baseline FC and the stimulus FC between the BFD and the other regions in the two genotypes. We demonstrated that globally, only Shank3b+/- mice show a significant decrease of the FC after the stimulation (Shank3b+/+ baseline = 0.66 ± 0.02 r; Shank3b+/+ stimulus = 0.65 ± 0.02 r; Shank3b+/- baseline = 0.65 ± 0.02 r; Shank3b+/- stimulus = 0.64 ± 0.02 r; ; *p= 0.03, Two way RM ANOVA, Tukey correction) (Fig 3.8E). These findings suggest that the whisker-evoked response is more spatially restricted in Shank3b+/- mice.

A 20 minutes transcranial current stimulation disrupts BFD responses and alters connectivity

Finally, we did preliminary experiments to test the effects of anodal tDCS to perturb cortical excitability and assess its potential as a therapeutic strategy for PMS. In a separate batch of animals (N Shank3b+/+ = 2; N Shank3b+/- = 2) we compared the whisker-evoked response before and 1 day after 20 minutes of 0.2mA anodal tDCS. Figure 3.9 shows singularly the effect of tDCS on BFD activity and FC in 4 subjects (TEL 18, TEL 15 = Shank3B+/-; TEL17, TEL20 = Shankb +/+). This preliminary experiment suggests that a single application of anodal current on the BFD can increase the amplitude of the evoked response 1 day after tDCS , but only in a subset of the treated subjects (see the example in Fig. 3.9A). Indeed, some mice show a reduction of the response, or no effects, regardless of the genotype (Fig. 3.9B-D). Similarly, high variability can be observed in terms of FC (stimulus) outcome one day after tDCS (Fig. 3.9A-D).

Overall, these findings demonstrated that Shank3b+/- mice show a disrupted large-scale cortical sensory-evoked response and that we need further investigations to confirm the effectiveness of tDCS to ameliorate sensory deficits.

Discussion

In this part of the PhD project, we show that Shank3b+/- mice display pronounced alterations in cortical processing of whisker stimulation compared to wild-type controls. Both genotypes exhibited clear activation in the barrel field, but in Shank3b+/- mice the response was characterized by a smaller spatial extent and lower peak amplitude, indicating that sensory input reaches the cortex but is represented in a weaker and more spatially restricted form (Fig. 3.4 and 3.5). This impairment likely reflects altered excitatory synaptic drive and/or an imbalance in local excitation and inhibition, mechanisms that have been frequently associated with Shank3 deficiency and autism spectrum disorders (Peca et al., 2011; Chen et al., 2020). Interestingly, Chen et al. (2020) reported hyperactivation of layer 2/3 BFD neurons in Shank3b-/- mutant mice using 2PEF imaging, suggesting enhanced excitatory responses at the single-cell level. The discrepancy between this and our results may reflect methodological differences between 2PEF imaging and WFFI. Alternatively, even if single L2/3 neurons' responses are higher, the overall fraction of stimulus responding cells (including L5 neurons) could be lower. Thus, while individual neurons may be hyperactive, the overall cortical representation of sensory input appears weaker and more spatially restricted in Shank3b+/- mice, highlighting the importance of scale when interpreting cortical activity patterns.

Beyond local activity of the BFD, we observed that the sensory-evoked activations across cortical areas were also altered. Specifically, in Shank3b+/- mice the spread of cortical activation was reduced or possibly delayed, particularly in the motor

cortices and retrosplenial areas (Fig. 3.6). These results suggest that the coordination of the activity propagation within the sensory network, and specifically the top-down control from associative regions, is disrupted in Shank3b+/- mice, potentially leading to impaired sensorimotor integration.

Analysis of temporal adaptation further revealed that WT mice showed a gradual decrease in BFD activity after the first few stimuli, whereas Shank3b+/- mice did not exhibit significant adaptation, consistent with deficits in synaptic plasticity or inhibitory regulation (Chen et al., 2020). Song and colleagues reported a secondary component during the earlier trials of the awake state using voltage imaging (Song et al., 2018). Our data does not show any secondary peak in the BFD, possibly due to the slower dynamics of the calcium indicators compared to the voltage sensors (Lin & Schnitzer, 2016).

FC analyses confirmed that network reconfiguration following sensory input differs between genotypes, indicating a more spatially restricted and less integrated response in Shank3b+/- mice (Fig. 3.8).

Preliminary experiments using a-tDCS suggest that cortical excitability can be modulated, leading to changes in BFD response amplitude and connectivity (Fig. 3.9), but the effects were highly variable and not consistently linked to genotype, highlighting the need for further studies to identify optimal stimulation parameters and mechanisms.

An explanation to the variability across subjects could arise from the fact that both cortical excitability and the brain state influence the outcome of the tDCS (Bortoletto et al., 2015; Fehring et al., 2024).

Collectively, these results demonstrate that Shank3b haploinsufficiency disrupts both local and large-scale cortical

processing of sensory input, affecting the strength, spatial spread, temporal adaptation, and network integration of responses. Such alterations likely contribute to the sensory processing deficits observed in PMS and provide insight into the circuit-level mechanisms underlying these abnormalities. These findings underscore the importance of considering both local synaptic deficits and broader network dysfunction when investigating sensory and cognitive impairments in Shank3-related disorders, and may guide the development of targeted interventions to restore cortical processing in affected individuals.

Future Perspectives & Conclusions

In summary, this work provides new insights into the developmental trajectory of cortical dysfunction in the Shank3b+/- genetic model of ASD and highlights the interplay between altered network dynamics and behavioral impairments.

Future research should focus on optimizing the all-optical system developed here to achieve precise, targeted modulation of cortical circuits. This tool represents a promising avenue for future studies aimed at restoring physiological cortical dynamics. In particular, future work could exploit this system in a closed-loop configuration to dynamically modulate the expression of cortical motifs and rescue behaviorally relevant activity patterns in Shank3b+/– mice, possibly locking the modulation according to the phase of the brain activity.

Additionally, this optical approach could be employed to modulate cortical responses to somatosensory inputs, especially in regions showing excessive activation compared to WT animals (e.g., motor cortex). Complementary experiments could focus on enhancing the responsiveness of cortical neurons to whisker stimulation in the BFD through optogenetic activation using well-established actuators such as ChR2. Its application to the Shank3b+/– model is technically straightforward and may provide important insights into restoring appropriate sensory-motor integration.

We also attempted to modulate cortical dysfunction through the application of transcranial current stimulation. However, this approach produced highly variable outcomes across animals, suggesting that the technique requires further optimization and parameter refinement before its potential therapeutic value in this model can be fully assessed.

In conclusion, continued efforts to optimize neuromodulation methods will be essential to translate these interventions into effective therapies for PMS.

References

- Acharya, A.R. *et al.* (2021) "In vivo blue light illumination for optogenetic inhibition: Effect on local temperature and excitability of the rat hippocampus," *Journal of Neural Engineering*, 18(6). Available at: https://doi.org/10.1088/1741-2552/ac3ef4.

- Adibi, M. (2019) "Whisker-Mediated Touch System in Rodents: From Neuron to Behavior," *Frontiers in Systems Neuroscience*. Frontiers Media S.A. Available at: https://doi.org/10.3389/fnsys.2019.00040.

- Ahmad, R.F. *et al.* (2016) "EEG-fMRI combination for better understanding of brain functions: Pros and cons," in *IEEE 2015 International Conference on Signal and Image Processing Applications, ICSIPA 2015 - Proceedings*. Institute of Electrical and Electronics Engineers Inc., pp. 278–281. Available at: https://doi.org/10.1109/ICSIPA.2015.7412204.

- Balasco, L. *et al.* (2022) "Abnormal whisker-dependent behaviors and altered cortico-hippocampal connectivity in Shank3b-/-mice," *Cerebral Cortex*, 32(14), pp. 3042–3056. Available at: https://doi.org/10.1093/cercor/bhab399.

- Barbati, S.A. *et al.* (2020) "Enhancing Plasticity Mechanisms in the Mouse Motor Cortex by Anodal Transcranial Direct-Current Stimulation: The Contribution of Nitric Oxide Signaling," *Cerebral Cortex*, 30(5), pp. 2972–2985. Available at: https://doi.org/10.1093/cercor/bhz288.

- Bauer, H.F. *et al.* (2023) "Development of sex- and genotype-specific behavioral phenotypes in a Shank3 mouse model for neurodevelopmental disorders," *Frontiers in Behavioral Neuroscience*, 16. Available at: https://doi.org/10.3389/fnbeh.2022.1051175.

➢ Bonaglia, M.C. *et al.* (2001) “Disruption of the ProSAP2 Gene in a t(12;22)(q24.1;q13.3) Is Associated with the 22q13.3 Deletion Syndrome”, *Am. J. Hum. Genet*, 69:261–268. Available at: https://doi: 10.1086/321293.

➢ Bortoletto M, *et al.* (2015) “The interaction with task-induced activity is more important than polarization: a tDCS study. *Brain Stimul,* 8(2):269-76. Available at: https//doi.org/ 10.1016/j.brs.2014.11.006.

➢ Boyden, E.S. *et al.* (2005) “Millisecond-timescale, genetically targeted optical control of neural activity,” *Nature Neuroscience*, 8(9), pp. 1263–1268. Available at: https://doi.org/10.1038/nn1525.

➢ Bozdagi, O. *et al.* (2010) “Haploinsufficiency of the autism-associated Shank3 gene leads to deficits in synaptic function, social interaction, and social communication,” *Molecular Autism*, 1(1). Available at: https://doi.org/10.1186/2040-2392-1-15.

➢ Brier, L.M. *et al.* (2022) “A Multivariate Functional Connectivity Approach to Mapping Brain Networks and Imputing Neural Activity in Mice,” *Cerebral Cortex*, 32(8), pp. 1593–1607. Available at: https://doi.org/10.1093/cercor/bhab282.

➢ Brini, M. *et al.* (2014) “Neuronal calcium signaling: Function and dysfunction,” *Cellular and Molecular Life Sciences*. Birkhauser Verlag AG, pp. 2787–2814. Available at: https://doi.org/10.1007/s00018-013-1550-7.

➢ Caminade, A.M. *et al.* (2019) “Fluorescent phosphorus dendrimers excited by two photons: Synthesis, two-photon absorption properties and biological uses,” *Beilstein Journal of Organic Chemistry*, 15, pp. 2287–2303. Available at: https://doi.org/10.3762/bjoc.15.221.

➢ Cavaleiro, C. *et al.* (2020) "Memory and Cognition-Related Neuroplasticity Enhancement by Transcranial Direct Current Stimulation in Rodents: A Systematic Review," *Neural Plasticity*. Hindawi Limited. Available at: https://doi.org/10.1155/2020/4795267.

➢ Chen, Q. *et al.* (2012) "Imaging Neural Activity Using Thy1-GCaMP Transgenic Mice," *Neuron*, 76(2), pp. 297–308. Available at: https://doi.org/10.1016/j.neuron.2012.07.011.

➢ Chen, Q. *et al.* (2020) "Dysfunction of cortical GABAergic neurons leads to sensory hyper-reactivity in a Shank3 mouse model of ASD," *Nature Neuroscience*, 23(4), pp. 520–532. Available at: https://doi.org/10.1038/s41593-020-0598-6.

➢ Chen, T.W. *et al.* (2013) "Ultrasensitive fluorescent proteins for imaging neuronal activity," *Nature*, 499(7458), pp. 295–300. Available at: https://doi.org/10.1038/nature12354.

➢ Costales, J.L. and Kolevzon, A. (2015) "Phelan–McDermid Syndrome and SHANK3: Implications for Treatment," *Neurotherapeutics*. Springer New York LLC, pp. 620–630. Available at: https://doi.org/10.1007/s13311-015-0352-z.

➢ Cramer, J. v. *et al.* (2019) "In vivo widefield calcium imaging of the mouse cortex for analysis of network connectivity in health and brain disease," *NeuroImage*, 199, pp. 570–584. Available at: https://doi.org/10.1016/j.neuroimage.2019.06.014.

➢ Dana, H. *et al.* (2016) "Sensitive red protein calcium indicators for imaging neural activity," *eLife*. Edited by M. Häusser, 5, p. e12727. Available at: https://doi.org/10.7554/eLife.12727.

➢ Dana, H. *et al.* (2019) "High-performance calcium sensors for imaging activity in neuronal populations and microcompartments," *Nature Methods*, 16(7), pp. 649–657. Available at: https://doi.org/10.1038/s41592-019-0435-6.

➢ Dasilva, M. *et al.* (2020) “Altered Neocortical Dynamics in a Mouse Model of Williams-Beuren Syndrome.” Available at: https://doi.org/10.1007/s12035-019-01732-4/Published.

➢ Deisseroth, K. (2011) “Optogenetics,” *Nature Methods*. Nature Publishing Group, pp. 26–29. Available at: https://doi.org/10.1038/nmeth.f.324.

➢ Delling, J.P. and Boeckers, T.M. (2021) “Comparison of SHANK3 deficiency in animal models: phenotypes, treatment strategies, and translational implications,” *Journal of Neurodevelopmental Disorders*. BioMed Central Ltd. Available at: https://doi.org/10.1186/s11689-021-09397-8.

➢ Deverman, B.E. *et al.* (2016) “Cre-dependent selection yields AAV variants for widespread gene transfer to the adult brain,” *Nature Biotechnology*, 34(2), pp. 204–209. Available at: https://doi.org/10.1038/nbt.3440.

➢ Drapeau, E. *et al.* (2014) “Absence of strong strain effects in behavioral analyses of Shank3-deficient mice,” *DMM Disease Models and Mechanisms*, 7(6), pp. 667–681. Available at: https://doi.org/10.1242/dmm.013821.

➢ Durand, C.M. *et al.* (2012) “SHANK3 mutations identified in autism lead to modification of dendritic spine morphology via an actin-dependent mechanism,” *Molecular Psychiatry*, 17(1), pp. 71–84. Available at: https://doi.org/10.1038/mp.2011.57.

➢ Emiliani, V. *et al.* (2015) “All-optical interrogation of neural circuits,” *Journal of Neuroscience*. Society for Neuroscience, pp. 13917–13926. Available at: https://doi.org/10.1523/JNEUROSCI.2916-15.2015.

➢ Esmaeili, V. *et al.* (2021) “Rapid suppression and sustained activation of distinct cortical regions for a delayed sensory-triggered motor response,” *Neuron*, 109(13), pp.

2183-2201.e9. Available at: https://doi.org/10.1016/j.neuron.2021.05.005.

➢ Falcão, M., Monteiro, P. and Jacinto, L. (2024) "Tactile sensory processing deficits in genetic mouse models of autism spectrum disorder," *Journal of Neurochemistry*. John Wiley and Sons Inc, pp. 2105–2123. Available at: https://doi.org/10.1111/jnc.16135.

➢ Fan, L.Z. *et al.* (2020) "All-Optical Electrophysiology Reveals the Role of Lateral Inhibition in Sensory Processing in Cortical Layer 1," *Cell*, 180(3), pp. 521-535.e18. Available at: https://doi.org/10.1016/j.cell.2020.01.001.

➢ Fehring, D. *et al.* (2024) "The role of neuronal variability in cognitive modulation via prefrontal direct current stimulation," *Brain*. Oxford University Press, pp. 3645–3647. Available at: https://doi.org/10.1093/brain/awae307.

➢ Forli, A. *et al.* (2018) "Two-Photon Bidirectional Control and Imaging of Neuronal Excitability with High Spatial Resolution In Vivo," *Cell Reports*, 22(11), pp. 3087–3098. Available at: https://doi.org/10.1016/j.celrep.2018.02.063.

➢ Fritsch, B. *et al.* (2010) "Direct current stimulation promotes BDNF-dependent synaptic plasticity: Potential implications for motor learning," *Neuron*, 66(2), pp. 198–204. Available at: https://doi.org/10.1016/j.neuron.2010.03.035.

➢ Gao, J. *et al.* (2025) "Comprehensive behavioral characterization and impaired hippocampal synaptic transmission in R1117X Shank3 mutant mice," *Translational Psychiatry*, 15(1). Available at: https://doi.org/10.1038/s41398-025-03505-1.

➢ Gómez, L. *et al.* (2017) "Non-invasive brain stimulation for children with autism spectrum disorders: A short-term outcome study," *Behavioral Sciences*, 7(3). Available at: https://doi.org/10.3390/bs7030063.

➢ Grødem, S. *et al.* (2021) “An updated suite of viral vectors for *in vivo* calcium imaging using local and retro-orbital injections.” Available at: https://doi.org/10.1101/2021.05.14.443815.

➢ Ha, S. *et al.* (2015) “Characteristics of Brains in Autism Spectrum Disorder: Structure, Function and Connectivity across the Lifespan,” *Experimental Neurobiology*, 24(4), pp. 273–284. Available at: https://doi.org/10.5607/en.2015.24.4.273.

➢ Hamodi, A.S. *et al.* (2020) “Transverse sinus injections drive robust whole-brain expression of transgenes,” *eLife*, 9, pp. 1–16. Available at: https://doi.org/10.7554/eLife.53639.

➢ Han, K. *et al.* (2013) “SHANK3 overexpression causes manic-like behaviour with unique pharmacogenetic properties,” *Nature*, 503(7474), pp. 72–77. Available at: https://doi.org/10.1038/nature12630.

➢ Han, Q. *et al.* (2016) “SHANK3 Deficiency Impairs Heat Hyperalgesia and TRPV1 Signaling in Primary Sensory Neurons,” *Neuron*, 92(6), pp. 1279–1293. Available at: https://doi.org/10.1016/j.neuron.2016.11.007.

➢ Harony-Nicolas, H. *et al.* (2015) “Phelan McDermid Syndrome: From Genetic Discoveries to Animal Models and Treatment,” *Journal of Child Neurology*. SAGE Publications Inc., pp. 1861–1870. Available at: https://doi.org/10.1177/0883073815600872.

➢ Hasnain, M.A. *et al.* (2025) “Separating cognitive and motor processes in the behaving mouse,” *Nature Neuroscience*, 28(3), pp. 640–653. Available at: https://doi.org/10.1038/s41593-024-01859-1.

➢ He, C.X. *et al.* (2017) “Tactile defensiveness and impaired adaptation of neuronal activity in the Fmr1 knock-out mouse model of autism,” *Journal of Neuroscience*, 37(27), pp.

6475–6487. Available at: https://doi.org/10.1523/JNEUROSCI.0651-17.2017.

➢ Helmchen, F. and Denk, W. (2005) "Deep tissue two-photon microscopy," *Nature Methods*. Nature Publishing Group, pp. 932–940. Available at: https://doi.org/10.1038/nmeth818.

➢ Hoshino, C. *et al.* (2021) "GABAergic neuron-specific whole-brain transduction by AAV-PHP.B incorporated with a new GAD65 promoter," *Molecular Brain*, 14(1). Available at: https://doi.org/10.1186/s13041-021-00746-1.

➢ Isenstein, E.L. *et al.* (2022) "Neural Markers of Auditory Response and Habituation in Phelan-McDermid Syndrome," *Frontiers in Neuroscience*, 16. Available at: https://doi.org/10.3389/fnins.2022.815933.

➢ Jameson, D.M.. (2014) "Introduction to fluorescence". C*RC Press, Taylor & Francis Group.*

➢ Jun, N.Y. and Cardin, J.A. (2019) "Activation of distinct channelrhodopsin variants engages different patterns of network activity," *eNeuro*, 7(1). Available at: https://doi.org/10.1523/ENEURO.0222-18.2019.

➢ Just, M.A. *et al.* (2007) "Functional and anatomical cortical underconnectivity in autism: Evidence from an fmri study of an executive function task and corpus callosum morphometry," *Cerebral Cortex*, 17(4), pp. 951–961. Available at: https://doi.org/10.1093/cercor/bhl006.

➢ Kalanithi, P.S.A. and Henderson, J.M. (2012) "Optogenetic Neuromodulation," in *International Review of Neurobiology*. Academic Press Inc., pp. 185–205. Available at: https://doi.org/10.1016/B978-0-12-404706-8.00010-3.

➢ Kang, J. *et al.* (2025) "Effects of Transcranial Direct Current Stimulation on Excitatory/Inhibitory Balance and Behavior in

Children With Autism—A Randomized Controlled Study," *Alpha Psychiatry*, 26(4). Available at: https://doi.org/10.31083/ap46111.

- Kinsky, N.R. *et al.* (2023) "Simultaneous electrophysiology and optogenetic perturbation of the same neurons in chronically implanted animals using μLED silicon probes," *STAR Protocols*, 4(4). Available at: https://doi.org/10.1016/j.xpro.2023.102570.

- Knöpfel, T. (2012) "Genetically encoded optical indicators for the analysis of neuronal circuits," *Nature Reviews Neuroscience*, pp. 687–700. Available at: https://doi.org/10.1038/nrn3293.

- Kolevzon, A. *et al.* (2014) "Phelan-McDermid syndrome: A review of the literature and practice parameters for medical assessment and monitoring," *Journal of Neurodevelopmental Disorders*. Springer Science and Business Media, LLC. Available at: https://doi.org/10.1186/1866-1955-6-39.

- Kouser, M. *et al.* (2013) "Loss of predominant shank3 isoforms results in hippocampus-dependent impairments in behavior and synaptic transmission," *Journal of Neuroscience*, 33(47), pp. 18448–18468. Available at: https://doi.org/10.1523/JNEUROSCI.3017-13.2013.

- Kremer, Y. *et al.* (2011) "Late emergence of the vibrissa direction selectivity map in the rat barrel cortex," *Journal of Neuroscience*, 31(29), pp. 10689–10700. Available at: https://doi.org/10.1523/JNEUROSCI.6541-10.2011.

- Labbé, S., Meftah, E.-M. and Chapman, C.E. (1978) "Effects of transcranial direct current stimulation of primary somatosensory cortex on vibrotactile detection and discrimination," *J Neurophysiol*, 115. Available at: https://doi.org/10.1152/jn.00506.2015.-Anodal.

- Levine, J.H. *et al.* (2015) "Data-Driven Phenotypic Dissection of AML Reveals Progenitor-like Cells that Correlate with

Prognosis," *Cell*, 162(1), pp. 184–197. Available at: https://doi.org/10.1016/j.cell.2015.05.047.

- Lim, D.H. *et al.* (2012) "In vivo large-scale cortical mapping using channelrhodopsin-2 stimulation in transgenic mice reveals asymmetric and reciprocal relationships between cortical areas," *Frontiers in Neural Circuits*. Available at: https://doi.org/10.3389/fncir.2012.00011

- Lim, D.H. *et al.* (2014) "Optogenetic mapping after stroke reveals network-wide scaling of functional connections and heterogeneous recovery of the peri-infarct," *Journal of Neuroscience*, 34(49), pp. 16455–16466. Available at: https://doi.org/10.1523/JNEUROSCI.3384-14.2014.

- Lin, M.Z. and Schnitzer, M.J. (2016) "Genetically encoded indicators of neuronal activity," *Nature Neuroscience*. Nature Publishing Group, pp. 1142–1153. Available at: https://doi.org/10.1038/nn.4359.

- Liu, J. *et al.* (2024) "Mapping the Behavioral Signatures of Shank3b Mice in Both Sexes," *Neuroscience Bulletin*, 40(9), pp. 1299–1314. Available at: https://doi.org/10.1007/s12264-024-01237-8.

- Liu, M. *et al.* (2025) "Effects of Early-Life Tactile Experience Enrichment on Autistic-Like Behaviors and Synaptic Alterations in Shank3 Mutant Mice," *Fundamental Research* [Preprint]. Available at: https://doi.org/10.1016/j.fmre.2025.09.011.

- Logothetis, N.K. *et al.* (2001) "Neurophysiological investigation of the basis of the fMRI signal," *Nature* 412, 150–157. Available at: https://doi.org/10.1038/35084005

- Lohani, S. *et al.* (2022) "Spatiotemporally heterogeneous coordination of cholinergic and neocortical activity," *Nature Neuroscience*, 25(12), pp. 1706–1713. Available at: https://doi.org/10.1038/s41593-022-01202-6.

➢ Lord, C. *et al.* (2018) "Autism spectrum disorder," *The Lancet*. Lancet Publishing Group, pp. 508–520. Available at: https://doi.org/10.1016/S0140-6736(18)31129-2.

➢ Luu, P., Fraser, S.E. and Schneider, F. (2024) "More than double the fun with two-photon excitation microscopy," *Communications Biology*. Nature Research. Available at: https://doi.org/10.1038/s42003-024-06057-0.

➢ Ma, Y. *et al.* (2016) "Wide-field optical mapping of neural activity and brain haemodynamics: Considerations and novel approaches," *Philosophical Transactions of the Royal Society B: Biological Sciences*. Royal Society of London. Available at: https://doi.org/10.1098/rstb.2015.0360.

➢ MacDowell, C.J. *et al.* (2024) "Differences in the expression of cortex-wide neural dynamics are related to behavioral phenotype," *Current Biology*, 34(6), pp. 1333-1340.e6. Available at: https://doi.org/10.1016/j.cub.2024.02.004.

➢ MacDowell, C.J. and Buschman, T.J. (2020) "Low-Dimensional Spatiotemporal Dynamics Underlie Cortex-wide Neural Activity," *Current Biology*, 30(14), pp. 2665-2680.e8. Available at: https://doi.org/10.1016/j.cub.2020.04.090.

➢ Mackevicius, E.L. *et al.* (2019) "Unsupervised discovery of temporal sequences in high-dimensional datasets, with applications to neuroscience," *eLife*, 8. Available at: https://doi.org/10.7554/eLife.38471.001.

➢ Mahn, M. *et al.* (2016) "Biophysical constraints of optogenetic inhibition at presynaptic terminals," *Nature Neuroscience*, 19(4), pp. 554–556. Available at: https://doi.org/10.1038/nn.4266.

➢ Mahn, M. *et al.* (2018) "High-efficiency optogenetic silencing with soma-targeted anion-conducting channelrhodopsins," *Nature Communications*, 9(1). Available at: https://doi.org/10.1038/s41467-018-06511-8.

➢ Mallya, A.P. *et al.* (2019) "Microglial Pruning of Synapses in the Prefrontal Cortex during Adolescence," *Cerebral Cortex*, 29(4), pp. 1634–1643. Available at: https://doi.org/10.1093/cercor/bhy061.

➢ Marvin, J.S. *et al.* (2013) "An optimized fluorescent probe for visualizing glutamate neurotransmission," *Nature Methods*, 10(2), pp. 162–170. Available at: https://doi.org/10.1038/nmeth.2333.

➢ Mathis, A. *et al.* (2018) "DeepLabCut: markerless pose estimation of user-defined body parts with deep learning," *Nature Neuroscience*, 21(9), pp. 1281–1289. Available at: https://doi.org/10.1038/s41593-018-0209-y.

➢ Michelson, N.J., Vanni, M.P. and Murphy, T.H. (2019) "Comparison between transgenic and AAV-PHP.eB-mediated expression of GCaMP6s using in vivo wide-field functional imaging of brain activity," *Neurophotonics*, 6(02), p. 1. Available at: https://doi.org/10.1117/1.nph.6.2.025014.

➢ Mizuno, A. *et al.* (2006) "Partially enhanced thalamocortical functional connectivity in autism," *Brain Research*, 1104(1), pp. 160–174. Available at: https://doi.org/10.1016/j.brainres.2006.05.064.

➢ Montagni, E. *et al.* (2019) "Wide-field imaging of cortical neuronal activity with red-shifted functional indicators during motor task execution," *Journal of Physics D: Applied Physics*, 52(7). Available at: https://doi.org/10.1088/1361-6463/aaf26c.

➢ Monteiro, P. and Feng, G. (2017) "SHANK proteins: Roles at the synapse and in autism spectrum disorder," *Nature Reviews Neuroscience*. Nature Publishing Group, pp. 147–157. Available at: https://doi.org/10.1038/nrn.2016.183.

➢ Morya, E. *et al.* (2019) "Beyond the target area: an integrative view of tDCS-induced motor cortex modulation in patients and athletes," *Journal of NeuroEngineering and Rehabilitation*.

BioMed Central Ltd. Available at: https://doi.org/10.1186/s12984-019-0581-1.

➢ Nakai, N. *et al.* (2023) "Virtual reality-based real-time imaging reveals abnormal cortical dynamics during behavioral transitions in a mouse model of autism," *Cell Reports*, 42(4). Available at: https://doi.org/10.1016/j.celrep.2023.112258.

➢ Nietz, A.K. *et al.* (2022) "Wide-Field Calcium Imaging of Neuronal Network Dynamics In Vivo," *Biology*. MDPI. Available at: https://doi.org/10.3390/biology11111601.

➢ Orefice, L.L. *et al.* (2019) "Targeting Peripheral Somatosensory Neurons to Improve Tactile-Related Phenotypes in ASD Models," *Cell*, 178(4), pp. 867-886.e24. Available at: https://doi.org/10.1016/j.cell.2019.07.024.

➢ Pagani, M. *et al.* (2019) "Deletion of autism risk gene shank3 disrupts prefrontal connectivity," *Journal of Neuroscience*, 39(27), pp. 5299–5310. Available at: https://doi.org/10.1523/JNEUROSCI.2529-18.2019.

➢ Pagano, J. *et al.* (2023) "Shank3 deletion in PV neurons is associated with abnormal behaviors and neuronal functions that are rescued by increasing GABAergic signaling," *Molecular Autism*, 14(1). Available at: https://doi.org/10.1186/s13229-023-00557-2.

➢ Palmer, A.E. *et al.* (2011) "Design and application of genetically encoded biosensors," *Trends in Biotechnology*, pp. 144–152. Available at: https://doi.org/10.1016/j.tibtech.2010.12.004.

➢ Park, J. *et al.* (2022) "Motor cortical output for skilled forelimb movement is selectively distributed across projection neuron classes", *Sci. Adv*. Available at: Park et al., Sci. Adv. 8, eabj5167 (2022)

➢ Patriarchi, T. *et al.* (2018) “Ultrafast neuronal imaging of dopamine dynamics with designed genetically encoded sensors,” *Science*, 360(6396). Available at: https://doi.org/10.1126/science.aat4422.

➢ Peça, J. *et al.* (2011) “Shank3 mutant mice display autistic-like behaviours and striatal dysfunction,” *Nature*, 472(7344), pp. 437–442. Available at: https://doi.org/10.1038/nature09965.

➢ Peixoto, R.T. *et al.* (2016) “Early hyperactivity and precocious maturation of corticostriatal circuits in Shank3B â ’/â ’ mice,” *Nature Neuroscience*, 19(5), pp. 716–724. Available at: https://doi.org/10.1038/nn.4260.

➢ Phelan, K. and McDermid, H.E. (2011) “The 22q13.3 deletion syndrome (Phelan-McDermid syndrome),” *Molecular Syndromology*, 2(3–5), pp. 186–201. Available at: https://doi.org/10.1159/000334260.

➢ Platisa, J. and Pieribone, V.A. (2018) “Genetically encoded fluorescent voltage indicators: are we there yet?,” *Current Opinion in Neurobiology*. Elsevier Ltd, pp. 146–153. Available at: https://doi.org/10.1016/j.conb.2018.02.006.

➢ Podda, M.V. *et al.* (2016) “Anodal transcranial direct current stimulation boosts synaptic plasticity and memory in mice via epigenetic regulation of Bdnf expression,” *Scientific Reports*, 6. Available at: https://doi.org/10.1038/srep22180.

➢ Sala, C. *et al.* (2001) “Regulation of Dendritic Spine Morphology and Synaptic Function by Shank and Homer”, *Neuron,* Vol. 31, 115–130. Available at: https://doi.org/10.1016/s0896-6273(01)00339-7

➢ Rahn, R.M. *et al.* (2022) “Functional Connectivity of the Developing Mouse Cortex,” *Cerebral Cortex*, 32(8), pp. 1755–1768. Available at: https://doi.org/10.1093/cercor/bhab312.

➢ Ren, C. and Komiyama, T. (2021) “Characterizing cortex-wide dynamics with wide-field calcium imaging,” *Journal of Neuroscience*, 41(19), pp. 4160–4168. Available at: https://doi.org/10.1523/JNEUROSCI.3003-20.2021.

➢ Resta, F. *et al.* (2022) “Large-scale all-optical dissection of motor cortex connectivity shows a segregated organization of mouse forelimb representations,” *Cell Reports*, 41(6). Available at: https://doi.org/10.1016/j.celrep.2022.111627.

➢ Rinaldi, T., Silberberg, G. and Markram, H. (2008) “Hyperconnectivity of local neocortical microcircuitry induced by prenatal exposure to valproic acid,” *Cerebral Cortex*, 18(4), pp. 763–770. Available at: https://doi.org/10.1093/cercor/bhm117.

➢ Salimzadeh, L. *et al.* (2013) “Non-Viral Transfection Methods Optimized for Gene Delivery to a Lung Cancer Cell Line”. *Avicenna J Med Biotech*; 5(2): 68-77. Available at: https://pmc.ncbi.nlm.nih.gov/articles/PMC3689559/

➢ Sánchez-León, C.A. *et al.* (2021) “Immediate and after effects of transcranial direct-current stimulation in the mouse primary somatosensory cortex,” *Scientific Reports*, 11(1). Available at: https://doi.org/10.1038/s41598-021-82364-4.

➢ Sarowar, T. and Grabrucker, A.M. (2016) “Actin-Dependent Alterations of Dendritic Spine Morphology in Shankopathies,” *Neural Plasticity*. Hindawi Limited. Available at: https://doi.org/10.1155/2016/8051861.

➢ Sato, M. *et al.* (2015) “Generation and imaging of transgenic mice that express G-CaMP7 under a tetracycline response element,” *PLoS ONE*, 10(5). Available at: https://doi.org/10.1371/journal.pone.0125354.

➢ Scaglione, A. *et al.* (2024) “Group ICA of wide-field calcium imaging data reveals the retrosplenial cortex as a major contributor to cortical activity during anesthesia,” *Frontiers in*

Cellular Neuroscience, 18. Available at: https://doi.org/10.3389/fncel.2024.1258793.

- Scheinost, D. *et al.* (2017) "Does prenatal stress alter the developing connectome?," *Pediatric Research*. Nature Publishing Group, pp. 214–226. Available at: https://doi.org/10.1038/pr.2016.197.

- Scott, B.B. *et al.* (2018) "Imaging Cortical Dynamics in GCaMP Transgenic Rats with a Head-Mounted Widefield Macroscope," *Neuron*, 100(5), pp. 1045-1058.e5. Available at: https://doi.org/10.1016/j.neuron.2018.09.050.

- Song, C. *et al.* (2018) "Cortical signatures of wakeful somatosensory processing," *Scientific Reports*, 8(1). Available at: https://doi.org/10.1038/s41598-018-30422-9.

- Sousa, B. *et al.* (2022) "Transcranial Direct Current Stimulation as an Approach to Mitigate Neurodevelopmental Disorders Affecting Excitation/Inhibition Balance: Focus on Autism Spectrum Disorder, Schizophrenia, and Attention Deficit/Hyperactivity Disorder," *Journal of Clinical Medicine*. MDPI. Available at: https://doi.org/10.3390/jcm11102839.

- Staiger, J.F. and Petersen, C.C.H. (2021) "Neuronal circuits in barrel cortex for whisker sensory perception," *Physiological Reviews*, 101(1), pp. 353–415. Available at: https://doi.org/10.1152/physrev.00019.2019.

- Suzuki, J., Kanemaru, K. and Iino, M. (2016) "Genetically Encoded Fluorescent Indicators for Organellar Calcium Imaging," *Biophysical Journal*. Biophysical Society, pp. 1119–1131. Available at: https://doi.org/10.1016/j.bpj.2016.04.054.

- Takumi, T. *et al.* (2020) "Behavioral neuroscience of autism," *Neuroscience and Biobehavioral Reviews*. Elsevier Ltd, pp. 60–76. Available at: https://doi.org/10.1016/j.neubiorev.2019.04.012.

➢ Tasic, B. *et al.* (2016) "Adult mouse cortical cell taxonomy revealed by single cell transcriptomics," *Nature Neuroscience*, 19(2), pp. 335–346. Available at: https://doi.org/10.1038/nn.4216.

➢ Turner, K.C. *et al.* (2006) "Atypically diffuse functional connectivity between caudate nuclei and cerebral cortex in autism," *Behavioral and Brain Functions*, 2. Available at: https://doi.org/10.1186/1744-9081-2-34.

➢ Uddin, L.Q. *et al.* (2015) "Brain state differentiation and behavioral inflexibility in autism," *Cerebral Cortex*, 25(12), pp. 4740–4747. Available at: https://doi.org/10.1093/cercor/bhu161.

➢ Valley, X.M.T. *et al.* (2020) "Higher Neural Functions and Behavior Separation of hemodynamic signals from GCaMP fluorescence measured with wide-field imaging," *J Neuro-physiol*, 123, pp. 356–366. Available at: https://doi.org/10.1152/jn.00304.2019.-Wide-field.

➢ Vasa, R.A., Mostofsky, S.H. and Ewen, J.B. (2016) "The Disrupted Connectivity Hypothesis of Autism Spectrum Disorders: Time for the Next Phase in Research," *Biological Psychiatry: Cognitive Neuroscience and Neuroimaging*. Elsevier Inc, pp. 245–252. Available at: https://doi.org/10.1016/j.bpsc.2016.02.003.

➢ Vinogradova, L. v., Rysakova, M.P. and Pavlova, I. v. (2020) "Small damage of brain parenchyma reliably triggers spreading depolarization," *Neurological Research*, 42(1), pp. 76–82. Available at: https://doi.org/10.1080/01616412.2019.1709745.

➢ Wang, X. *et al.* (2011) "Synaptic dysfunction and abnormal behaviors in mice lacking major isoforms of Shank3," *Human Molecular Genetics*, 20(15), pp. 3093–3108. Available at: https://doi.org/10.1093/hmg/ddr212.

➢ Wang, X. *et al.* (2013) "Distribution of CaMKIIα expression in the brain in vivo, studied by CaMKIIα-GFP mice," *Brain*

Research, 1518, pp. 9–25. Available at: https://doi.org/10.1016/j.brainres.2013.04.042.

- Warm, D. *et al.* (2025) "Spontaneous mesoscale calcium dynamics reflect the development of the modular functional architecture of the mouse cerebral cortex," *NeuroImage*, 309. Available at: https://doi.org/10.1016/j.neuroimage.2025.121088.

- Waters, J. (2020) "Sources of widefield fluorescence from the brain," *eLife*, 9, pp. 1–13. Available at: https://doi.org/10.7554/eLife.59841.

- Watkins de Jong, L. *et al.* (2023) "Optogenetics reveals paradoxical network stabilizations in hippocampal CA1 and CA3," *Current Biology*, 33(9), pp. 1689-1703.e5. Available at: https://doi.org/10.1016/j.cub.2023.03.032.

- Watt, J.L. *et al.* (1985) "A familial pericentric inversion of chromosome 22 with a recombinant subject illustrating a "pure" partial monosomy syndrome, Journal of Medical Genetics." *Journal of Medical Genetics* 1985, 22, 283-287. Available at: https://doi.org/10.1136/jmg.22.4.283

- Wiegert, J.S. *et al.* (2017) "Silencing Neurons: Tools, Applications, and Experimental Constraints," *Neuron*. Cell Press, pp. 504–529. Available at: https://doi.org/10.1016/j.neuron.2017.06.050.

- Yang, M. *et al.* (2012) "Reduced excitatory neurotransmission and mild Autism-Relevant phenotypes in adolescent shank3 null mutant mice," *Journal of Neuroscience*, 32(19), pp. 6525–6541. Available at: https://doi.org/10.1523/JNEUROSCI.6107-11.2012.

- Zalesky, A., Fornito, A. and Bullmore, E.T. (2010) "Network-based statistic: Identifying differences in brain networks," *NeuroImage*, 53(4), pp. 1197–1207. Available at: https://doi.org/10.1016/j.neuroimage.2010.06.041.

➢ Zerbi, V. *et al.* (2021) “Brain mapping across 16 autism mouse models reveals a spectrum of functional connectivity subtypes,” *Molecular Psychiatry*, 26(12), pp. 7610–7620. Available at: https://doi.org/10.1038/s41380-021-01245-4.

➢ Zhang, F. *et al.* (2006) “Channelrhodopsin-2 and optical control of excitable cells,” *Nature Methods*, 3(10), pp. 785–792. Available at: https://doi.org/10.1038/nmeth936.

➢ Zipfel, W.R., Williams, R.M. and Webb, W.W. (2003) “Nonlinear magic: Multiphoton microscopy in the biosciences,” *Nature Biotechnology*, pp. 1369–1377. Available at: https://doi.org/10.1038/nbt899.